Ultra-thin Materials from

Atomic Layer Deposition for Microbolometers

by

Nathan Thomas Eigenfeld

B.A. Physics, St. Olaf College, 2011

B.A. Mathematics, St. Olaf College, 2011

M.S. Mechanical Engineering, University of Colorado, 2013

A thesis submitted to the

Faculty of the Graduate School of the

University of Colorado in partial fulfillment

of the requirements for the degree of

Doctor of Philosophy

Department of Mechanical Engineering

2015

This thesis entitled:

Ultra-thin Materials from Atomic Layer Deposition for Microbolometers

written by Nathan Thomas Eigenfeld

has been approved for the Department of Mechanical Engineering

____

Prof. Victor M. Bright

____

Dr. George D. Skidmore

____

Prof. Y.C. Lee

____

Prof. Steven M. George

____

Prof. Juliet T. Gopinath

*Date*______________

The final copy of this thesis has been examined by the signatories, and we find that both the content and the form meet acceptable presentation standards of scholarly work in the above mentioned discipline.

Eigenfeld, Nathan Thomas (Ph.D., Mechanical Engineering)

Ultra-thin Materials from Atomic Layer Deposition for Microbolometers

Thesis directed by Prof. Victor M. Bright

Abstract:

This research focuses on the incorporation of atomic layer deposition (ALD) materials into microbolometer devices for infrared (IR) imaging. Microbolometers are suspended micro-electromechanical (MEMS) devices, which respond electrically to absorbed IR radiation. By minimizing the heat capacity (thermal mass) of these devices, their performance may be substantially improved. Thus, implementing ultra-thin freestanding ALD materials into microbolometer devices will offer a substantial reduction in the overall heat capacity of the device. A novel nanofabrication method is developed to produce robust ultra-thin suspended structures from ALD generated materials including W, Ru and Al_2O_3. Unique aspects of ALD such as high conformality offer the ability to create 3-dimensional structures with mechanical reinforcement. Additionally, the ability to tune residual stresses via atomically precise thickness control enables the fabrication of flat suspended structures. Since microbolometer elements are electro-thermally active, the electro-thermal properties of ultra-thin ALD W, Ru and Al_2O_3 are investigated. Several distinct deviations from bulk electro-thermal properties of resistivity, temperature coefficient of resistance, thermal conductivity and specific heat capacity are identified and interpreted with traditional nanoscale transport modeling and theory. For example, for ALD W, the electrical resistivity is increased by up to 99%, thermal conductivity is reduced by up to 91% and specific heat capacity increased 70% from bulk. Finally, the developed ALD nano-fabrication process and measured ALD material properties are combined to fabricate an

industrial level, state-of-the-art microbolometer pixel structure with 1.4X performance improvement. Further microbolomter performance enhancements based on the developed nanofabrication methods and electro-thermal measurements are discussed.

Dedication

I would like to dedicate this thesis to anyone with an open and willing mind to learn, those who pursue all avenues of life, not just scientific and those who humble themselves before nature, yet hunger for the tallest peaks.

The clearest way into the Universe is through a forest wilderness. – John Muir

Acknowledgements

First and foremost, I would like to acknowledge my advisor, Professor Victor M. Bright for his guidance and expertise surrounding high impact MEMS devices. I had almost no background in MEMS when beginning my graduate education and he gave me the opportunity to pursue my graduate degrees and further my knowledge in this exciting field of research. Without his continual support, this thesis would not have been possible. I would also like to thank my committee for allowing me to defend my work. I owe much gratitude for their time as well as their encouragement during the completion of this thesis. Additionally, I would like to acknowledge the Defense Advanced Research Projects Agency (DARPA), the Army Research Office (ARO) and DRS Technologies for funding this work.

Next, I would like to acknowledge Dr. George Skidmore from DRS Technologies. He served as my industry mentor, providing unsurpassed expertise on industrial level microbolometer devices. Detailed discussions regarding the fundamental operation of these devices inspired much of the work pursued in this thesis. Without his guidance, much of this work would not have been attempted or applied to industrial level state-of-the-art microbolometers.

I thank my family for giving me the opportunity to pursue knowledge from a young age. Without their encouragement through my years of intellectual development, I would not be where I am now. From my days in high-school choir, to my liberal arts undergraduate studies, to the intensively focused studies of graduate level mechanical engineering, they have always

provided me with the support to accomplish my goals. Without my family I would not be in the fortunate position I am today.

Several students and post-doctorate researchers deserve special recognition. Jonas Gertsch was essential in producing high quality atomic layer deposition thin films for my further study of their physical properties and application to microbolometer devices. Our collaboration was pivotal in the completion of this thesis. He will undoubtedly continue his excellent work in the pursuance of his own graduate degree in Chemistry. I would also like to thank Dr. Jason Gray for teaching me basic nano-fabrication processes and thin film characterization. Without him, my introduction to the clean room and experimentation would have been much less successful. Additionally, Dr. Joseph Brown helped me immensely during my first year as a graduate student. He provided detailed comments on my written assignments and guided my writing. Further, he was pivotal in helping me draft patent literature surrounding my work. I would also like to thank him for successfully proposing the seedling project for this work conveniently as I began graduate school and recommending me as a capable student. I would also like to thank the Victor Bright MEMS group for providing weekly feedback on my research progress for the entirety of my graduate degree.

I would also like to thank the staff of the Colorado Nanofabrication Laboratory and the Nano Characterization Facility at the University of Colorado Boulder. They provided the insightful comments and technical assistance regarding fabrication and characterization required to complete much of the work presented in this thesis.

Finally, I would like to thank my large circle of friends, which allowed me to pursue many extracurricular activities during my graduate studies. From backcountry skiing off the

rocky peaks of Colorado, to floating in deep Japanese powder, to epic mountain bike rides in the Moab desert, to “jolly” nights on Pearl St., they have been the backbone of my life outside engineering school. I credit them for my development of a healthy “work hard, play hard” lifestyle. In particular, I would like to thank my closest friends: Michael Chilton, Audrey Wilson, Erik Summerside, Peter O’Brien, Chris Stamper, Bre Stamper (Newell), James Cumming, Paul Schroeder, Paul Mountford and Charlie Miller. Without them, the massive concrete walls of the engineering center may have very well caved in on my own sanity.

Contents

Chapter 1

Introduction 1

1.1 Motivation 1

1.2 Scope and Application 3

1.3 Research Objectives 5

1.4 Organization of Dissertation 7

1.5 Summary of Resultant Publications and Patents 7

Chapter 2

Literature Review and State-of-the-Art 9

2.1 Atomic Layer Deposition 9

2.1.1 ALD Dielectrics 12

2.1.2 ALD Metals 13

2.1.3 ALD on Polymers 15

2.1.4 ALD in Industrial Applications 16

2.1.5 ALD in N/MEMS 18

2.2 IR Sensing 20

2.2.1 Theory of Detection 21

2.2.2 IR Sensors 22

2.2.3 The Microbolometer 24

2.2.4 Microbolometer Performance Figures of Merit 25

2.2.5 State-of-the-Art DRS Microbolometer 28

Chapter 3

Atomic Layer Deposition for Nano-devices 30

3.1 Ultra-thin 3-D Nano-devices from Atomic Layer Deposition on Polyimide 30

3.1.1 Fabrication Process 31

3.1.2 Nano-devices from ALD on Polyimide 33

3.2 Nano-device Mechanical Reinforcement and Stress Profile Tuning 33

3.2.1 Enhanced Stiffness via Trench Structures 33

3.2.2 Stress Gradient Tuning via ALD Thickness Variation in Al_2O_3/Ru/Al_2O_3 36

3.3 Experimental Information Surrounding ALD Nanofabrication Method 38

Chapter 4

Electrical and Thermal Property Measurement of ALD Nanolaminates 40

4.1 Fabrication of Sample Sets 41

4.2 Electro-thermal Measurement Methods 44

4.2.1 Electrical Resistivity Measurement 45

4.2.2 Temperature Coefficient of Resistance Measurement 46

4.2.3 Thermal Conductivity Extraction via Joule Heating Temperature Independent Electrical Conductivity Model 47

4.2.4 Thermal Conductivity Extraction via Joule Heating Temperature Dependent Electrical Conductivity Model 50

4.2.5 Specific Heat Capacity Extraction via Micropulse Calorimetry 52

4.3 Thermal Loss Calculations and Adjustments 56

4.4 Verification of Measurement Methods with Evaporated Aluminum 60

4.5 Grain Size Measurement 63

4.6 Experimental Circuit Diagrams for Electro-thermal Characterization 65

4.7 Uncertainty Analysis 66

Chapter 5

Electro-thermal Property Results of ALD W/Al_2O_3 and Ru/Al_2O_3 and Periodic W/Al_2O_3...... 68

5.1 Summary of ALD W, Ru, Al_2O_3 Sample Sets 69

5.2 Electrical Resistivity of ALD W and ALD Ru 70

5.3 Temperature Coefficient of Resistance of ALD W and ALD Ru 71

5.4 Thermal Conductivity of ALD W/Al2O3, ALD Ru/Al2O3 and Periodic ALD W/Al2O3 72

5.5 Specific Heat Capacity of ALD W/Al2O3, ALD Ru/Al2O3 and Periodic ALD W/Al2O375

5.6 Grain Sizes of ALD W and ALD Ru 79

Chapter 6

Interpretation of Electro-thermal Measurements of W/Al_2O_3 and Ru/Al_2O_3 and Periodic W/Al_2O_3 83

6.1 Parallel Layer Modeling.. 83

6.2 Traditional Nanoscale Transport Models.. 85

6.3 Grain Size Discussion 89

6.4 Electrical Resistivity in ALD W and ALD Ru.. 91

6.5 TCR in ALD W and ALD Ru 95

6.6 Thermal Conductivity of ALD Al_2O_3 99

6.7 Thermal Conductivity of ALD W and ALD Ru 102

6.8 Periodic W/Al_2O_3 Electrical Resistivity and Thermal Conductivity 108

6.9 Specific Heat Capacity of ALD Al2O3 and ALD W 112

6.10 Specific Heat Capacity of ALD Al_2O_3 and ALD Ru 116

6.11 Summary of Electro-thermal Results 117

Chapter 7

Application of Work to DRS Microbolometer 120
7.1 General Approach 120
7.2 ALD Umbrella 122
7.2.1 Fabrication 123
7.2.2 Stress Tuned Flat Umbrella 123
7.2.3 ALD Umbrella Results and Modeling 125
7.3 All-ALD Bolometer Approach 128
7.3.1 Structural Considerations of Support Leg 128
7.3.2 Electro-thermal Considerations of Support Leg 130
7.4 The Ideal DRS-style Bolometer 138
7.4.1 The Ideal Absorber 138
7.4.2 The Ideal Support Leg 141
Chapter 8
Conclusions/Future Work 144
8.1 Dissertation Summary 144
8.2 Envisioned Future Work 148

Figures

Figure 2.1 : Demonstration of binary ALD Al_2O_3 reaction chemistry and growth rate.[13] 10

Figure 2.2 : Demonstration of conformal ALD Al_2O_3 coating on high aspect ratio silicon trenches.[13] 11

Figure 2.3 : Nucleation of ALD W and ALD Pt. a) ALD W nucleates in ~ 5 – 10 ALD cycles through the formation of island clusters.[14] b) ALD Pt nucleates in ~ 40 cycles through the formation of island clusters.[15] 14

Figure 2.4 : Qualitative model of ALD film growth on polymer network.[26] 15

Figure 2.5 : Cross-sectional TEM image of a superlattice of ALD W and Al_2O_3 for X-ray reflectors.[10] W is the dark portion and Al_2O_3 the light portion. 17

Figure 2.6 : Underside ALD Al_2O_3 coating of silicon based micro-cantilever.[18] 18

Figure 2.7 : Micro-fabricated ALD Al_2O_3 pointer structure for stress measurement.[55] 19

Figure 2.8 : Suspended ALD devices. a) Micro-fabricated ALD W capacitive switch.[22] b) Micro-fabrication ALD Pt serpentine microbolometer.[24] 20

Figure 2.9 : IR spectrum relative to total spectrum (a) and characteristic IR image (b). 21

Figure 2.10 : Blackbody spectral radiance curves and atmospheric IR transmission. a) Full spectrum of blackbody radiation at relative temperatures. b) Spectral radiance of blackbody at 300K with peak wavelength of ~ 10µm. c) Atmospheric IR transmission of near, mid and LWIR bands. 23

Figure 2.11 : Microbolomer pixel with underlying support legs and transducing element with an absorption structure. 24

Figure 2.12 : Microbolometer performance curves of NETD vs. τ_{th}. Removing heat capacity shifts curve (improved red line). 28

Figure 2.13 : DRS-style two level microbolometer. Flat umbrella structure (left) and flat "holed" umbrella structure with reduced heat capacity (right). 29

Figure 3.1 : Fabrication processing overview. 32

Figure 3.2 : SEM images of a variety of fully released microstructures fabricated using the process from Figure 3.1a 34

Figure 3.3 : SEM images of freestanding structures that demonstrate the use of patterned trenches for structural control. 35

Figure 3.4 : Processing control of curvature.. 37

Figure 4.1 : TEM cross-section and SEM image of test structures. a) TEM cross-section image of Al_2O_3/W/Al_2O_3 coating on polyimide with similar thickness to the test structures.[34] b) SEM image tilted by 75° of an 80 x 2 μm suspended beam of Al_2O_3/W/Al_2O_3 with Al contact pads. 43

Figure 4.2 : Example XRR scan of Al_2O_3/Ru/Al_2O_3 indicating ~ 6.15 nm Al_2O_3 / 5.65 nm Ru / 6.15 nm Al_2O_3. 44

Figure 4.3 : Resistance versus beam length for 15.40 nm W beams. The linear fit is used to extract resistivity through equation 4.1. 45

Figure 4.4 : Normalized resistance change versus temperature for 7.9 nm Ru beam. The linear fit is used to extract TCR through equation 4.2. 46

Figure 4.5 : Relation of change in temperature versus joule heating input power for a 6.2 nm Al_2O_3/20.40 W/6.2 Al_2O_3 nanobridge. Thermal conductance G_{th} is extracted by a linear fit as the inverse of the slope. 49

Figure 4.6 . Relation of thermal conductance to length for a 9.8 nm Al_2O_3/20.40 W/9.8 Al_2O_3 cross-section nanobridge. Thermal conductivity is extracted by fitting the derived joule heating model (Equation 4.12) to the data. 50

Figure 4.7 : Resistance versus applied current squared for 6.7 nm Al_2O_3/7.9 nm Ru/6.7 nm Al_2O_3 nanobridge. Thermal conductivity is extracted by fitting equation 4.18 (red line) to the data. 52

Figure 4.8 : Raw current response data post voltage pulse at time zero. The red line is an exponential fit from which τ is extracted. 53

Figure 4.9 : Time constant data with respect to nanobridge length plotted as black squares. The data is fitted with the presented model (equation 4.22) and specific heat capacity extracted. 56

Figure 4.10 : The percentage of conduction attributed to air and radiation from the total measured thermal conductance of individual nanobridges. 58

Figure 4.11 : Adjusted thermal conductance values and total measured thermal conductance values with associated fits using the joule heating model from section 4.2.3. 60

Figure 4.12 : Relation of thermal conductance/bridge width to length for 100 nm Al film. Thermal conductivity is extracted by fitting the derived joule heating model (section 4.2.3) to the data. 62

Figure 4.13 : XRD data. a) Single peak fit on a 20 nm W ALD film. b) Multiple peak fitting on 20 nm W ALD film. 64

Figure 4.14 : Circuit diagram for resistivity, TCR and thermal conductivity measurement. 65

Figure 4.15 : Circuit diagram for specific heat capacity measurement. 66

Figure 5.1 : Electrical resistivity of single W and Ru ALD films and periodic ALD W films at room temperature. a) Thickness dependence of electrical resistivity of W and Ru films are plotted as black squares and red circles, respectively. b) Periodic layer dependence of electrical resistivity of W/ Al_2O_3 periodic layer stack with constant total thickness. 70

Figure 5.2 : Representative graphic of periodic W/Al_2O_3 structures from 1 – 4 layers with constant total thickness. 71

Figure 5.3 : TCR of W, Ru and periodic W/Al_2O_3 structures. a) TCR of W plotted as black squares and Ru plotted as red circles with respect to metal thickness. b) TCR of periodic W/Al_2O_3 plotted as black squares with respect to number of W layers denoted in Figure 5.2... 72

Figure 5.4 : Effective thermal condcutivities of $Al_2O_3/W/Al_2O_3$ plotted in black squares and $Al_2O_3/Ru/Al_2O_3$ plotted in red circles with respect to metal thickness. The legend denotes Al_2O_3 layer thicknesses for each sample. 73

Figure 5.5 : Effective thermal conductivity of periodic W/Al_2O_3 structures potted in black squares with respect to number of W layers as denoted in Figure 5.2............................. 74

Figure 5.6 : Effective thermal conductivity of Al_2O_3/20.40 nm/Al_2O_3 with respect to Al_2O_3 thickness on top and bottom plotted as black squares. 75

Figure 5.7 : Effective specific heat capacity of Al_2O_3/20.40 nm W/Al_2O_3 with respect to top/bottom Al_2O_3 thickness plotted as black squares. 76

Figure 5.8 : Effective specific heat capacity of 6.7 nm Al_2O_3/W/6.7 nm Al_2O_3 with respect to W thickness plotted as black squares... 77

Figure 5.9 : Effective specific heat capacity of 6.7 nm Al_2O_3/Ru/6.7 nm Al_2O_3 with respect to Ru thickness plotted as black squares. 78

Figure 5.10 : Effective specific heat capacity of periodic W/Al_2O_3 with respect to number of W layers denoted by Figure 5.2 plotted as black squares. 79

Figure 5.11 : Grain size relation to W ALD cycles (thickness).[37] Black square data points are from a single peak fit of GIXRD data. Red circle data points are from an averaged multiple peak fit of GIXRD data for various phases of ALD W. 80

Figure 5.12 : XRD data showing a multiple peak fit on a 8.0 nm ALD Ru film......................... 81

Figure 5.13 : Idealized schematic of grain structure and relative thickness in ALD W and ALD Ru with Al_2O_3 capping layers. a) ALD W/Al_2O_3 grain structure and relative thickness

with ~ 2 nm nuclation layer made up of disordered grains. b) ALD Ru/Al_2O_3 grain structure and relative thickness with ~ 1 nm nuclation layer. 82

Figure 6.1 : Qualitative model of electron and phonon conduction through polycrystalline films. Grain boundaries act as energy potential with strength *S* resulting in added phonon or electron resistance.[111] 87

Figure 6.2 : Temperature zone model for microstructural evolution during film growth.[115] Zone I, Zone T, and Zone II correspond to a T_s/T_m from 0 – 0.2, 0.2 – 0.4 and > 0.4, respectively. Layers a), b), c) and d) correspond to film thickness growth. 90

Figure 6.3 : Grain width versus film thickness for several ALD generated materials.[116] Each material has a different grain width saturation above 20-30 nm in thickness, but approximately identical linear relationships below 10 nm. 91

Figure 6.4 : Measured electrical resistivity of W films at room temperature at three thicknesses are plotted as black squares. The bulk W resistivity is shown as the blue dashed line. The upper bound FS model (p=0) is shown as the red dashed line. The solid black line is the thickness dependent MS model. 93

Figure 6.5 : Measured electrical resitivity of Ru films at room temperature at four thicknesses are plotted as black squares. The bulk Ru resistivity is shown as the blue dashed line. The upper bound FS model (p = 0) is shown as the red dashed line. The solid black line MS model from equation 6.7 for p = 0 and R = 0.49. The black dashed line is the MS model from equation 6.7 for p = 0 and R = 0.80. 94

Figure 6.6 : TCR of ALD W with respect to thickness plotted as black squares. The red line corresponds to a model fit by equation 6.16. 98

Figure 6.7 : TCR of ALD Ru with respect to thickness plotted as black squares. The red line corresponds to a model fit by equation 6.16. 99

Figure 6.8 : Effective thermal conductivity of Al_2O_3/W/Al_2O_3 with respect to top/bottom Al_2O_3 thickness plotted as black squares fit by equation 6.1 (red line). 101

Figure 6.9 : Data from Luo et al. and Lee et al. for the thermal conductivity of amorphous Al_2O_3.[104,107] a) Thermal conductivity of ALD Al_2O_3 at various thicknesses. b) Thermal

conductivity of amorphous Al_2O_3 deposited on different substrates by various techniques. 102

Figure 6.10 : Measured thermal conductivity of ALD W with respect to thickness plotted as black squares.[37] The black line is the bulk value. The red circles are WFL calculated κ_{el} values. The blue triangles are WFL calculated κ_{ph} values. The blue dashed line is the thickness dependent MS_{ph} model. 103

Figure 6.11 : Measured thermal conductivity of ALD Ru with respect to thickness plotted as black squares. The black line is the bulk value. The red circles are WFL calculated κ_{el} values. The blue triangles are WFL calculated κ_{ph} values. 104

Figure 6.12 : Calculated Lorenz numbers based off measured electrical resistivity and thermal conductivity for W (black squares) and Ru (red circles) with respect to film thickness. 108

Figure 6.13 : Periodicity dependence of thermal conductivity of W films at room temperature.[37] The black line is the bulk value. The red circles are WFL calculated κ_{el}. The blue triangles are WFL calculated κ_{ph}. The upside-down purple triangles are values modeled by the thickness depended MS_{ph} model. 111

Figure 6.14 : Effective specific heat capacity of Al_2O_3/20.40 nm W/Al_2O_3 at room temperature with respect to top/bottom Al_2O_3 thickness plotted as black squares. The red line corresponds to a model fit by equation 6.2. 112

Figure 6.15 : Specific heat of W/Al_2O_3 structures. The effective specific heat of 6.7 nm Al_2O_3/W/6.7 nm Al_2O_3 with respect to W thickness is plotted as black squares. The extracted specific heat of the W layer using equation 6.2 is plotted as red squares with respect to W thickness. 116

Figure 7.1 : DRS Tamarisk consumer model LWIR camera. 121

Figure 7.2 : DRS-style two level microbolometer. Flat umbrella structure (left) and flat “holed” umbrella structure with reduced heat capacity (right). Images were provided by DRS. 122

Figure 7.3 : TEM images of nominal ALD coating on polyimide for an umbrella absorption structure. 124

Figure 7.4 : SEM images of suspended membranes for microbolometer applications, with cross section of Al_2O_3 (blue) and W (yellow) (not to scale).[37] Only the top Al_2O_3 layer was varied in thickness. Identical W and lower Al_2O_3 layers are used in all three images. Each square structure is 16 µm × 16 µm. c) Nominal top and bottom Al_2O_3 thicknesses resulted in upward curl, while d) a top Al_2O_3 layer two times thicker resulted in downward curl. e) A flat structure was achieved with a 1.4 times nominal top Al_2O_3 layer and nominal bottom Al_2O_3 layer. Images in (c-e) were taken at 45° stage tilt angle. 124

Figure 7.5 : Comparison of proposed figure of merit, $Z_{B\text{-abs},}$ for single layer ALD Ru (black squares) and single layer ALD W (red circles) normalized to the 8.0 nm Ru film. Bulk Ru and bulk W normalized to bulk W are plotted as black dashes and red dashes, respectively. 127

Figure 7.6 : Comparison of proposed figure of merit, Z_B for single layer W (black squares) and periodic W layer structure (red squares) normalized to the 20.40 nm W or “single-layer” W structure. 133

Figure 7.7 : Comparison of proposed figure of merit, $Z_{B\text{-leg}}$ for single layer Ru (black squares) and single layer W (red circles) normalized to the 5.7 nm Ru film. Bulk Ru and bulk W normalized to bulk W are plotted as black dashes and red dashes, respectively. 135

Figure 7.8 : Comparison normalized thermal sheet resistance versus electrical sheet resistance for W and Ru. The data for Ru is plotted as black squares and W plotted as red circles. 135

Figure 7.9 : Comparison of normalized NETD with respect to normalized τ for several support leg optimization routes. The optimization begins with decreasing dielectric thickness, t_{Al2O3} and may then proceed by increasing l or decreasing κ and then increasing l. 137

Tables

Table 5.1: Summary of electro-thermal measurements sample set. 69

Table 6.1 : Summary of studied material properties for ALD W, Ru and Al_2O_3. 119

Chapter 1

Introduction

1.1 Motivation

Near the dawn of micro and nano-technology in 1959, Richard Feynman posed the question, "*Why cannot we write the entire 24 volumes of the Encyclopedia Britannica on the head of a pin?"*.[1] When discussing the decreasing scales of physical objects he stressed not only that there is "*room at the bottom*", but "*plenty of room at the bottom*". Soon after, the invention of the complimentary metal-oxide-semiconductor (CMOS) in 1963 would open the world of integrated circuitry (IC). Silicon batch fabrication methods revolutionized the production of ICs and soon IC technology was driving microprocessors in consumer and military industries. Moore's law would be identified as a definitive rate of improvement for the computing power of microprocessors stating that the number of transistors on a microchip would double every 18 months.[2] To maintain this rate, material dimensions continued to shrink in transistor elements. Today, we may be reaching the physical limits of scaled dimensions at sub-20 nm design rules and new materials or fabrication methods with interesting properties must be exploited by physicists and engineers alike to maintain improvement.[2]

Simultaneous to the IC technology revolution was a complementary revolution involving the development of small machines. As it turns out, the same silicon fabrication methods used to build circuitry could also be applied to mechanical devices. Silicon was identified as a promising mechanical material for a host of miniaturized transducing devices. Silicon was abundant, capable of thin, micron scale dimensions, shapeable, able to be batch fabricated by standardized lithographic and etching methods used in IC fields and easily integrated directly with underlying IC circuitry.[3] Micro-electro-mechanical systems (MEMS) would benefit directly from these developments in silicon fabrication methods. One major example of a silicon based MEMS device we encounter every day is an inertial sensor, which consists of a small silicon cantilever, fractions of a hair thick that deflects due to gravitational accelerations. Common inertial applications include airbag deployment during an automobile crash or display rotation in a variety of mobile electronic devices. As the field of MEMS progressed, other versatile materials including special semiconductors, metals and dielectrics allowed for more advanced devices and freedom of design.

Analogous to IC technology improvements, there is still "plenty of room at the bottom" for micro-machines. Benefitting from advancements in fabrication technologies in the IC fields, micro-machines have also scaled significantly following a "Moore's Law" of their own. Thin film deposition techniques and advances in surface micromachining have allowed for extremely thin film manufacturing and active materials are reaching dimensions which must be measured in nanometers. Further, it is not unforeseeable that new and exciting materials such as graphene and carbon nanotubes that are measured by single atomic layers will eventually be utilized as freestanding mechanical sensors, actuators or display devices in industrial applications. In many

cases, the smaller the better, as length scales begin to dominate physics and useful exploitations of these effects can drive development of higher performing devices.

Major hurdles to overcome in the development of ultra-thin MEMS or nano-electro-mechanical systems (NEMS) will include the manufacturability of the involved ultra-thin materials and their mechanical, electrical, thermal and optical properties. Additionally, ease of integration with current CMOS processing methods will dictate new technologies success rates as "time to market" metrics greatly impact near future consumer and military applications. Developing new ultra-thin materials and methods to easily build smaller and smaller machines is becoming increasingly important as relevant markets are demanding new and higher performance devices.

1.2 Scope and Application

Traditional bulk and surface micromachining techniques have provided a robust and diverse platform for the fabrication of microelectronics and micromachines or sensors.[3,4] Polymer applications in microfabrication processes are a subset of a growing trend of electrically, thermally, mechanically, and optically active organic material systems for flexible and stretchable electronics, organic light emitting diodes, and N/MEMS fabrication.[5–8] Spin-coated polymers such as polyimide or polydimethylsiloxane are easily moldable as flexible layers for micro-sensing devices or micro-fluidic channels.[6,9–11] Furthermore, dry etching of sacrificial polymers is very advantageous over traditional wet release of microdevices in microscale and nanoscale fabrication. The use of dry etching to release suspended structures at these scales avoids stiction and supercritical CO_2 processing.[12]

New nanotechnologies will require high performance and reliable inorganic and organic material interfacing to excel beyond traditional fabrication methods. Such a task is challenging due to the chemical and temperature sensitivity of many organic materials. High temperatures from chemical vapor deposition can cause a glass transition or thermal breakdown, while harsh conditions from plasma-assisted vapor deposition or sputtering can cause pinholes or degradation in the polymer. Additionally, many current deposition techniques face limitations in thickness control and film conformality and continuity at the nanoscale. Atomic layer deposition (ALD) is an increasingly popular thin film deposition method which uses a self-limiting binary reaction sequence that deposits films in discrete steps limited by surface site chemical reactions.[13–15] It produces continuous pinhole-free films with atomically controlled thicknesses, high conformality, and atomically smooth surfaces. These are essential properties as design constraints push device technologies to ever smaller sizes.[16,17] ALD-generated films on traditional microfabrication substrates have recently been applied to N/MEMS applications and will be reviewed in Chapter 2.[18–24]

Because ALD may be performed at low deposition temperatures and without high-energy ion bombardment, ALD on polymers avoids problems associated with other deposition techniques on polymers and thereby may enable a new generation of device fabrication. Inorganic ALD material generation on organic polymers has been found to be a reliable, scalable, and high-performing method utilizing aluminum oxide (Al_2O_3) as a model material.[25,26] Other materials are available in conformal ALD because Al_2O_3 is often used as a seed layer for the growth of metal, semiconducting and insulating layers including, but not limited to W, Ru, Pt, ZnO, TiO_2 and SiO_2.[14,15,27–30] Polymers may also be used as insulating layers, adhesion layers, thermal barrier layers, encapsulating bio-compatible gels, moldable substrates, flexible or

stretchable substrates. ALD materials have uses as electrical, mechanical, or optical layers for patterned N/MEMS, and may offer many advantageous coatings for gas diffusion applications and micro-system packaging.[31–33]

One example of the incorporation of ALD materials is in thermal sensing. Thinner active materials in thermal sensors such as microbolometers increase their sensitivity to absorbed infrared (IR) radiation and reduce power consumption of the pixel. By implementing ALD generated materials into existing pixel structures connected to CMOS circuitry an improved IR imaging device may be achieved. Performance metrics of these devices will be reviewed in Chapter 2. This is an exciting application of ALD for a high-performance imaging device and will be the focus of much of the work presented in this thesis.

1.3 Research Objectives

The primary focus of this research has been the development of a robust fabrication process involving ALD generated materials and to study several ALD material's electro-thermal and mechanical characteristics for the future implementation in microbolometer devices. However, the fabrication method and materials are not limited to microbolometer applications and may provide substantial design utility for other ultra-thin nano-devices. The major objectives of the research effort summarized in this thesis include:

1. Demonstration of a repeatable and extendable top-down fabrication method combining standard lithography and etching techniques with atomic layer deposition (ALD) generated ultra-thin films on polyimide substrates with three-dimensional features. The fabrication method is demonstrated in a variety of ALD materials including Al_2O_3, W and Ru with thicknesses on the order of 2 – 20 nm and in a

variety of two-dimensional patterns that include the first-ever two-story suspended ALD structures.

2. Demonstration of mechanical control of the associated ALD materials. Three-dimensional structural property control is achieved with three-dimensional molds that increased cantilever beam rigidity. Residual curl of cantilevers is observed in cantilevers of varied thicknesses and may be atomically tuned by ALD self-limiting reactions.
3. Utilization of the fabrication method developed to fabricate sample sets for the measurement of electro-thermal properties of a variety of ALD nanolaminates involving single metal layers and periodic metal layers. Modeling and discussion of these electro-thermal properties to shed light on the significant differences many nano materials exhibit relative to bulk traits. Studied ALD materials and properties include:
    a. W, periodic W/Al_2O_3 and Ru resistivity (Ω*m)
    b. W, periodic W/Al_2O_3 and Ru temperature coefficient of resistance (%/K)
    c. W/Al_2O_3, periodic W/Al_2O_3 and Ru/Al_2O_3 thermal conductivity (W/mK)
    d. W/Al_2O_3, periodic W/Al_2O_3 and Ru/Al_2O_3 specific heat capacity (J/gK)
4. Demonstration of an absorption structure for a microbolometer infrared light sensing pixel fabricated and tuned for flatness using angstrom-scale thickness control enabled by ALD.
5. Utilization of the measured material properties of ALD W/Al_2O_3 and ALD Ru/Al_2O_3 to estimate the performance enhancement of a microbolometer pixel via incorporation of ALD materials in the support legs and absorption structure.

6. Discussion of microbolometer component optimization in the context of identified mechanical and electro-thermal trends associated with the studied ALD materials.

1.4 Organization of Dissertation

The general motivation and research objectives have been presented in Chapter 1. The remainder of the thesis will include information relevant to the work described in the previous section. The second chapter includes a focused literature review of ALD, ALD materials and ALD in industrial applications to date. This chapter will also cover the basics of IR sensing and performance metrics that describe microbolometer IR sensing pixels. The third chapter will present a comprehensive description of the developed nanofabrication process and its relevant applications. It will also describe the mechanical control of associated ultra-thin materials. The fourth chapter will describe the electro-thermal measurement methods used to study ALD materials. Chapter 5 will present results of the electro-thermal measurements. Chapter 6 will interpret these measurements with classical transport models and provide a discussion of the nanoscale trends associated with the studied ALD materials. The seventh chapter will demonstrate the application of the developed nanofabrication process utilizing ALD materials to a microbolometer device and discuss device performance in the context of the nanoscale electro-thermal trends identified in Chapter 6. The finite mechanical tuning processes in regards to a microbolometer absorption structure are presented as well as estimations of performance increases via incorporation of ALD materials in the absorption structure. Finally, Chapter 8 will conclude and discuss future work surrounding this thesis.

1.5 Summary of Resultant Publications and Patents

Several first author publications and one US patent application have resulted from this work. The first publication surrounds the development of a nano-fabrication process utilizing

ALD generated materials on polyimide titled, "Ultra-thin 3-D nano-devices from atomic layer deposition on polyimide" and published in *Advanced Materials*.[34] This nanofabrication work was highlighted in the submission of US Patent Application # 14/604,906, 2014 under the title, "Novel Methods of Preparing Nanodevices".[35] The second first author publication was a conference paper presented at the premier MEMS conference, Transducers 2015 in Anchorage, AK surrounding the measurement of specific heat capacity of ALD W/Al_2O_3 titled, "Specific heat capacity of ultra-thin atomic layer deposition nanobridges for microbolometers".[36] The third first author publication surrounded the measurement of thermal conductivity of ALD W/Al_2O_3 and periodic W/Al_2O_3 structures titled, "Electrical and thermal conduction in ultra-thin freestanding atomic layer deposition W nanobridges" and published in *Nanoscale*.[37] Other work presented in this thesis surrounding the measurement of ALD Ru structures is also expected to result in a publication.

Chapter 2

Literature Review and State-of-the-Art

The following chapter presents a detailed literature review on ALD technology and associated materials as well as the fundamentals of IR imaging sensing and system optimization.

2.1 Atomic Layer Deposition

As stated previously in Chapter 1, ALD is an increasingly popular thin film deposition method. It uses a self-limiting binary reaction sequence that deposits films in discrete steps limited by surface site chemical reactions.[13–15] Precursor "A" is flowed over a substrate and reacts with available surface sites forming dangling bonds for the subsequent precursor "B" to react with, forming a desired chemistry. If each precursor is surface site limited, then each sequential reaction may proceed to build films one atomic layer at a time. Figure 2.1 demonstrates this alternating precursor process and thickness gains per cycle for ALD Al_2O_3. By its nature, the gas phase surface site limited reactions enable films to be built with extremely high conformality and minimal pin-holes.

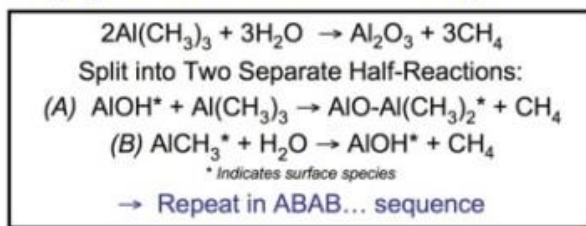

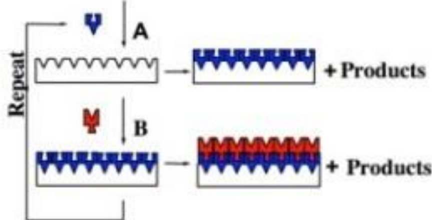

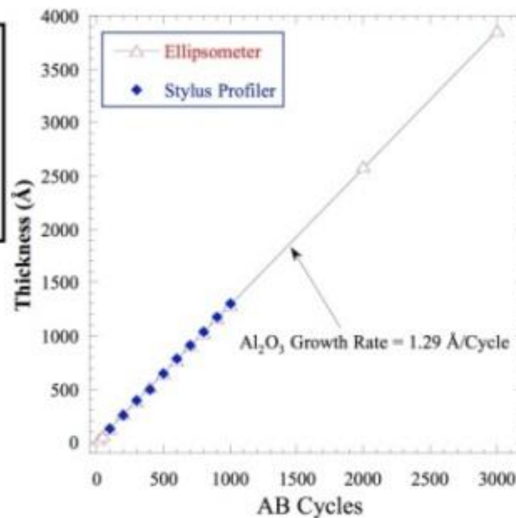

Figure 2.1: Demonstration of binary ALD Al_2O_3 reaction chemistry and growth rate.[13]

The idea of ALD can be dated back to the early 1960s under the name "molecular layering" by Prof. S. I. Kol'tsov from Leningrad Technological Institute.[38] Motivated by the desire to modify the surfaces of sorbents and catalysts, early Soviet Union scientists quantified the reaction between $TiCl_4$ and Si-OH groups on silica gel by titration and calorimetry, which later led to the demonstration of the formation of TiO_2 by sequential exposure of $TiCl_4$ and water. In the early 1970s ALD was further developed into a film deposition technique by Dr. Tuomo Suntola and co-workers under the term atomic layer epitaxy (ALE). The inspiration for the development of reactors to carry out the deposition technology was the need for high quality thin films in electroluminescent (TFEL) flat panel displays. Early reactors moved the substrate between different reactant sources (spatial ALD). Soon after, viscous flow reactors were developed, which remain today as high performance reactors allowing the swapping of molecular precursors through sequential gas flowing and purging to form a number of different dielectric, semi-metal and metal films during batch substrate coatings. ALD is inherently

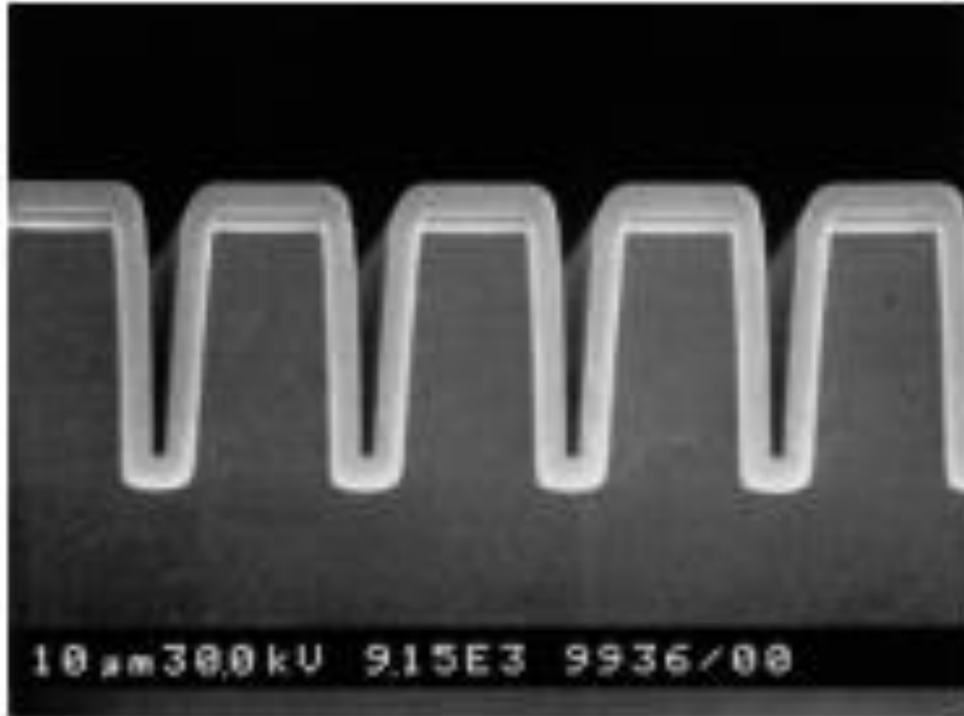

Figure 2.2: Demonstration of conformal ALD Al_2O_3 coating on high aspect ratio silicon trenches.[13]

different and more controllable than a common thin film deposition system known as chemical vapor deposition (CVD). In CVD the substrate is exposed to both precursors simultaneously while in ALD each precursor is flowed over the substrate individually wherein surface limited reactions occur.

Recently, thermal and plasma assisted ALD deposition systems have enabled the production of higher quality and larger variety of material films. Thermal ALD consists of heating a precursor source to a desired vapor temperature and flowing it into the reactor to achieve a specific reaction. Plasma or radical-enhanced ALD benefit single element depositions for many metals. Radicals such as hydrogen produced from a plasma source are used to provide

highly active molecules to reduce the metal or semi-metal precursors during half-reactions in the AB cycle.

2.1.1 ALD Dielectrics

ALD dielectric materials have important applications as electrical insulating layers, diffusion barriers, gap layers and protective coatings.[18,39,40] A model material for ALD dielectrics is Al_2O_3, which in its most general deposition chemistry utilizes trimethylaluminum (TMA) and H_2O, but may also utilize TMA and ozone. For the case of TMA and H_2O the surface chemistry during deposition can be described as,

$$\text{(A) } AlOH^* + Al(CH_3)_3 \rightarrow AlOAl(CH_3)_2^* + CH_4 \quad (2.1)$$

$$\text{(B) } AlCH_3^* + H_2O \rightarrow AlOH^* + CH_4 \quad (2.2)$$

where the asterisks denote the surface species. By alternating precursor A (TMA) and precursor B (H_2O) ALD growth occurs. The surface chemistry of Al_2O_3 has been studied by fourier transform infrared spectroscopy (FTIR) and results indicate clearly the loss of AlOH species and simultaneous gain of $AlCH_3$ species during the TMA reaction. For the H_2O reaction, FTIR indicates the loss of $AlCH_3$ species and simultaneous gain of $AlOH^*$ species. By repeating these surface reactions Al_2O_3 growth continues linearly with the number of AB cycles as demonstrated in Figure 2.1. Typical growth rates are 1.1 – 1.3 Å/cycle. Various methods to verify these rates have been employed and include, spectroscopic ellipsometry, quartz crystal microbalance (QCM) and x-ray reflectivity (XRR) methods.[13,26] Figure 2.2 demonstrates a conformal Al_2O_3 coating on high aspect ratio silicon trenches.

2.1.2 ALD Metals

Single element ALD metals offer many advantageous applications which require metallic properties such as light reflection/absorption, electron transport and heat dissipation, or as coatings for catalytic substrates and corrosive protection.[10,41,42] Also, they are often exploited as seed layers for high aspect ratio electro-plating processes.[27] Common ALD metals include Ru and Pt due to their high electrical conductivity, but W is also a common material and has recently been used in a high performance X-ray mirror and a free-standing mechanical structure due to its high atomic number and high strength.[10,22,27] ALD W is based on the reduction of WF_6 by Si_2H_6. The Si_2H_6 reaction occurs by a two-step process and the overall AB process may be described as,

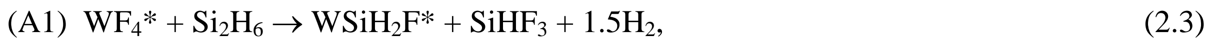

$$\text{(A1)}\quad WF_4^* + Si_2H_6 \rightarrow WSiH_2F^* + SiHF_3 + 1.5H_2, \qquad (2.3)$$

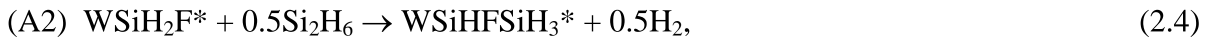

$$\text{(A2)}\quad WSiH_2F^* + 0.5Si_2H_6 \rightarrow WSiHFSiH_3^* + 0.5H_2, \qquad (2.4)$$

$$\text{(B)}\quad WSiHFSiH_3^* + 2WF_6 \rightarrow WWWF_4^* + 2SiF_4 + 1.5H_2 + HF, \qquad (2.5)$$

where the asterisk denotes surface species. In general, initial ALD cycles of W produce islands which eventually coalesce and recrystallize to minimize surface energy after 5 – 10 ALD cycles as demonstrated in Figure 2.3a. Once nucleated, deposition rates vary from ~ 3.8 – 4.0 Å/cycle. Often Al_2O_3 is used as a seed layer to promote the nucleation of the W. Al_2O_3 is also utilized as a capping layer to protect against W oxidization to WO_3.[25]

ALD Ru is also a common ALD metal which usually uses thermally assisted ALD to help activate a number of metal reducing precursors.[27] For example, a commercial Beneq TFS 200 reactor system may deposit Ru by using thermally activated $Ru(EtCp)_2$ at 110 °C and O_2 for

growth at ~ 0.4 Å/cycle. Similar to the W, a layer of Al_2O_3 may be deposited to promote nucleation of the Ru.

ALD of Pt is a great example of an ALD chemistry which benefits from plasma assisted ALD. By utilizing (methylcyclopentadienyl)-trimethyl platinum ($MeCpPtMe_3$) and O_2 plasma as

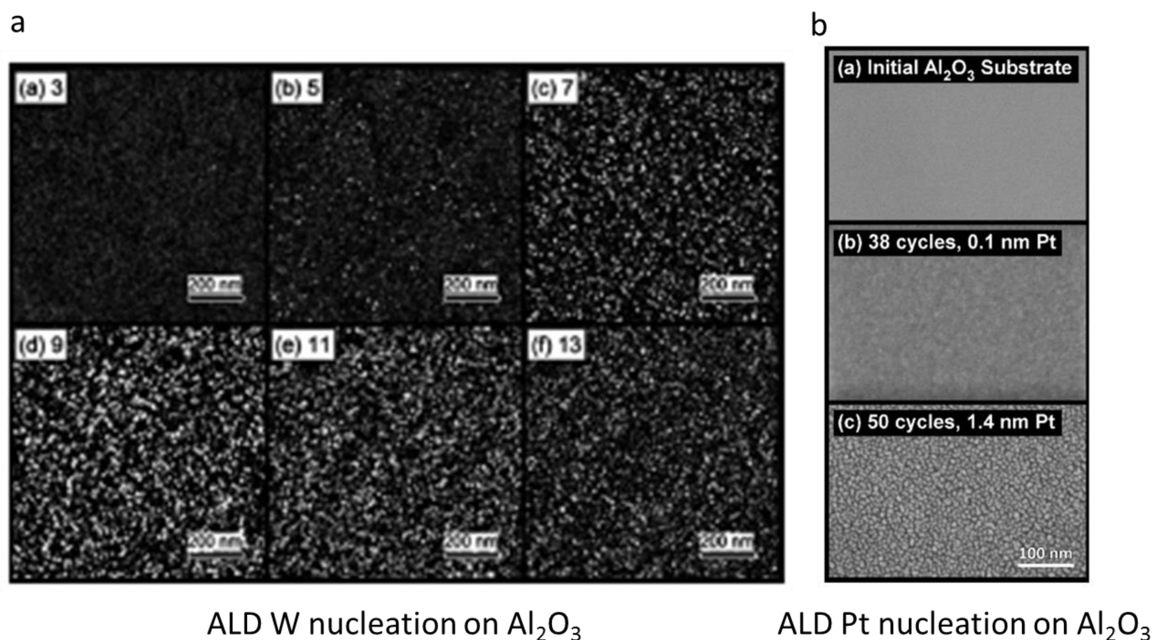

Figure 2.3: Nucleation of ALD W and ALD Pt. a) ALD W nucleates in ~ 5 – 10 ALD cycles (top right labels) through the formation of island clusters.[14] b) ALD Pt nucleates in ~ 40 cycles through the formation of island clusters.[15]

the reactants, ALD Pt was able to nucleate on ALD Al_2O_3 in ~ 40 cycles.[15] Figure 2.3b demonstrates the nucleation process of Pt on ALD Al_2O_3, which when compared to W, is much longer. The W nucleation phase may be faster due to a higher chemical interaction with the Al_2O_3 substrate and Si_2H_6 reactant, whereas Pt growth contains a less efficient interaction between $MeCpPtMe_3$ and surface hydroxyl groups.[14,15] In general, plasma assisted ALD Pt promotes more rapid nucleation of Pt when compared with thermal ALD Pt by providing a more

active form of O_2 during reactions. Plasma assisted Pt deposition may also utilize a H_2 plasma source.[15]

2.1.3 ALD on Polymers

ALD on polymers has a plethora of applications in flexible coatings, gas diffusion barriers and robust fabrication processes.[8,32–34] Specifically, roll-to-roll applications could offer

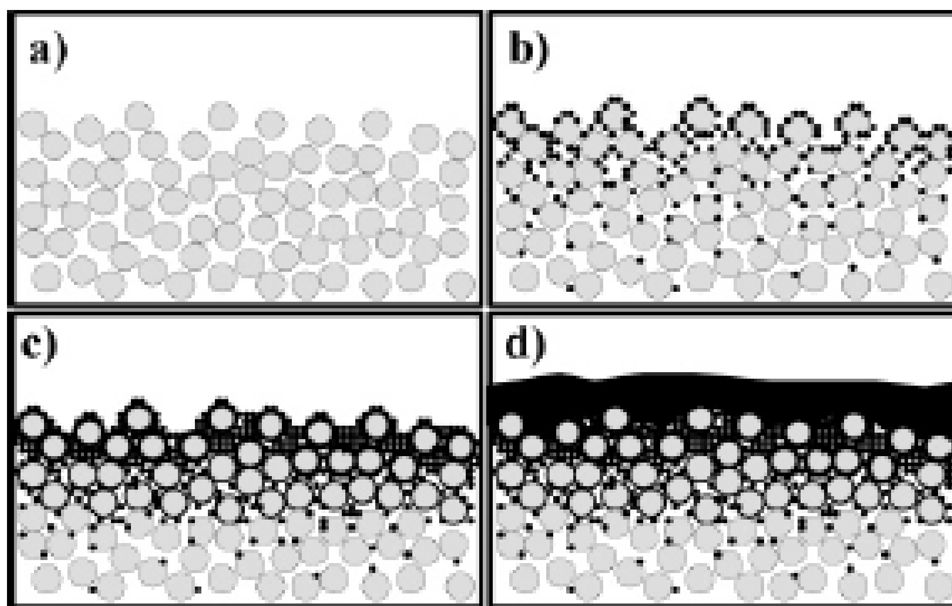

Figure 2.4: Qualitative model of ALD film growth on polymer network.[26]

extreme utility in the printed electronics industry.[43] Given polymer surfaces are often absent of functionalized chemical groups, ALD on polymers was initially foreseen as extremely difficult. However, the nucleation of ALD Al_2O_3 and other metal-oxides on polymers is routinely accomplished and do not require specific chemical groups on the polymer surface. This process may be best described as a quasi-CVD process wherein the precursors penetrate the polymer network and mix together. The reaction may be carried out in the following steps: reactant diffusion, reactant retainment, ALD chemistry cluster formation and ALD cluster coalescence to form a continuous ALD film.[25,26] Figure 2.4 demonstrates a model for Al_2O_3 ALD growth on a

non-functionalized surface polymer network. For functionalized polymer surfaces, ALD nucleation is routine. Nucleation of ALD Al_2O_3 and other materials has been demonstrated on a host of relevant polymer surfaces including, but not limited to, polyimide, polymethyldisiloxane, polystyrene (PS), polypropylene (PP), poly(methylmethacrylate) (PMMA), polyethylene (PE), or poly(vinyl chloride) (PVC); polyesters such as polycaprolactone; proteins, polysaccharides and other biopolymers.[25,26,34] Recently, polyimide has been used to enable a robust fabrication process for ALD enabled NEMS devices and will be described in section 3.1.[34]

2.1.4 ALD in Industrial Applications

After the invention of ALD, its only publically acknowledged commercial application would be TFELs for the next 20 years. TFELS are used in many transparent display systems such as heads-up car displays.[44] These devices consist of thin film laminates of insulator-luminescent-insulator, which must withstand high electric fields to provide luminescence. ALD offered low pin-hole films such as ZnS:MN for the luminescent layers and Al_2O_3 or Al_xTi_yO for the insulators.[44] Following TFELs in the 1990s silicon-based microelectronics demanded higher quality and highly controlled thin films as Moore's law was identified and design rules continued to shrink every 18 months. The potential for scaling thin films with ultra-high conformality was an incredible utility. Other thin film deposition systems would fail at producing conformal pin-hole free films at extremely thin thicknesses. This was detrimental for metal-oxide field effect transistors as low quality films would produce leakage currents through gate dielectrics and transistors would begin to waste enormous amounts of power as they continued to shrink.[2,45,46] ALD offered high dielectric constant materials at extremely thin thicknesses to combat this leakage current with shrinking dimensions.[44,46,47] Other ALD enabled microelectronics include dynamic random access memory devices (DRAMS). These devices improve with increased

capacitance, which may be achieved by a decrease in dielectric thickness, increase in dielectric constant and increase in active capacitive surface area by the introduction of 3-dimensional shapes. ALD offered outright improvement in all the performance considerations previously listed – extremely thin dielectric materials such as Al_2O_3, TiO_2, ZrO_2 and HfO_2 with high dielectric constants and extreme conformality for complex capacitor arrangements.[48] Soon, ALD began permeating complementary markets, which also benefited from extremely high quality thin films.

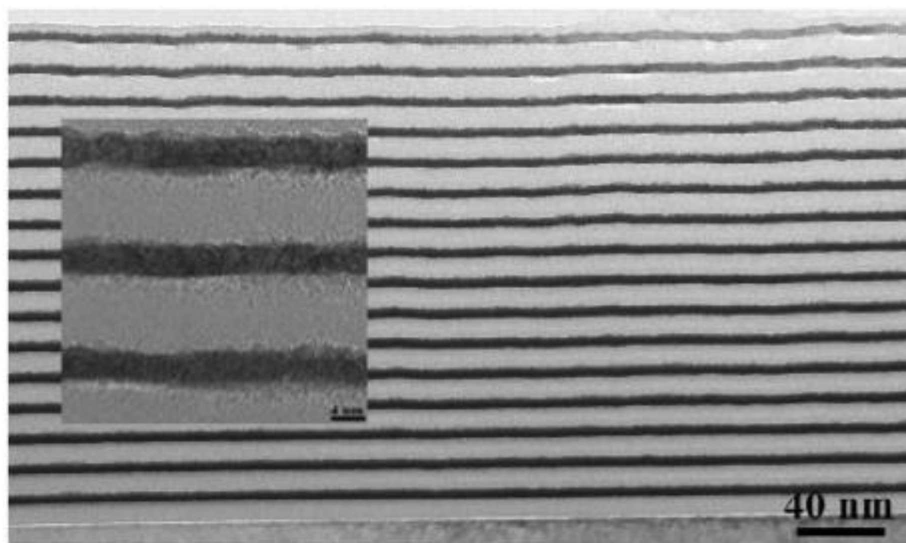

Figure 2.5: Cross-sectional TEM image of a superlattice of ALD W and Al_2O_3 for X-ray reflectors.[10] W is the dark portion and Al_2O_3 the light portion.

Other applications of ALD generated films include gas diffusion barriers, wear protective coatings, optical coatings, or as active suspended structures.[10,18,19,21–24,34,41,42,44,49–58] ALD gas diffusion applications actually date back to the original TFEL displays where protective ALD layers would prevent outdiffusion from soda lime glass. Other pertinent gas diffusion barrier applications are for organic light-emitting diode (OLED) devices, that may lead to highly efficient displays fabricated on flexible polymeric substrates for little cost.[8,32,33] These devices require extremely low diffusion rates for O_2 and H_2O, which can destroy the devices. Single

layers of Al_2O_3 may achieve extremely low H_2O transmission rates of ~1 x 10^{-3} $g/m^2/day$.[33] Further, applying multilayer laminates of Al_2O_3 and SiO_2 may lower the H_2O transmission rate to as low as 1 x 10^{-5} $g/m^2/day$ by filling in possible pin-holes from underlying layers.[32] Multilayer laminates may also be used to achieve supreme optical properties. Figure 2.5 demonstrates a nanolaminate of W/Al_2O_3 that achieved an ultra-high X-ray reflectivity of 96.5% at a 0.154 nm wavelength for applications in X-ray mirrors. This is attributed to the extreme smoothness of the ALD films,

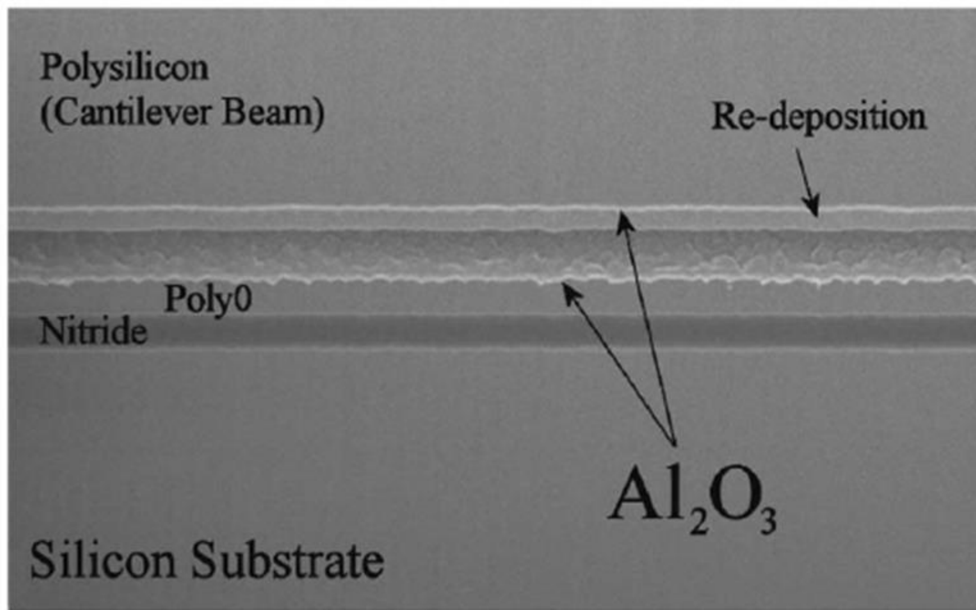

Figure 2.6: Underside ALD Al_2O_3 coating of silicon based micro-cantilever.[18]

which are precisely fabricated as Bragg reflector. High performance X-ray diffraction lenses are also possible by ALD's precise thickness control, smoothness and multi-layer capability.[41]

2.1.5 ALD in N/MEMS

ALD also provides many benefits for active N/MEMS devices as both protective coatings and as active material layers in suspended structures. One common application of ALD Al_2O_3 is for an anti-wear, anti-stiction and anti-shorting coating for suspended MEMS structures.[18] Since

ALD is completely conformal, it ensures film coverage on all sides of a released MEMS device assuming the gas diffusion during the deposition cycling allows the precursor agents to reach complex surfaces. This allows the coating of the underside of suspended structures. Figure 2.6 demonstrates a protective Al_2O_3 coating on a released polysilicon MEMS structure. It may also be used to increase the stiffness of suspended devices increasing pull-down voltages.[18]

Recently, suspended ALD films have been utilized as structural materials in resonators, mechanical switches and microbolometer elements.[21,22,24,56] The structural properties of ALD Al_2O_3 have been studied to enhance design utility for ALD films in N/MEMS. Figure 2.7

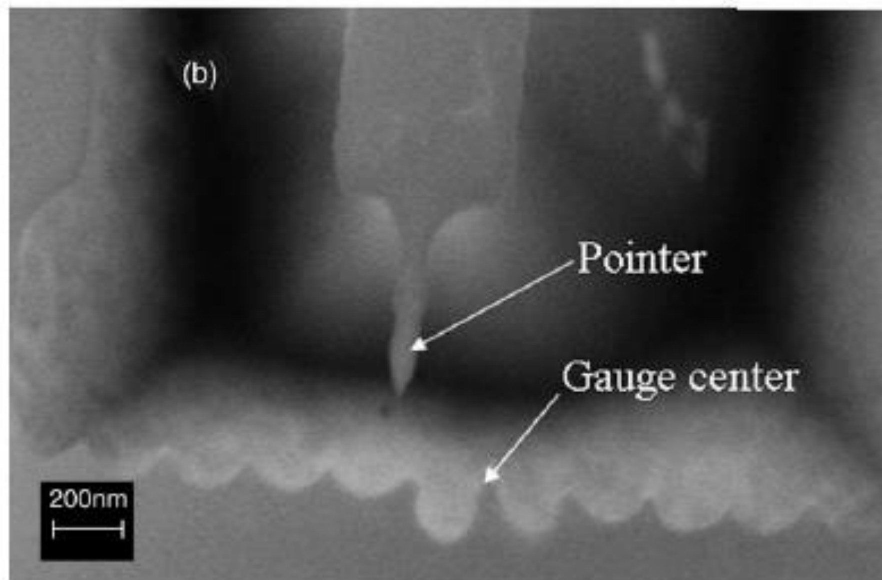

Figure 2.7: Micro-fabricated ALD Al_2O_3 pointer structure for stress measurement.[55]

demonstrates a micro pointer structure utilized to investigate stresses in 50 nm Al_2O_3 layers. The Young's modulus and residual tensile stress for Al_2O_3 on silicon substrate has been recorded as 168 – 182 GPa and 383 – 474 MPa, respectively.[20] Figure 2.8a demonstrates a capacitive ALD W CMOS compatible switch. This work demonstrated ALD W as a capable structural material for use in the field of NEMS.[22] Often a thin layer of ALD Al_2O_3 is utilized to achieve faster

nucleation of a single element metal layer. This technique has also been used in the construction of free-standing ALD Pt serpentine resistors for applications in IR sensing (Figure 2.8b).[24,42] Utilizing ultra-thin materials allows for a higher sensitivity to IR radiation. Since ALD in N/MEMS is an infant field, many applications of ALD may still be trade secret. However, there is little doubt that within the next 20 years, active ALD films will permeate N/MEMS to further improve micro and nano-devices alike.

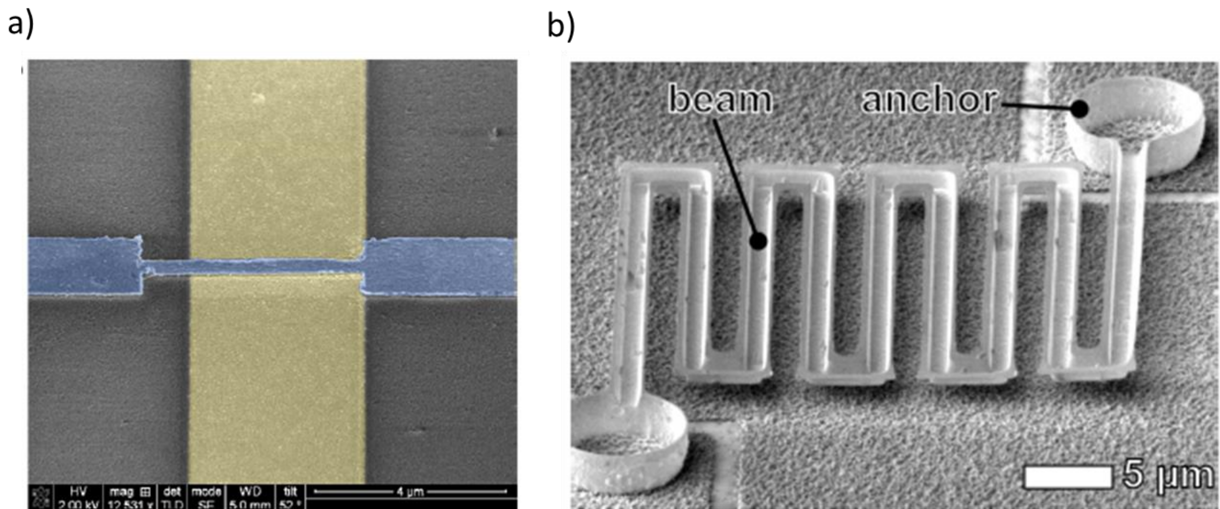

Figure 2.8: Suspended ALD devices. a) Micro-fabricated ALD W capacitive switch.[22] b) Micro-fabrication ALD Pt serpentine microbolometer.[24]

2.2 IR Sensing

Imaging beyond the visible light spectrum into the infrared (IR) allows for a host of multi-spectral imaging applications in fields including, but not limited to industrial, military, and commercial. Specifically, monitoring of facilities and machinery, aerial surveillance, night vision, automotive collision avoidance, weapon detection and non-invasive medical imaging are important applications driving the improvement of many IR imaging devices. Figure 2.9a

demonstrates the large portion of IR light outside the visible spectrum including near, mid and long-wave IR (LWIR) regions and Figure 2.9b shows characteristic IR images. There is no color because the wavelengths in question are not from the visible spectrum in which the human eye operates. The image is a mapping of relative temperature differences within the field of view of the imaging device.

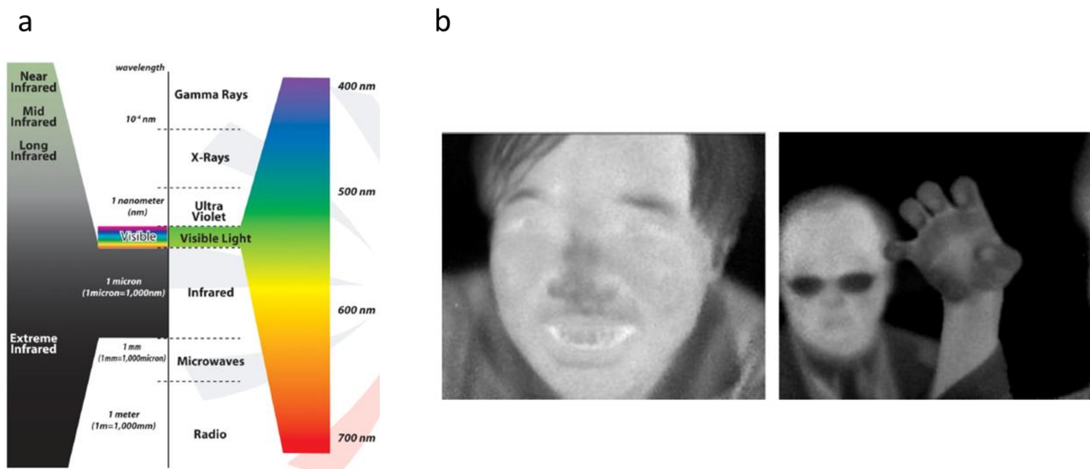

Figure 2.9: IR spectrum relative to total spectrum (a) and characteristic IR image (b).

2.2.1 Theory of Detection

All objects emit radiation that depends on their temperature and how closely they resemble a blackbody; an idealized physical object that absorbs all incident electromagnetic radiation. The degree to which blackbodies emit radiation is governed by what is known as Planck's law. This law dictates the spectrum of emitted radiation relative to the blackbody's absolute temperature. The spectral radiance is given as,

$$Planck(T,\lambda) = \frac{2\pi \cdot c^2 \cdot h}{\lambda^5 \cdot \left(exp\left(\frac{hc}{kT\lambda}\right) - 1\right)} \frac{Watts}{cm^2 \cdot steradian \cdot \mu m}, \tag{2.6}$$

where λ is the wavelength of light. Blackbodies at various temperatures will have different spectral curves as demonstrated in Figure 2.10a. For example, the spectrum for a body at 300K is demonstrated in Figure 2.10b that peaks in radiance at ~ 10 μm.

In an idealized vacuum, all wavelengths would be transmitted at 100% over infinite distance, however this is not the case when trying to image within earth's atmosphere. Various wavelengths encounter strong attenuation by the atmosphere and thus may not be easily sensed. Figure 2.10c demonstrates the transmission of spectra in the near, mid and LWIR. Because of this atmospheric attenuation, sensors are designed to detect specific wavebands, or even multiple wavebands.[59]

Humans may be considered blackbodies at 300K and thus, many sensors are designed for imaging in the LWIR corresponding to a peak wavelength of ~ 10 μm. These sensors are able to detect differential spectral radiance between bodies at different temperatures, i.e. humans and their background environment. Differential Planck blackbody radiation is the derivative of Planck radiation with respect to temperature and is given as,

$$DPlanck(T,\lambda) = \frac{2\pi \cdot c^2 \cdot h \cdot exp\left(\frac{hc}{kT\lambda}\right)}{k \cdot T^2 \cdot \lambda^6 \cdot \left(exp\left(\frac{hc}{kT\lambda}\right) - 1\right)^2} \frac{Watts}{cm^2 \cdot steradian \cdot \mu m \cdot K}. \tag{2.7}$$

This definition is more descriptive of the instantaneous power radiated from a blackbody between small variations in temperature.

2.2.2 IR Sensors

At present, IR imagers encompass two categories of operation, photoconductive and thermal. Photoconductive detectors, such as Quantum Well Infrared Photodetectors (QWIPS) or photodiode devices, are considered single stage transducers. They operate on the immediate

electrical detection of individual photon interactions with a material lattice.[59] Two stage transducers operate on the conversion of IR radiation to detectable heat.[60–63] Such devices include microbolometers, micromechanical sensors, pyroelectrics, thermopiles and Golay cells.[60,64] Modern IR sensing devices must be easily fabricated, large format compatible, low in power consumption, light-weight, easily integrated with

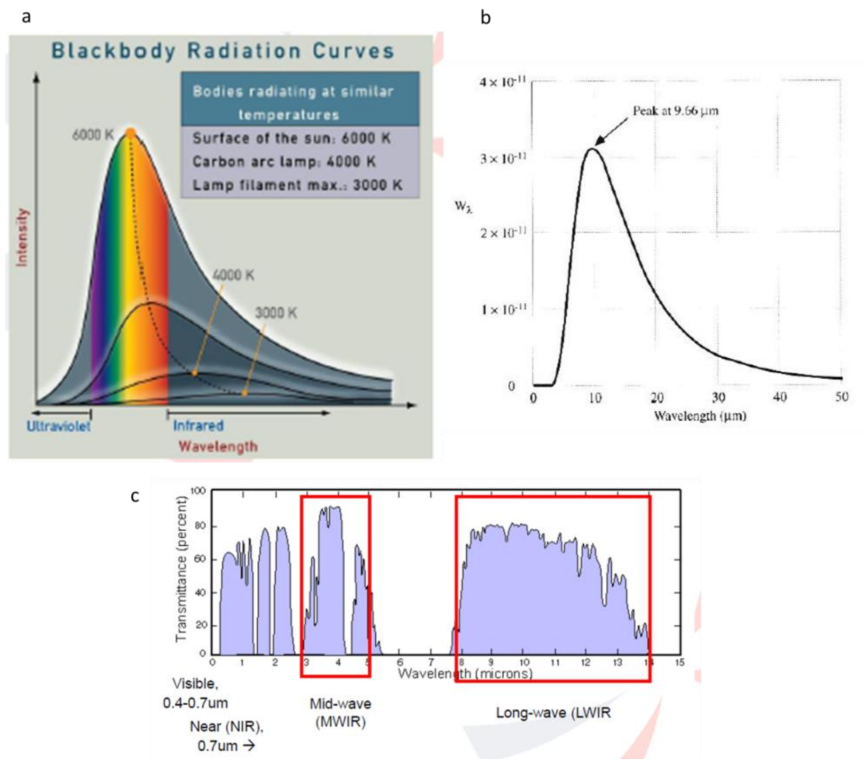

Figure 2.10: Blackbody spectral radiance curves and atmospheric IR transmission. a) Full spectrum of blackbody radiation at relative temperatures. b) Spectral radiance of blackbody at 300K with peak wavelength of ~ 10μm. c) Atmospheric IR transmission of near, mid and LWIR bands.

existing CMOS circuitry elements, highly sensitive, fast in response and low in noise. QWIPS and high performance photo-diode devices often require sufficient cooling for operation, making them bulky and cost ineffective. Pyroelectric, micromechanical sensors, thermopile and Golay cells struggle to compete with existing uncooled microbolometer's high performance and simple

operation for standard imaging applications. Thus, the uncooled microbolometer has emerged as the market leading IR imaging device.

2.2.3 The Microbolometer

The microbolometer is a temperature sensitive electrical resistor that absorbs IR radiation (thermal energy) and heats up, producing a measurable change in resistance (Figure 2.11). In general, the microbolometer may be broken into four elements: an IR absorber, a temperature

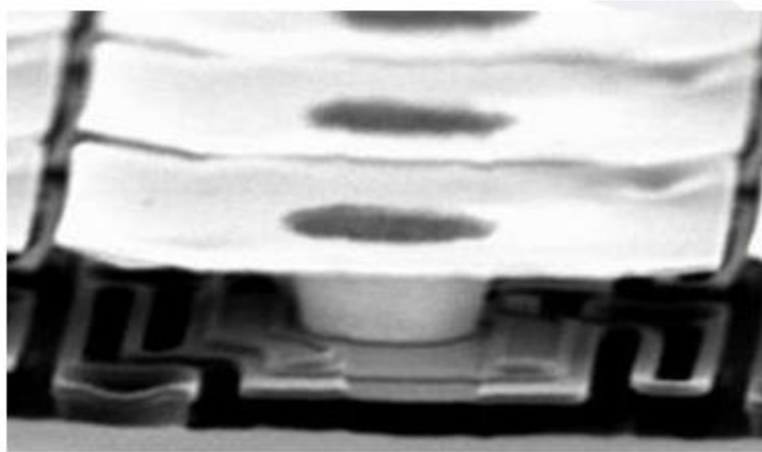

Figure 2.11: Microbolomer pixel with underlying support legs and transducing element with an absorption structure.

sensitive transducer, thermally isolating mechanical support legs and CMOS pixel readout circuitry. The transducing material often consists of vanadium oxide (VO_x), amorphous silicon (α-Si) or silicon diodes.[65] These elements are designed to produce a large change in resistance when heated, often on the order of 2 – 4 %/K. This resistance change is detected by a constant or pulsed bias voltage.[60] The IR absorber is typically a thin metal film with a sheet resistance (resistivity × film thickness) designed to absorb a specific IR band, often for imaging in the LWIR of 8 – 14 μm wavelengths.[23,62,63,66] The thermally isolating mechanical support legs provide suspension for the free-standing transducing and absorbing elements and thermal isolation from the underlying substrate. Though bolometers are not required to be suspended

devices, their performance is increased by thermal isolation from the substrate. They also provide an electrical connection between the transducer and readout integrated circuitry (ROIC). Support legs are designed to have minimal thermal conductance to the substrate in order to maximize the signal produced in the transducing element caused by absorbed IR radiation. Often an underlying IR reflector is included to maximize IR absorption through the creation of an optical absorption cavity between the reflector and absorber.[62] For example, thin metal films are generally limited to no more than ~ 50% absorption in the LWIR by the Woltersdorff thickness relation, but with the addition of a reflector, absorption coefficients may reach higher than 90%.[62,67,68]

2.2.4 Microbolometer Performance Figures of Merit

Microbolometers are measured mainly by two figures of merit (FOM); noise equivalent temperature difference (NETD) and the thermal time constant (τ_{th}). The noise equivalent temperature difference is the minimum resolvable temperature difference between two side-by-side blackbodies that produces a signal-to-noise ratio of unity in the ROIC. Standard values for high-performance devices are ~ 50 mK. The NETD follows the relation:

$$NETD = \frac{Noise}{Response} = \frac{Noise \cdot G_{th}}{TCR \cdot (\beta \cdot \varepsilon \cdot A) \cdot V_b}, \tag{2.8}$$

where *Noise* consists of the total noise of the bolometer including noise from Johnson heating, temperature fluctuation, inherent 1/f noise and ROIC noise, G_{th} is the thermal conductance, *TCR* is the temperature coefficient of resistance, β is the fill factor of the absorber, ε is the emissivity or absorption coefficient of the bolometer, A is the area of the pixel and V_b is the bias voltage. NETD is a metric where less is better and may be minimized by several approaches. One approach is to optimize the ROIC through reducing its noise as well as the overall applied

voltage, which in turn may affect Johnson noise. However, on a more fundamental level of pixel performance, thermal conductance should be minimized, while TCR, absorption and fill factor maximized. By optimizing the latter properties, the largest response to absorbed infrared radiation may be achieved. The area of the pixel is pushed smaller and smaller by the demand for higher resolution sensors with more pixels at smaller overall sensor sizes and should not be considered a free parameter in the overall design of the pixel.[69]

The second FOM, the thermal time constant, is a measure of response time for the absorbed infrared imaging and follows the relation:

$$\tau_{th} = \frac{C_{th}}{G_{th}}, \tag{2.9}$$

where C_{th} is the heat capacity of the bolometer. NETD and τ_{th} are trade-offs since they have a reciprocal relation with thermal conductance. One may design a high-speed imaging bolometer (low τ_{th}) with a large NETD or a low-speed imaging bolometer (high τ_{th}) with a small NETD simply by varying the thermal conductance of the pixel. This trade-off effect is often governed by support leg design, i.e. increasing the length, or decreasing width or thickness to decrease G_{th}, lowering the NETD, but increasing τ.

Recent work has pushed for a new figure of merit, the product of NETD and τ_{th}:

$$NETD \cdot \tau_{th} = \frac{Noise \cdot \cancel{G_{th}} \cdot C_{th}}{TCR \cdot (\beta \cdot \varepsilon \cdot A) \cdot V_b \cdot \cancel{G_{th}}}. \tag{2.10}$$ [70]

This FOM is a much better description of the geometry independent performance of a bolometer pixel since G_{th} is mostly a function of cross-sectional area and length of the support legs. In the case of equation 2.10, the product of NETD and τ_{th}, heat capacity becomes the fundamental

performance metric, assuming TCR and absorption are maximized. By reducing the heat capacity of the bolometer the frontier of bolometer performance is improved. Figure 2.12 demonstrates NETD versus τ_{th} with absolute values removed. For the "improved" curve, heat capacity was removed, shifting the curve, or "frontier" of performance. After removing heat capacity, thermal conductance may be tuned to reduce NETD or τ_{th} respectively. In general, for 30 Hz imaging devices τ_{th}'s are on the order of 5 – 15 ms, or a third of the frame rate (upper bound for standard imaging devics).[60] Thus, an optimization process may proceed as follows:

1. Reduce heat capacity, lowering the thermal time constnt (shift from blue to red curve Figure 2.12)
2. Redesign pixel's support leg structure to reduce the thermal conductance, raising the thermal time constant towards the upperbound, reducing NETD (movement along blue or red curve Figure 2.12).

Removing heat capacity negates the trade-off effect in bolometer performance and pushes the frontier of device performance. Further discussion of optimizaiton will be presented in Chapter 7.

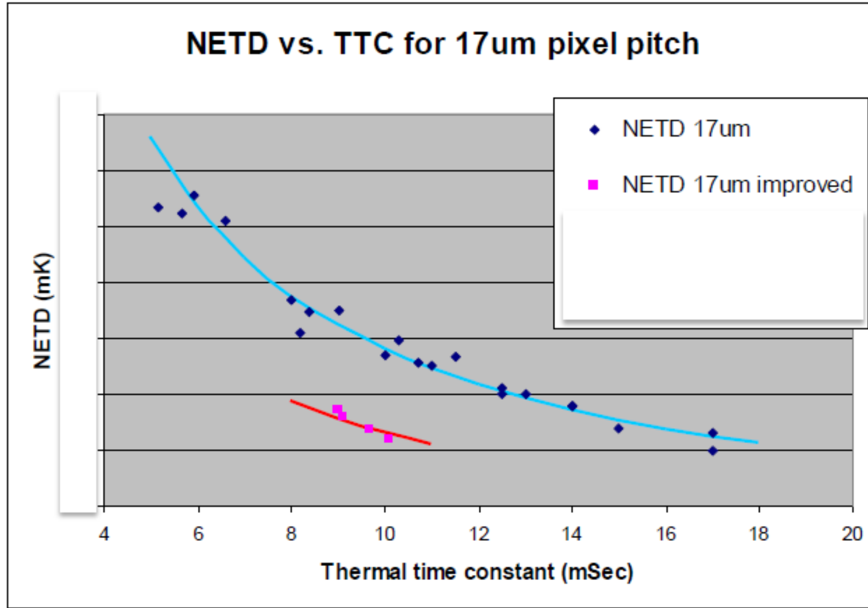

Figure 2.12: Microbolometer performance curves of NETD vs. τ_{th}. Removing heat capacity shifts the curve or "frontier" of performance (improved red line).

2.2.5 State-of-the-Art DRS Microbolometer

Figure 2.13 demonstrates a DRS two-layer uncooled bolometer structure consisting of an umbrella absorber structure connected to an underlying VO_x transducer and support leg elements for imaging in the LWIR. The absorber consists of a thin metal absorber with an optimized sheet resistance and protective dielectric layers. DRS uses a two-level structure to optimize fill factor to absorb the maximum amount of incident IR radiation. Placing the absorption structure above the support level frees up lateral real-estate for more aggressive support leg designs as seen in the right of Figure 2.13. This is an especially important design utility as pixel areas will continue to decrease with the demand for higher resolution, smaller and lower power consumption sensors, which result in smaller and more light-weight optical housing units for the camera.[69,70] The umbrella structure forms an optical cavity with an underlying metal reflector to maximize absorption in the structure.[70] Further, DRS has optimized this structure to improve bolometer

performance by removing lateral material in the umbrella to reduce the overall heat capacity (right of Figure 2.13). In doing so, the umbrella maintains > 90% IR absorption in the LWIR by maintaining an optimal sheet resistance in the metal absorber.[66] This technique capitalizes on the interaction of electromagnetic waves with solid matter. Since the LWIR wavelengths are ~ 8 – 14 µm, sub 5 µm recesses or channels in the absorption structure appear absent to the absorbed IR radiation. Further improvements to the umbrella structure and support legs could result in an even higher performance DRS microbolometer pixel. For the purpose of this dissertation the discussion of pixel improvements will be limited to the umbrella and support leg structures and will be discussed in Chapter 7.

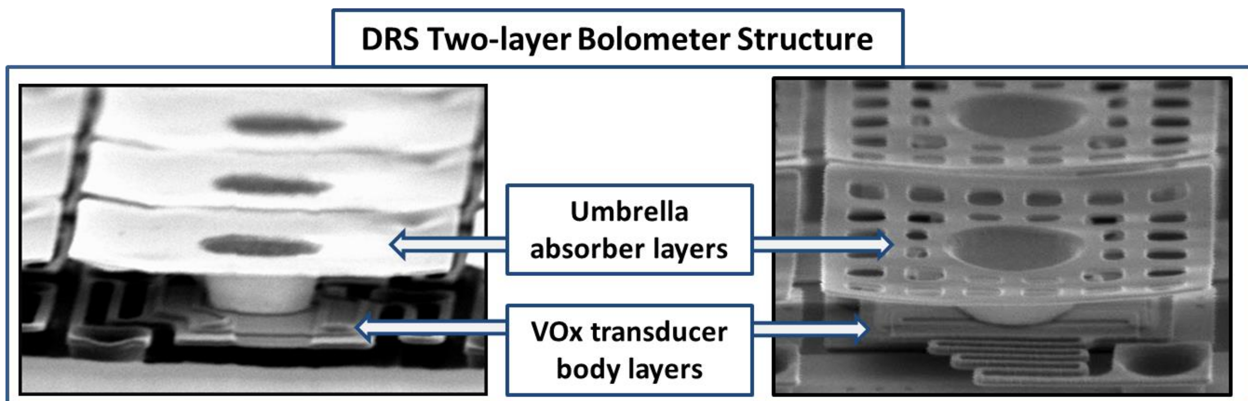

Figure 2.13: DRS-style two level microbolometer. Flat umbrella structure (left) and flat “holed” umbrella structure with reduced heat capacity (right).

Chapter 3

Atomic Layer Deposition for Nano-devices

The following chapter describes work published in *Advanced Materials* titled, "Ultra-thin 3D Nano-Devices from Atomic Layer Deposition on Polyimide," and work included in US patent application # 14 604 906, 2014 titled, "Novel Methods of Preparing Nanodevices".[34]

3.1 Ultra-thin 3-D Nano-devices from Atomic Layer Deposition on Polyimide

Efforts to improve upon current N/MEMS with continually shrinking dimensions and increased performance require new processing and fabrication techniques. Recently, bottom-up and top-down fabrication methods have shown unique advancements in applications of nanoscale polymeric structures in hierarchical arrangements.[71] However, fabrication methods, which incorporate both inorganic and organic materials, will offer a more versatile platform for N/MEMS fabrication and nanotechnology advancement. This section of the thesis demonstrates a repeatable and extendable top-down fabrication method combining standard lithography and etching techniques with ALD generated ultra-thin films on polyimide substrates with three-dimensional features. This fabrication method was demonstrated in a variety of active ALD

materials including Al_2O_3, W and Ru with thicknesses on the order of 10 nm and in a variety of two-dimensional patterns that included two-story suspended structures.

3.1.1 Fabrication Process

Figure 3.1 demonstrates the ALD on polyimide fabrication process. An initial electrical layer may be deposited on a bare Si wafer by evaporation of aluminum and lift-off patterning. Next, a polyimide layer is processed. An adhesion promotion chemical, VM-651 is applied to the fabrication substrate and polyimide is spun onto the adhesion layer. The resultant structure is then cured at elevated temperatures. Thicknesses of the polyimide layer using this process are ~ 2.5 μm – 4.5 μm. Vias and trenches are both etched utilizing a thermally evaporated aluminum mask (Figure 3.1b), which is patterned using negative photoresist and lift-off processing. The polyimide etch is done using anisotropic reactive ion etching (RIE) with O_2 plasma. The aluminum mask is removed in aluminum etchant. Next, ALD deposition occurs on the polyimide layer. $Al_2O_3/W/Al_2O_3$ ALD is performed at 130 °C in a custom reactor.[14,26] $Al_2O_3/Ru/Al_2O_3$ ALD is performed in a Beneq TFS 200 commercial reactor at 300 °C.[27] The Al_2O_3 uses trimethylaluminum (TMA) and H_2O as gas precursors for growth at ~0.13 nm/cycle. The W uses Si_2H_6 and WF_6 as gas precursors for growth at ~0.384 nm/cycle. Ru uses thermally activated $Ru(EtCp)_2$ and O_2 at 110 °C as gas precursors for growth at ~0.04 nm/cycle. The nucleation of Al_2O_3 forms an initial interfacial layer different from bare Si/SiO_2 substrates possibly due to limited ALD precursor infiltration of the polyimide. In general, this slightly lengthens the nucleation period and results in a skin layer of polyimide/Al_2O_3 which remains unstudied. This

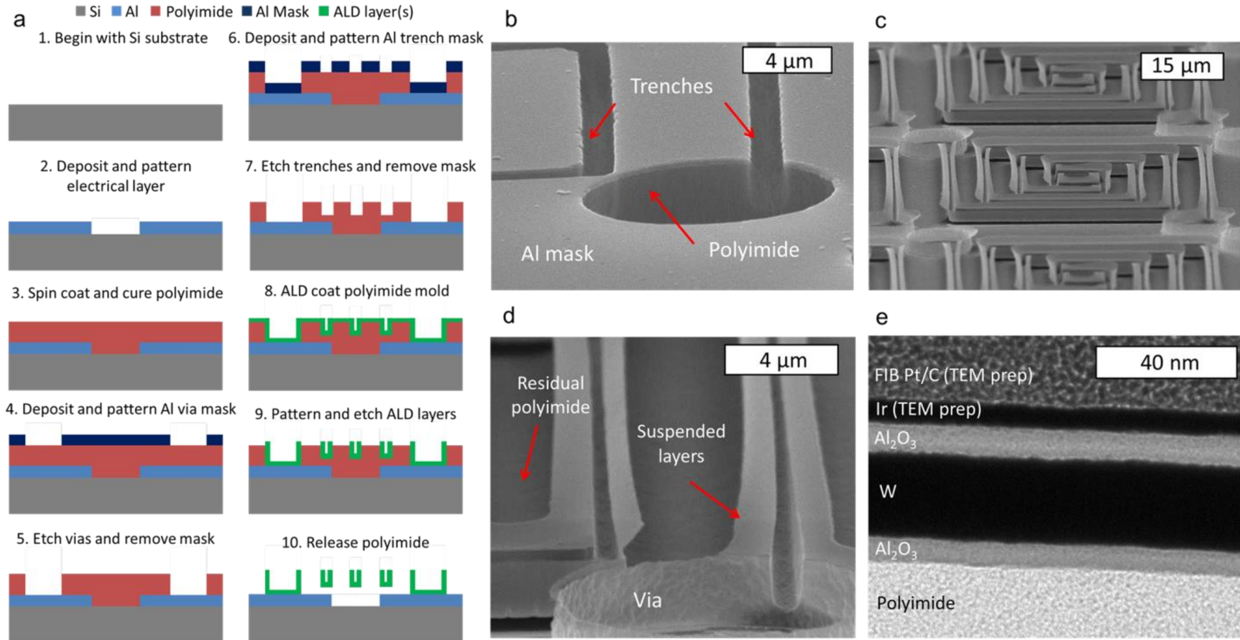

Figure 3.1: Fabrication processing overview. a) Fabrication process steps 1–10 with descriptions. The process may be extended to multiple levels by repeating steps 3–9 before finishing with release step 10. b) Etched polyimide mold of vias and trenches with aluminum mask. The via is nominally 3 µm deep and open to the underlying metal layer and connected to a 1.5 µm deep trench pattern. c) Partially released structures consisting of 2.2 nm Al_2O_3/18 nm W/2.2 nm Al_2O_3. The ALD layers coat the via and trench mold from (b). d) Magnified view of a portion of the structures in (c). e) TEM cross-sectional image of an Al_2O_3/W/Al_2O_3coating on polyimide with similar thicknesses to (c) and (d). All images in (b-d) were taken with an SEM at a 75° stage tilt angle.

skin layer may be discernable in TEM images, but further investigation is required. Growth after nucleation remains highly linear.[26] Next processing of the ALD films is required. The ALD lithography is accomplished using a positive photo-resist. Each ALD film is etched by anisotropic RIE using fluorine-based chemistry. The photoresist is removed in an acetone bath. Next a gentle release process is required to protect the ALD films from damage. The ALD films are released by removing the polyimide by an isotropic oxygen plasma at 150 W and ~10 Torr in a microdevice asher. Figure 3.1c and Figure 3.1d demonstrate a partially released ALD structure with trench insets and anchors.

3.1.2 Nano-devices from ALD on Polyimide

By utilizing standard lithography methods in this process, batch fabrication of any pattern that can be achieved with micro or nanolithography is possible. A variety of patterns with suspended ALD laminates with W and Ru surrounded by Al_2O_3 may be seen in Figure 3.2. Figure 3.2b demonstrates an array of Al_2O_3/W/Al_2O_3 structures curled upwards, potentially useful for engineered 3-D metamaterials.[10,72,73] Figure 3.2c and Figure 3.2e demonstrate flower petal patterns for potential applications such as nano-trapping systems for single cell biological testing platforms.[74,75] Flat structures are also achievable through stress balancing or additional mechanical reinforcement (Figure 3.2d and Figure 3.2f). Achieving mechanically robust and flat structures will be discussed in the following sections.

3.2 Nano-device Mechanical Reinforcement and Stress Profile Tuning

N/MEMS devices continually face mechanical issues surrounding residual stress effects from both intrinsic film stress and fabrication conditions. To suspend flat or specifically curled structures, control over the mechanical properties of these active thin films is vital. This is particularly important for application to microbolometer structures which require a flat absorption structure and a stiff supporting structure.

3.2.1 Enhanced Stiffness via Trench Structures

Motivated by prior work with polysilicon ALD coated trench molds, control of mechanical properties by incorporating a three-dimensional mold in the sacrificial polyimide layer was demonstrated.[23,24] Figure 3.3 demonstrates the effect of a trench in structural reinforcement of fixed-free cantilevers. Without the trench (Figure 3.3a), the large bi-axial stress curls the cantilevers. With the addition of the trench in the cross section (Figure 3.3b), the device

stiffness was substantially increased. For a flat beam with thickness t, width b, and effective Young's modulus E_{eff}, the flexural rigidity EI about the x–axis is given as,[76]

$$EI_{flat} = E_{eff}bt^3/12. \tag{3.1}$$

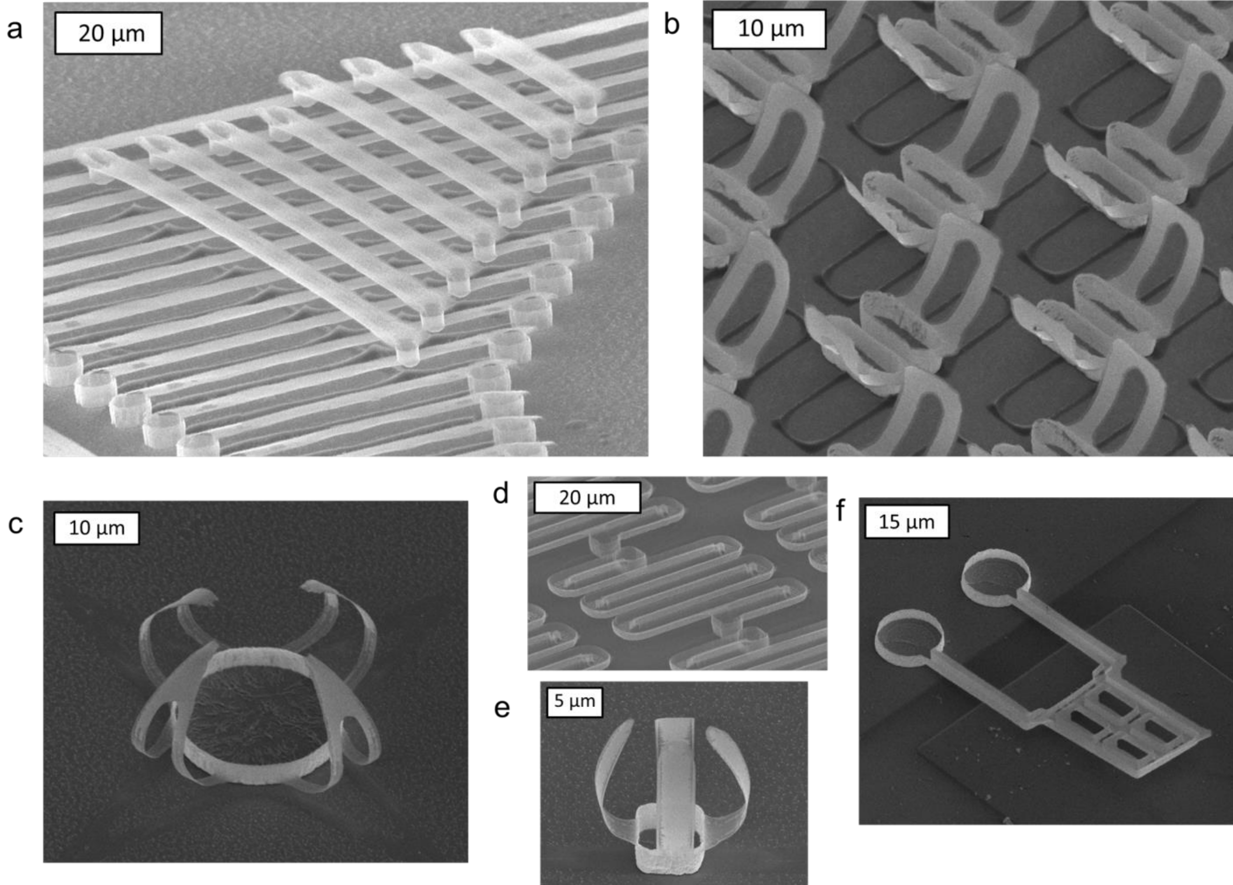

Figure 3.2: SEM images of a variety of fully released microstructures fabricated using the process from Figure 3.1a. a) Two-story suspended fixed-fixed cantilever structures comprised of 5.5 nm Al_2O_3/2.5 nm Ru/5.5 nm Al_2O_3 fabricated from the extended process outlined in Figure 3.1a. The second level vias are etched to the underlying first level patterned nanostructures and the deposition and patterning repeated. b) Array of meta-material-like structures comprised of 5.5 nm Al_2O_3/18 nm W/5.5 nm Al_2O_3. c) Curled structures comprised of 5.5 nm Al_2O_3/5 nm Ru/7.7 nm Al_2O_3. d) Microbolometer-like structure with trench, comprised of 5.5 nm Al_2O_3/5 nm Ru/7.7 nm Al_2O_3. e) Curled structure comprised of 5.5 nm Al_2O_3/5 nm Ru/7.7 nm Al_2O_3. f) Micromechanical paddle structure comprised of 2.2 nm Al_2O_3/18 nm W/2.2 nm Al_2O_3. Images (a) and (d) were taken at a 60° stage tilt angle and (b),(d),(e) and (f) at a 45° stage tilt angle.

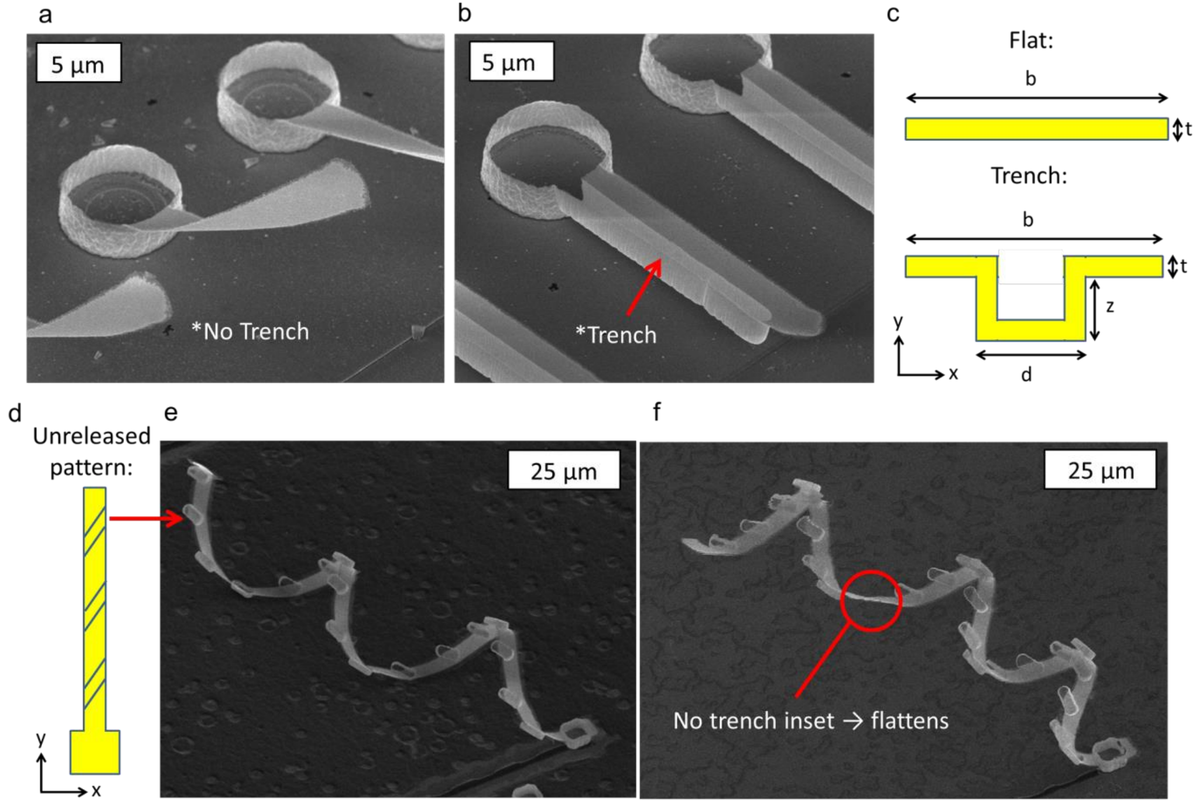

Figure 3.3: SEM images of freestanding structures that demonstrate the use of patterned trenches for structural control. a) Fixed-free cantilever comprised of 2.2 nm Al_2O_3/18 nm W/2.2 nm Al_2O_3. b) Fixed-free cantilever with same dimensions as (a), but with trench included to maintain mechanical flatness. c) Example of beam cross-sections for flat and trench structures. d) Example of alternative trench layouts for targeted stress relief control in (e) and (f). e) Helical structure comprised of 5.5 nm Al_2O_3/5 nm Ru/7.7 nm Al_2O_3 based off the design from (d). f) Helical structure with missing trench, demonstrating flattening control of cantilever structure where inset is missing. All images were taken at 45° stage tilt angle.

For a channel section with depth z and width d (Figure 3.3c), the y–axis centroid coordinate C_y, channel area A, and flexural rigidity about the x–axis of the full trench structure from the bottom of Figure 3.3c EI_{trench}, are given as,[76]

$$C_y = \frac{2z^2t+(d-2t)t^2}{2zd-2(d-2t)(z-t)}, \tag{3.2}$$

$$A = 2tz + (d-2t)t, \tag{3.3}$$

$$EI_{trench} = E_{eff}\left[\frac{1}{12}(b-(d-2t))t^3 + \frac{1}{3}\left((d-2t)t^3 + 2tz^3\right) - AC_y^2\right]. \quad (3.4)$$

The first term in the brackets of EI_{trench} accounts for the moment of inertia of the flat overhang sections of the trench and the rest for the moment of inertia for the trench. For example, the flexural rigidity of the trench inset beam from Figure 3.3b for a stress free structure with d = ~1.5 μm and z = ~1.6 μm, is ~10^4 times larger than the flat beam in Figure 3.3a with the same width, thickness and effective Young's modulus. This trench method may be used to ensure mechanical flatness when other optical, thermal or electrical performance constraints require film thicknesses or material combinations that would produce curled release structures without the trench. Additionally, the trench process may be used to induce targeted physical shapes such as three-dimensional helices as depicted in Figure 3.3e. Trench insets placed in angled increments along the cantilever structures (Figure 3.3d) forced the structure to spiral upon release (Figure 3.3e and Figure 3.3f).

3.2.2 Stress Gradient Tuning via ALD Thickness Variation in Al_2O_3/Ru/Al_2O_3

Figure 3.4a shows the suspension of laminate fixed-free cantilevers of varying length. Four chips underwent identical ALD growth and processing conditions, but with varied Ru thicknesses from ~ 1.5 nm – 5 nm and outer Al_2O_3 layers with constant 5.5 nm thicknesses. To reduce anchor influence, the fabrication process from Figure 3.1a was abbreviated by excluding vias and trenches to release ALD structures anchored directly to polyimide. Cantilever curl magnitudes from suspended arrays on each chip were measured and Figure 3.4b shows the relation between curl and Ru thickness. With atomically controlled ALD material thicknesses, a desired curl level, i.e. high curl for a self-assembled structure, or no curl for a traditionally flat MEMS device structure, may be obtained by atomically tuning material thicknesses.

Only recently have ALD material mechanics with thicknesses on the order of 50 – 100 nm been investigated for single materials, leaving models for laminate structures at < 5 nm thicknesses absent in the literature.[20] Intrinsic stresses such as Volmer-Weber grain growth

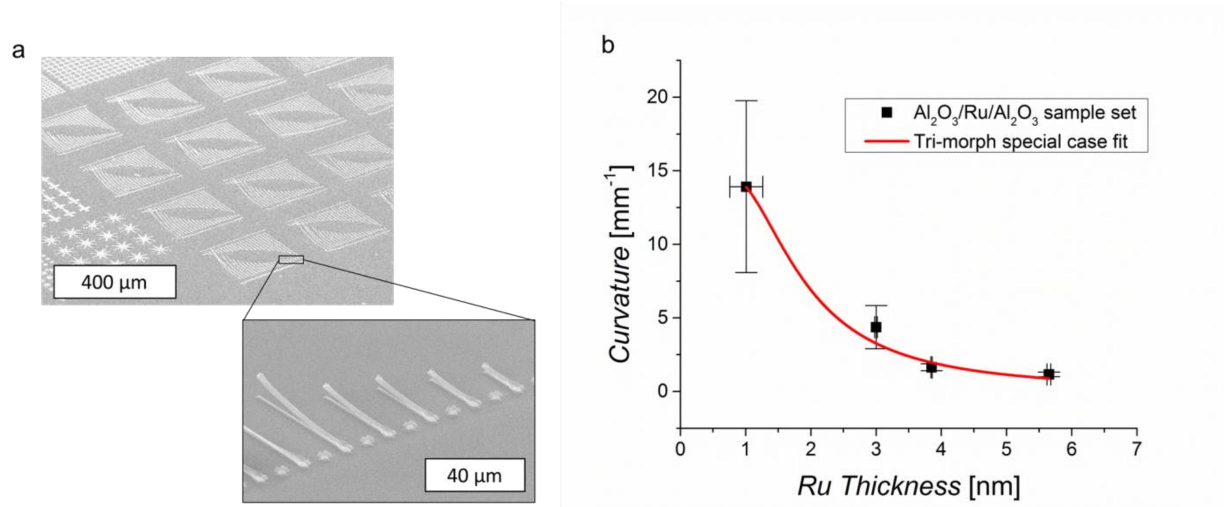

Figure 3.4: Processing control of curvature. a) Example of suspended Al_2O_3/Ru/ Al_2O_3 fixed-free cantilever arrays for curl measurements. Inset shows magnified view of curled structures anchored to polyimide. Both SEM images were taken at 60° stage tilt angle. b) Cantilever curvature relates to thickness measured from samples depicted in (a).

stress, surface interface stress and grain boundary stress are present in these ALD laminates, which are a combination of amorphous and nano-crystalline structures.[77] To best fit the data in Figure 3.4b, the stress-based curvature for a trimorph cantilever with identical top and bottom material layers was derived.[78] For this trimorph special case, the curvature is given as the following:

$$\kappa = \frac{6t_3(t_2+t_3)\Delta\sigma_{1-3}}{E_2^2t_2^3+2E_3t_3\left(3t_2^2+6t_2t_3+(3+E_3)t_3^2\right)}\,. \tag{3.5}$$

Here, subscripts denote the layer number of the tri-layer stack counting up from the bottom layer and $\Delta\sigma_{1\text{-}3}$ denotes the stress difference between layer 1 and 3. The fitted value for $\Delta\sigma_{1\text{-}3}$ is several orders of magnitude larger than expected for standard thin film laminates when fitted with

known material thicknesses and material elastic moduli as free parameters capped at bulk values. Because this model lacks detailed consideration of surface stresses associated with nucleation phases of each ALD layer, surface roughness and actual Young's moduli of these ALD films it is not a complete description of the curled cantilever structures described here. Further investigation of ultra-thin film laminate stress specific to ALD generated materials including effects of growth temperature and precursor dosages, is needed for more detailed modeling. For the purpose of this thesis, discussion of the mechanical modeling of such stresses will be excluded, however, the engineering utility of thickness dependent stress tuning will be discussed later in the fabrication of micro-bolometer elements.

3.3 Experimental Information Surrounding ALD Nanofabrication Method

Curl measurement: Curl was measured with a Zygo white light interferometer by scanning arrays of released cantilevers with a 50 mm working distance objective. Each cantilever's length and deflection was measured with the interferometer's built-in software. Assuming $l << \kappa^{-1}$,[79] curl was calculated from the following:

$$\kappa = 2z/l^2, \tag{3.6}$$

where z is the vertical deflection and l the length of the cantilever. Statistical and measurement uncertainties were combined and reported with 95% confidence in the intervals shown in Figure 3.4b.

ALD thickness measurement: The deposited ALD film thicknesses were measured from dummy wafers inserted in the reaction chambers during ALD, by use of X-ray reflectometry (XRR) on a Bede D1 X-ray diffractometer (Bede Scientific Ltd.). The X-ray wavelength for

measurements was 1.54 Å, corresponding to the *Ka* transition in the Cu x-ray tube. The Bede REFS software was used to fit the XRR data and extract the error in thickness.

Chapter 4

Electrical and Thermal Property Measurement of ALD Nanolaminates

Work presented in this chapter surrounds the experimental methods of publications titled "Electrical and thermal conduction in ultra-thin freestanding atomic layer deposition W nanobridges" published in *Nanoscale* and "Specific heat capacity of ultra-thin atomic layer deposition nanobridges for microbolometers" published in the proceedings of Transducers 2015.[36,37]

Exciting research with 2D nanomaterials such as graphene and carbon nanotubes and ultra-scaled structures such as nanowires and quantum dots is highly relevant to the future of nano-electronics and nano-engineering.[80–86] However, there remains little characterization of ultra-thin metal/metal oxide thin film laminates, which are more easily implemented as electrical or thermal interconnects into current micro-fabrication techniques. Past micro-fabrication methods have made suspension of thin films on the order of 10's of nm's challenging. Since many thermal measurements require suspended structures to minimize thermal loss to underlying substrates there has been little characterization of ultra-thin films' thermal properties for use in nanodevices.[3,42,87] However, with the process described in section 3.1, suspended structures with

sub 20 nm thicknesses are easily fabricated.[34] This process is highly beneficial to the future characterization of many ultra-thin suspended films. Studies of these films often illuminate drastic physical property differences in the films from bulk. For example, electrical properties may vary substantially at the nanoscale due to an increased amount of electron scattering at film boundaries, grain boundaries and impurities or defects.[88] The knowledge of these differences will no doubt benefit the design and modeling of future nano-devices including, but not limited to microbolometer devices.

This portion of the thesis describes the measurement of the electrical resistivity, temperature coefficient of resistance, thermal conductivity and specific heat capacity of freestanding W and Al_2O_3, periodic W and Al_2O_3, and Ru and Al_2O_3. It also describes the measurement of ALD film morphology including grain size. This structural morphology is dominant in many electro-thermal transport mechanisms as will be seen in Chapter 6.

4.1 Fabrication of Sample Sets

A modified version of the fabrication process described in section 3.1.1 was used to fabricate test structures. Samples consist of arrays of cantilevers (nanobridges) varying in length from 20 – 190 μm and widths of 2, 4 and 6 μm (Figure 4.1b). ALD depositions of several thickness combinations of W, Ru and Al_2O_3 as well as periodicities were performed. One sample set consisted of 11.55, 15.40 and 20.40 nm W films surrounded by 3.20 nm Al_2O_3 layers on top and bottom. Another sample set consisted of periodic structures with the same total thickness to investigate the effect of periodicity in a W/Al_2O_3 configuration. The sample set consisted of chips containing a 20.40 nm W layer surrounded by 6.40 nm Al_2O_3 layers on top and bottom,

two 10.20 nm W layers spaced evenly by 4.20 nm Al_2O_3 layers, three 6.80 nm W layers spaced evenly by 3.20 nm Al_2O_3 layers and four 5.10 nm W layers spaced evenly by 2.56 nm Al_2O_3 layers. For the scope of this dissertation, the periodic samples will be referred to by "number of W layers", i.e. "4 W layers" refers to the sample containing four 5.10 nm W layers spaced evenly by 2.56 nm Al_2O_3 layers. Another sample set consisted of ~ 6.15 nm Al_2O_3 surrounding Ru layers of 2.71, 3.72, 5.69 and 7.97 nm of Ru, respectively. Thicknesses were verified by tunneling electron microscopy (TEM) (Figure 4.1a), X-Ray reflectometry (XRR) (Figure 4.2), and prior knowledge of deposition rates.[14,26] Aluminum contact pads were deposited after ALD patterning instead of before the polyimide layer for convenient electrical probing of the micro-bridges.

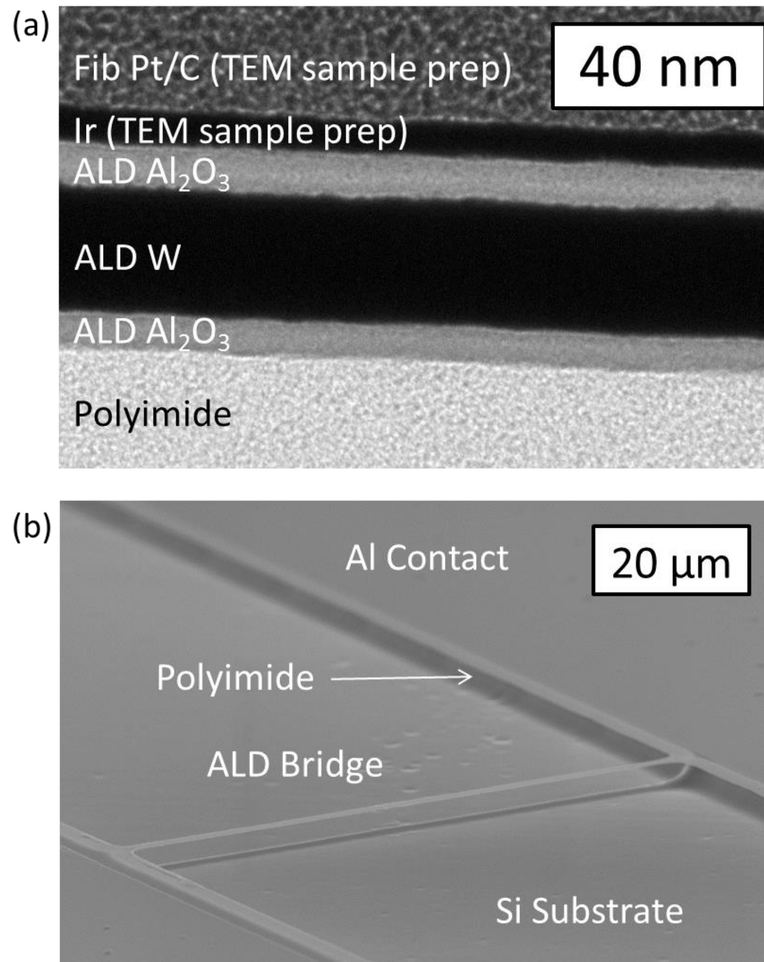

Figure 4.1: TEM cross-section and SEM image of test structures. a) TEM cross-section image of $Al_2O_3/W/Al_2O_3$ coating on polyimide with similar thickness to the test structures.[34] b) SEM image tilted by 75° of an 80 x 2 μm^2 suspended beam of $Al_2O_3/W/Al_2O_3$ with Al contact pads.

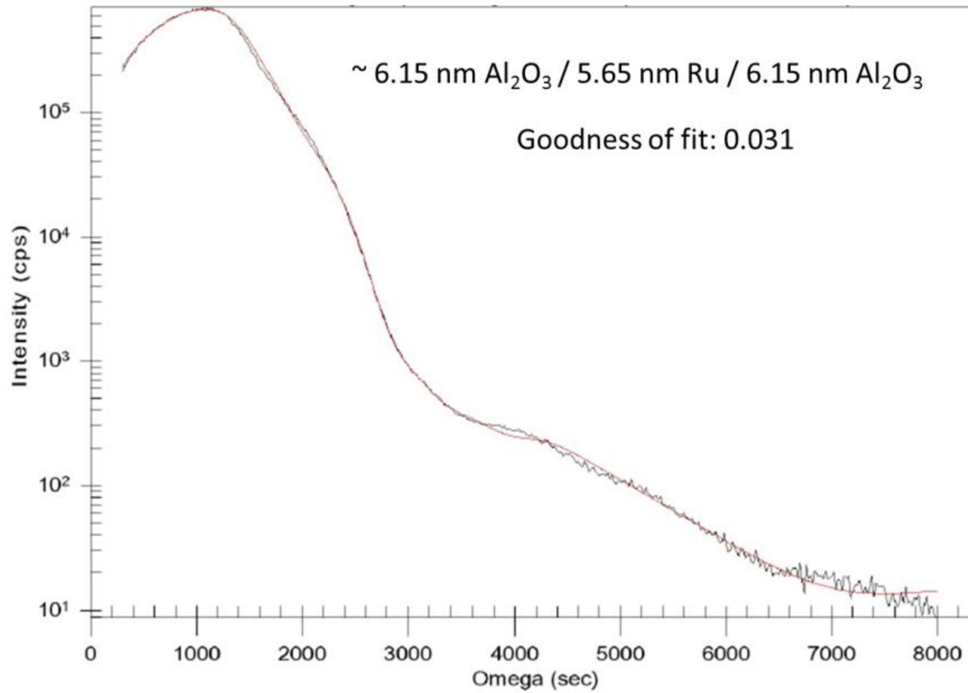

Figure 4.2: Example of an XRR scan for an Al_2O_3/Ru/Al_2O_3 film indicating ~ 6.15 nm Al_2O_3 / 5.69 nm Ru / 6.15 nm Al_2O_3 thicknesses.

4.2 Electro-thermal Measurement Methods

Several methods were used to measure the electro-thermal properties of the ALD samples described in section 4.1. For electrical resistivity of the W and Ru, the resistances of un-released nanobridges were measured and resistivity extracted through a geometric model. For the temperature coefficient of resistance of the W and Ru samples, the resistances of un-released nanobridges were monitored over temperature changes applied to the sample by a stage heater. For thermal conductivity, a dc-bias steady state heating method was used to extract the thermal conductivity of the W/Al_2O_3 and Ru/Al_2O_3 suspended nanobridges. For specific heat capacity a micro-pulse calorimetry method was used to extract the specific heat capacity of the W/Al_2O_3 and Ru/Al_2O_3 suspended nanobridges. The following sections provide a more in-depth description of each measurement method.

4.2.1 Electrical Resistivity Measurement

The electrical resistivities of the W and Ru samples are measured during the pre-release stage of fabrication. This method utilizes the electrical resistances of an array of beam lengths measured in a four-point-probe configuration pre-release to minimize Joule heating. Next, electrical resistivity is extracted through a fit of resistance versus beam length, following the relation:

$$R = \rho\, {}^{L}\!/_{A}\,, \tag{4.1}$$

where R is the resistance of the beam, L the length, A the beam cross-sectional area of the metal layer and ρ the electrical resistivity. Figure 4.3 demonstrates a typical resistivity extraction from a linear fit of beam resistance versus beam length.

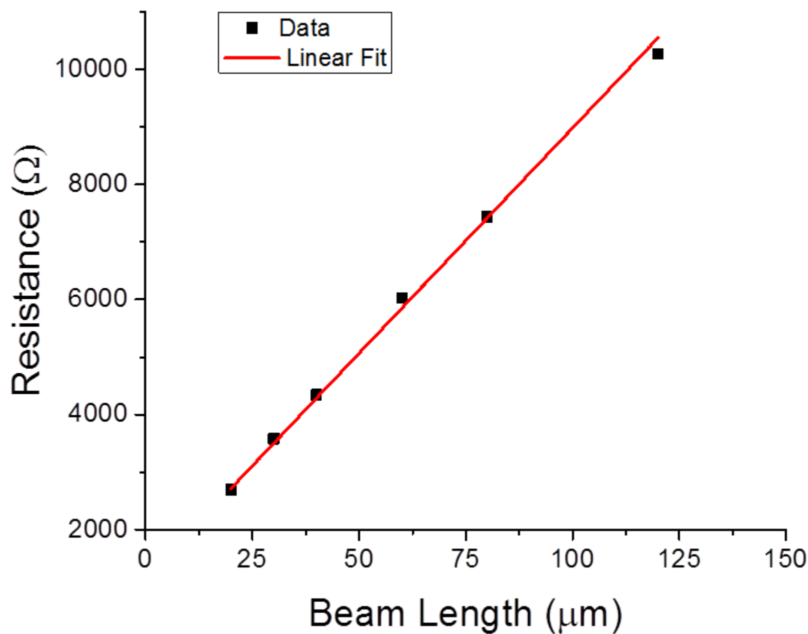

Figure 4.3: Resistance versus beam length for 15.40 nm W beams. The linear fit is used to extract resistivity through equation 4.1.

4.2.2 Temperature Coefficient of Resistance Measurement

The temperature coefficients of resistance (TCR) of the W and Ru nanobridges are measured pre-release to minimize joule-heating of the bridges. Samples are heated in atmosphere and nanobridge resistances monitored in a four-point-probe configuration. TCR is extracted by fitting the resistance versus temperature slope and follows the relation,

$$TCR = \frac{R - R_o}{(T - T_o) R_o}, \tag{4.2}$$

where, R_o is the room temperature resistance, T the temperature and T_o the room temperature. TCR's were measured to ~ 60 – 90 K above room temperature. Figure 4.4 demonstrates a typical TCR curve of normalized change in resistance versus temperature.

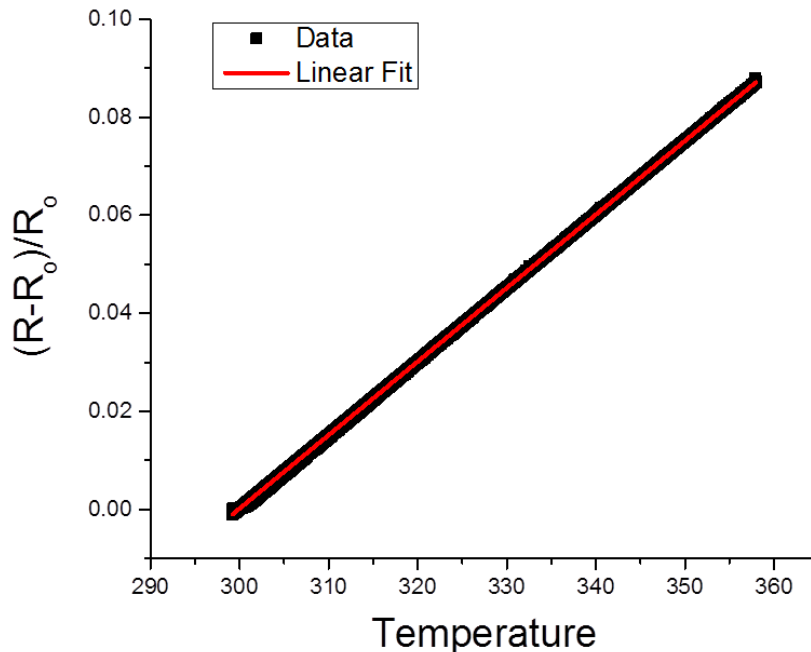

Figure 4.4: Normalized resistance change versus temperature for 7.97 nm Ru beam. The linear fit is used to extract TCR through equation 4.2.

4.2.3 Thermal Conductivity Extraction via Joule Heating Temperature Independent Electrical Resistivity Model

While there are various methods to measure thermal conductivity of structures and materials including the 3ω and frequency-dependent time-domain thermoreflectance, a simple DC based method has been used instead.[42,89] Two joule heating DC based models were used in the extraction of thermal conductivity of the W/Al_2O_3 and Ru/Al_2O_3 beams. The first model described below is based on the assumption that the electrical resistivity of the film is not temperature dependent and is relevant for materials with very small TCR values. By measuring the thermal conductances ($W\ K^{-1}$) of nanobridges with known physical dimensions, the thermal conductivity may be extracted by a model for joule-heated nanobridges. By considering the 1-dimensional steady-state heat equation,

$$T''(x) = \frac{-Q(x)}{\kappa A}, \tag{4.3}$$

where *A* is the total cross-sectional area of the bridge and the source *Q(x)* may be defined as,

$$Q(x) = j^2 \rho, \tag{4.4}$$

where j is current density (Amperes m^{-2}) and ρ is the temperature *independent* electrical resistivity. By applying the following definitions of j and ρ, *Q(x)* may be redefined:

$$j = \frac{I}{A}, \tag{4.5}$$

$$\rho = R\frac{A}{l}, \tag{4.6}$$

$$P = I^2 R, \tag{4.7}$$

$$Q(x) = \frac{P}{l}, \tag{4.8}$$

where I is the current applied to the bridge, R is the resistance, l the length of the bridge, and P the total power applied. The solution to equation 4.3 given the above joule heating conditions and boundary conditions $T(0)=0$ and $T(l)=0$ is given as,

$$T(x) = \frac{P}{2\kappa A}\left(x - \frac{x^2}{l}\right). \tag{4.9}$$

To measure thermal conductance, the temperature of the bridge must be measured as power is applied by joule heating. The temperature may be calculated by using a known TCR value and by measuring the change in resistance of the bridge as the power applied. The average temperature of the bridge is given as,

$$\Delta T_{avg} = \frac{R_{avg} - R_o}{TCR \cdot R_o}, \tag{4.10}$$

where R_{avg} is the measured resistance and R_o the initial resistance. By plotting power applied versus the average change in temperature of the beam (Figure 4.5), the thermal conductance (W K^{-1}) may be extracted by a linear fit as the inverse slope (assuming a temperature independent thermal conductivity). To define the thermal conductance in terms of the thermal conductivity, the average of equation 4.9 must be calculated since the temperature is calculated by measuring the average resistance of the bridge. The average change in temperature of the beam is given as,

$$\overline{T(x)} = \frac{Pl}{12\kappa A}, \tag{4.11}$$

where thermal conductance is defined as,

$$G = \frac{P}{\overline{T(x)}} = 12\kappa\frac{A}{l}. \tag{4.12}$$

A factor of 12 is introduced to the traditional definition of thermal conductance by the conditions of joule heating. Equation 4.12 may be utilized to fit thermal conduction versus nanobridge length demonstrated by Figure 4.6.

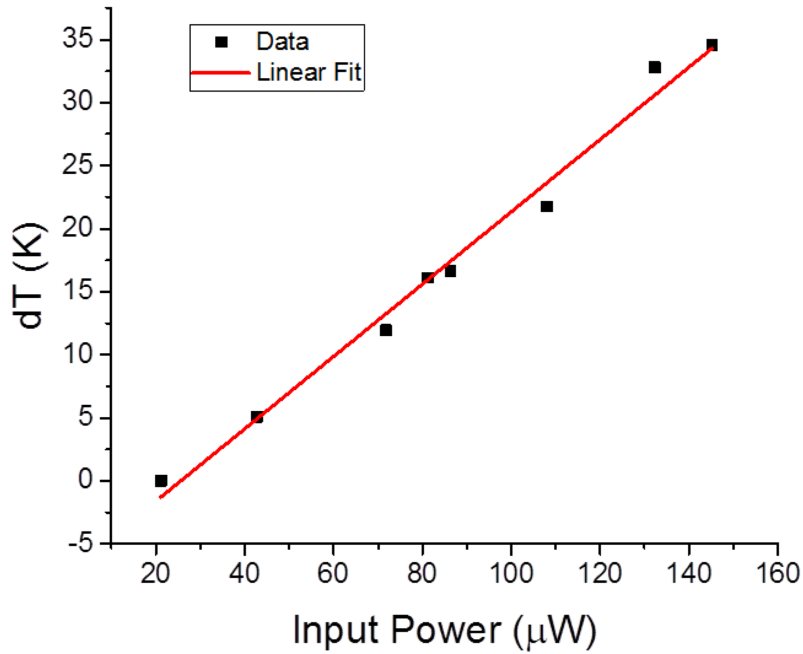

Figure 4.5: Relation of change in temperature versus joule heating input power for a 6.20 nm Al_2O_3/20.40 W/6.20 Al_2O_3 nanobridge. Thermal conductance G_{th} is extracted by a linear fit as the inverse of the slope.

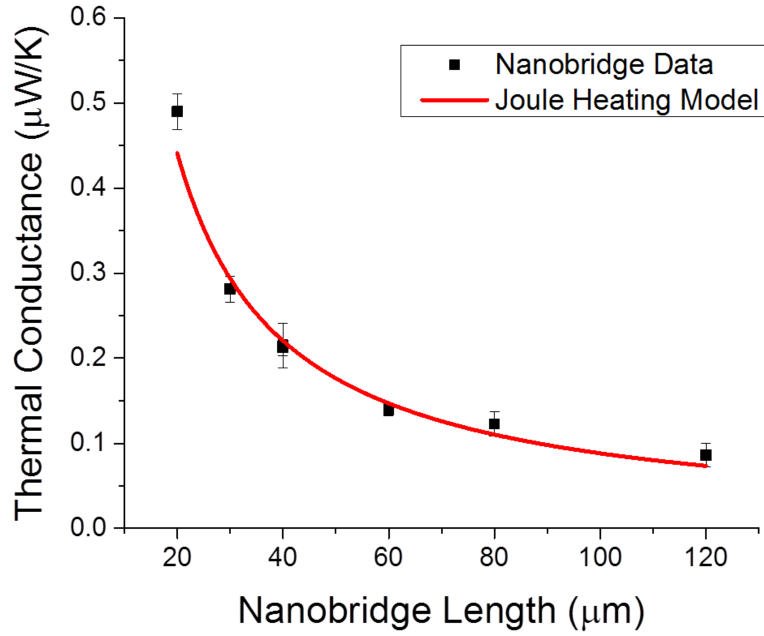

Figure 4.6. Relation of thermal conductance to length for a 9.80 nm Al_2O_3/20.40 W/9.80 Al_2O_3 cross-section nanobridge. Thermal conductivity is extracted by fitting the derived joule-heating model (Equation 4.12) to the data.

4.2.4 Thermal Conductivity Extraction via Joule Heating Temperature Dependent Electrical Resistivity Model

For films with larger TCR it is important to consider the effect of temperature dependence on the resistance of a suspended structure upon joule heating. As the structure heats up, its resistance changes, inducing a non-linear change in the amount of power dissipated in the structure. Thus, the thermal conductance of the structure is varied. To account for this, the temperature dependent electrical resistance must be included in the derivation of a joule heating resistance model. The one-dimensional heat diffusion equation with a temperature sensitive electrical resistivity and boundary conditions is given as,

$$\kappa \frac{d^2T}{dx^2} + \frac{I^2 R_o[1+TCR(T-T_o)]}{wtL} = 0 \tag{4.13a}$$

$$T\left(x = \pm\frac{L}{2}\right) = T_o \tag{4.13b}$$

where κ is thermal conductivity, I is electrical current, R_o is the initial resistance of the beam, TCR is the temperature coefficient of resistance, and w, t, L are the width, thickness and length of the beam respectively. Substituting variable θ into equation 4.13a, where $\theta = 1 + TCR(T - T_o)$ results in the following new equation and boundary conditions in the convenient form,

$$\frac{d^2\theta}{dx^2} + m^2\theta = 0\ , \tag{4.14a}$$

$$\theta\left(x = \pm\frac{L}{2}\right) = 1 \tag{4.14b}$$

where,

$$m^2 = I^2 R_o TCR/(wtL\kappa). \tag{4.14c}$$

The solution to the new equation is,

$$\theta(x) = \cos(mx)\,/\cos(\tfrac{mL}{2})\ . \tag{4.15}$$

Resubstituting this solution allows T to be solved for and subsequently the average of T since the average resistance is what is experimentally measured. The temperature is given as,

$$T(x) = \frac{\theta(x)-1}{TCR} + T_o. \tag{4.16}$$

Integrating from $-l/2$ to $l/2$, the average temperature and resistance are given as,

$$\bar{T} = T_o - \frac{1}{TCR}[1 - (2/mL)\tan(mL/2)], \tag{4.17}$$

$$R = R_o[(2/mL)\tan(mL/2)]. \quad (4.18)$$

From here, one may plot R versus I^2 and use equation 4.18 to extract κ. See Figure 4.7 for an example of data and κ extraction fit by equation 4.18. There is a very subtle non-linearity as a result of the temperature dependent resistivity term. For bulk-like film with much larger TCR, the non-linearity effect will be enhanced.

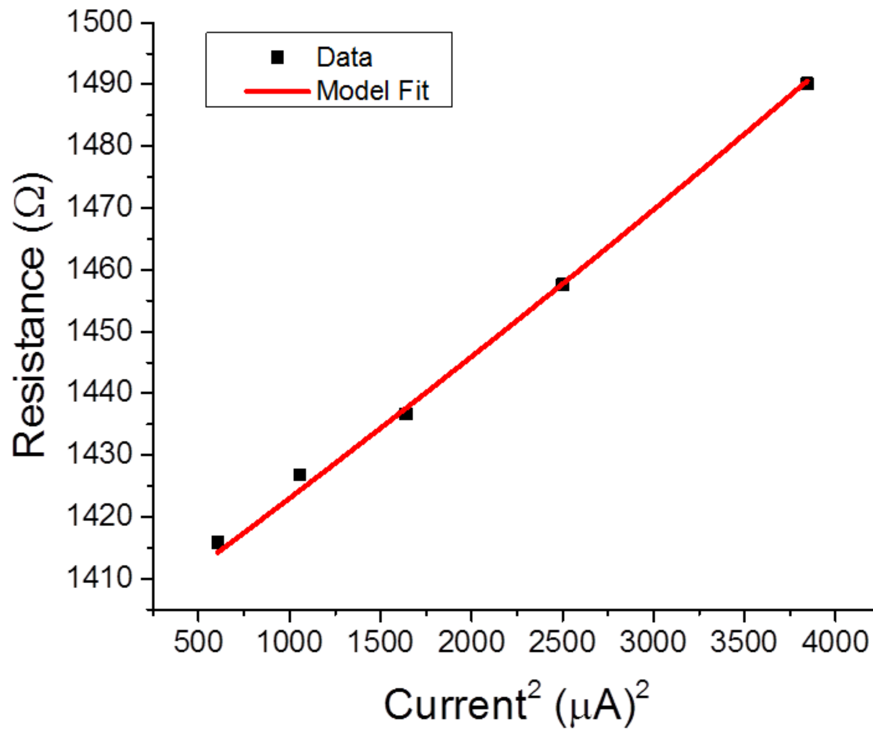

Figure 4.7: Resistance versus applied current squared for 6.70 nm Al_2O_3/7.97 nm Ru/6.70 nm Al_2O_3 nanobridge. Thermal conductivity is extracted by fitting equation 4.18 (red line) to the data.

4.2.5 Specific Heat Capacity Extraction via Micropulse Calorimetry

A structure's rate of heating is often described by its thermal time constant. By measuring the thermal time constant, a relation between the volumetric heat capacity and thermal conductivity

may be achieved. Thus, by knowing the thermal conductivity of the structure, the volumetric and specific heat capacity may be extracted. The test structures described in section 4.1 were measured using micropulse calorimetry. By applying a pulsed voltage (< 1 μs) across the bridge, a transient current response may be monitored which is several orders of magnitude slower than the voltage pulse. This effect is a result of the temperature sensitive nanobridge resistance responding to joule heating of the metal and surrounding Al_2O_3 layers. The magnitude of this resistance change is governed by the temperature coefficient of resistance (TCR). By fitting an exponential decay function to the post voltage pulse current response, τ may be extracted (Figure 4.8). The measured τ corresponds directly to how quickly the nanobridge is heating up to its steady state temperature based on the total heat capacity and effective material properties of the nanolaminate.

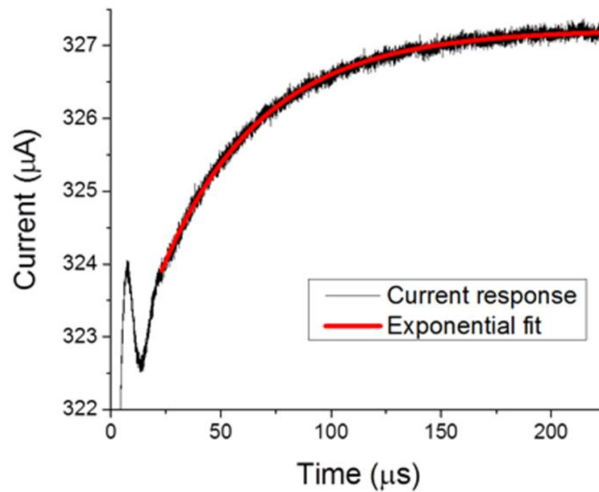

Figure 4.8: Raw current response data post voltage pulse at time zero for 6.50 nm Al_2O_3/20.40 nm W/6.50 Al_2O_3. The red line is an exponential decay fit from which τ is extracted.

To extract the specific heat capacity, a model for τ was derived from the time-dependent heat equation for the case of joule-heated beams with a temperature independent electrical resistivity. The problem and solution are given as,

$$C\frac{\partial \Delta T(x,t)}{\partial t} = \kappa A l \frac{\partial^2 \Delta T(x,t)}{\partial x^2} + P, \tag{4.19a}$$

$$\Delta T(x,t) = \sum_{n\ odd} \frac{4Pl}{\kappa A n^3 \pi^3}\left(1 - e^{-\frac{\pi^2 \kappa A n^2}{Cl}t}\right)\sin\left(\frac{n\pi x}{l}\right), \tag{4.19b}$$

where T is the temperature, P is the power applied, C is the heat capacity, l is the length, κ is the thermal conductivity, and A is the cross-sectional area. The measured transient current response is based on the average resistance of the beam, thus the average change in temperature of the beam should be used instead of the absolute change in temperature. Taking the average of equation 4.19b results in,

$$\overline{\Delta T(t)} = \frac{Pl}{12\kappa A} - \frac{8Pl}{\kappa A \pi^4}\sum_{n\ odd}\frac{1}{n^4} e^{-\frac{\kappa A n^2 \pi^2}{Cl}t}, \tag{4.20}$$

where the identity,

$$\sum_{n\ odd}\frac{1}{n^4} = \frac{\pi^2}{96}, \tag{4.21}$$

was used in the derivation. At t = 0, $\overline{\Delta T(0)} = 0$ and in the limit that t goes to infinity, $\overline{\Delta T(\infty)}$ $= {Pl}/{12\kappa A}$, which is the steady state solution for a joule heated beam. In this case, the solution contains an infinite number of different time constants. However, as a reasonable approximation,

since further terms diminish as n^{-4}, the first term of the series in equation 4.20 is utilized to extract a single τ from the exponential term,

$$\tau = {Cl}/{\kappa A\pi^2} = {c\rho l^2}/{\kappa\pi^2}, \tag{4.22}$$

given, $C = c\rho V$, where c is the specific heat capacity, ρ is the density and V the volume. Specific heat capacity is extracted in a fit of τ versus cantilever length using measured effective κ values for the given ALD nanolaminate and calculated effective density based on the thickness weighted densities of the associated ALD materials.[14,37] An example of a c extraction from a fit of equation 4.22 is demonstrated in Figure 4.9.

The transient heat equation with temperature independent electrical resistivity was used over the temperature dependent electrical resistivity transient heat equation because the latter is cumbersome to solve and requires complicated numerical modeling. Previous work has shown less than 2% variation between temperature dependent and temperature independent transient heat equation models in extracted specific heat values for thick Pt wires with bulk-like TCR values.[90] The variation will only be reduced further for the nanofilms with reduced TCR values studied here.

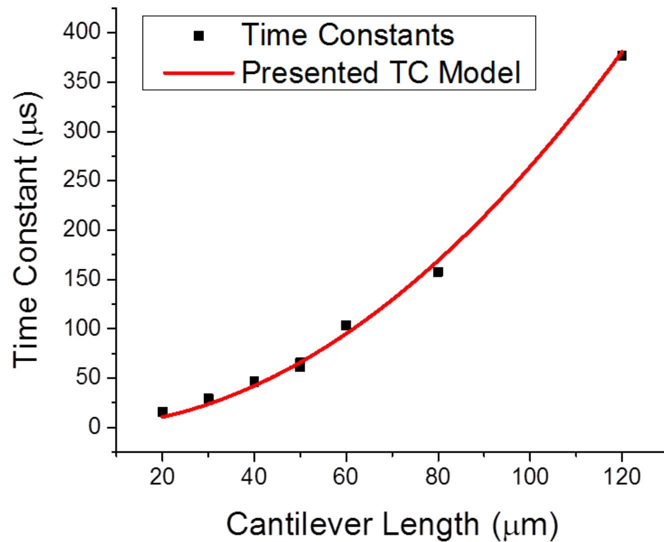

Figure 4.9: Time constant data with respect to nanobridge length plotted as black squares for 6.50 nm Al_2O_3/20.40 nm W/6.50 Al_2O_3. The data is fitted with the presented model (equation 4.22) and specific heat capacity extracted.

4.3 Thermal Loss Calculations and Adjustments

When attempting to measure thermal and electrical properties of nanoscale films, the heat loss in various forms must be considered. For the measurement of electrical resistivity, and temperature coefficient the effect of joule heating on the measurement was considered negligible due to low test currents, the attachment of the structures to the underlying substrate and the effects of convective cooling during the measurement at atmospheric pressures. However, the previously described methods for measuring thermal conductivity and specific heat capacity are done under vacuum at ~ 30 mTorr for the W/Al_2O_3 samples and ~ 5 mTorr for the Ru/Al_2O_3 samples. Though thermal convection is negligible at these pressures, thermal losses such as conduction to the air and radiation must be considered, especially for the 30 mTorr pressures.[91,92] Below 10 mTorr conduction to air is negligible compared to the magnitude of the beam thermal conductance.[92] Thermal conduction to air may be defined by the following relation,

$$G_{gas} = G_s + G_w = \frac{S}{\frac{1}{h_{s,hi}}+\frac{1}{h_{s,lo}}} + \frac{S}{\frac{1}{h_{w,hi}}+\frac{1}{h_{w,lo}}}, \tag{4.23}$$

where G_s is the total conduction to the substrate from the bottom of the bridge, G_w is the total conduction to the substrate from the top of the bridge, S is the surface area of the nanobridge, $h_{s,hi}$ is the convection coefficient at ambient pressure between the bottom of the bridge and the substrate, $h_{s,lo}$ is the convection coefficient at low pressure between the bottom of the bridge, $h_{w,hi}$ is the convection coefficient at ambient pressure between the bridge and the window of the vacuum probe station, and $h_{w,lo}$ is the convection coefficient at low pressure between the top of the bridge and the window of the vacuum probe station. The heat convection coefficients may be defined as,

$$h = \frac{\kappa(P,d)}{d}, \tag{4.24}$$

where κ is the gas conductivity of air and is a function of pressure P, and distance d, to a theoretical parallel plate (substrate or viewing window). The thermal conductivity may be calculated by the following relation,

$$\kappa = \frac{\kappa_O}{1+\frac{C}{PP}}, \tag{4.25}$$ [93]

where C is a constant defined as 7.6 x 10^{-5} N m^{-1} K^{-1} and pressure parameter PP, is defined as,

$$PP = \frac{P \cdot d}{T}, \tag{4.26}$$ [93]

where T is the absolute temperature. The conduction to air calculations were verified by measuring the thermal conductance of a beam at both 30 mTorr and 500 μTorr. The thermal

conductance at 30 mTorr was 1.4% larger than the thermal conductance at 500 μTorr, only a 0.1 % difference from the calculations presented above.

Additionally, considering the large surface area to volume ratio for these ultra-thin nanobridges, radiation losses will become non-negligible as the bridges are heated. Radiation conduction may be defined as,

$$G_{rad} = 2 \cdot \sigma \cdot \varepsilon \cdot S \cdot T_{avg}^{3}, \tag{4.27}$$

where σ is the Stefan Boltzmann constant, and ε the emissivity, which is assumed to be 0.9 and background radiation is at ambient. However, even at the maximum temperature rise, the thermal conductance due to radiation is ~ 2 orders of magnitude smaller than the measured thermal conductance of the nanobridges.

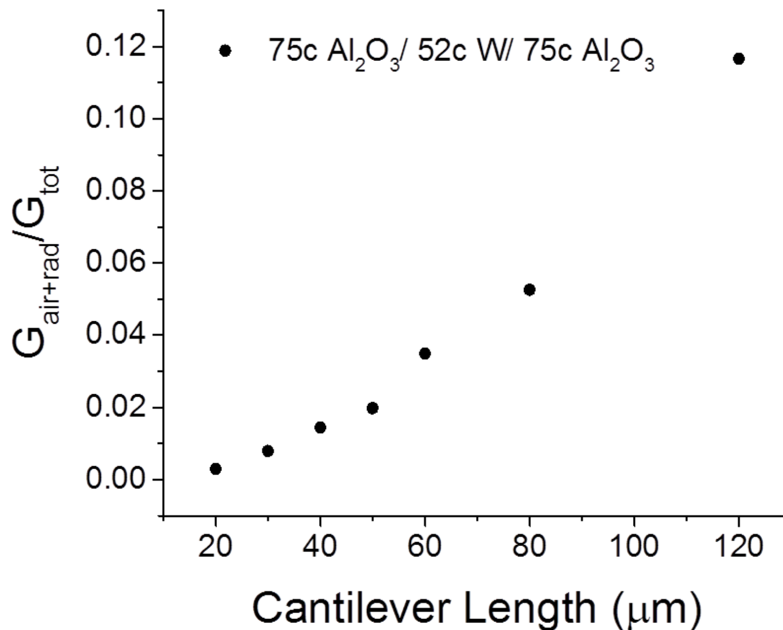

Figure 4.10: The percentage of conduction attributed to air and radiation from the total measured thermal conductance of individual nanobridges.

By combining the relevant conduction mechanisms of the nanobridge system under investigation, the total conduction may be defined as,

$$G_{tot} = G_{gas} + G_{rad} + G_{conv} + G_{beam}, \quad (4.28)$$

where G_{conv} is still negligible. An example of the percentage of bridge conduction attributed to conduction to air and radiation conduction for nanobridges with a 9.80 nm Al_2O_3/20.40 nm W/9.80 nm Al_2O_3 cross-section is shown in Figure 4.10.

For each sample, the total measured thermal conductance may be adjusted through the calculations described above. Figure 4.11 shows a plot of adjusted thermal conductance values and total thermal conductance values versus nanobridge length. Each data set was fit using the joule-heating model presented in section 4.2.3 or section 4.2.4. For example, for a 9.80 nm Al_2O_3/20.40 nm W/9.80 nm Al_2O_3 cross-sectional nanobridge, the relative change in thermal conductivity was reduced by 1.8%.

A similar approach was utilized for the measurement of specific heat capacity. The measured thermal time constants were adjusted to reflect heat losses during the measurement. Since $\tau \sim C/G$ where C is heat capacity and G is thermal conductance, the thermal conductance may be adjusted based on heat losses during the transient heating of the beams.

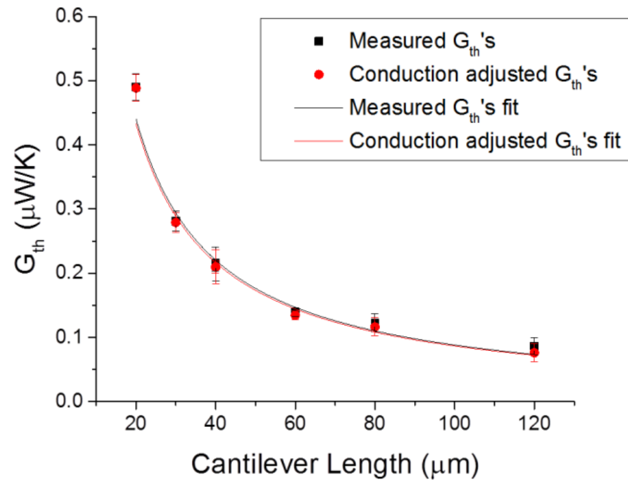

Figure 4.11: Adjusted thermal conductance values and total measured thermal conductance values with associated fits using the joule heating model from section 4.2.3.

4.4 Verification of Measurement Methods with Evaporated Aluminum

To verify the accuracy of the measurements described in section 4.2.3 and 4.2.4 a sample consisting of thin film aluminum was fabricated using a technique very similar to the one described in section 4.1. An aluminum film was evaporated on polyimide at ~ 10 μTorr at 1 nm/s to a thickness of 100 nm. A lithographic photoresist pattern was applied and instead of using RIE to etch the Al film, a wet etch using Transene A aluminum etchant for ~ 4 min was used. The resultant nanostructures were released in an O_2 plasma.

The electrical resistivity was 34.2 nΩ*m compared to 28.2 nΩ*m bulk value and the TCR was 0.395 %/K compared to 0.429 %/K for bulk.[94] Both values are within expected range from scaling effects for a 100 nm film.

Thermal conductance measurements of released bridges were carried out as described in sections 4.2.3 and 4.2.4. The wet etch resulted in varying widths of bridges and thus thermal conductivity was extracted using the method from section 4.2.3 through a plot of Thermal

Conductance/Bridge Width vs. Bridge Length where bridge widths were measured using an SEM. Figure 4.12 shows the Al bridge data and the joule heating model fit. The extracted value for the 100 nm Al film was 209.8 ± 4.7 W/mK. Volkov et al. measured 50, 74 and 110 nm films where the expected thermal conductivity for a 100 nm film based off their measurements was ~ 214 W/mK.[95] Slight differences in thermal conductivity values are expected due to small variances in the film preparation method. However, the method presented in this thesis was shown to extract a thermal conductivity value of 100 nm aluminum within 1.5% of work by Volkov et al.. Using the thermal conductivity extraction method from section 4.2.4 resulted in almost the same value for thermal conductivity within 1%.

Additionally, the specific heat capacity was extracted. Micropulse calorimetry was conducted on the 100 nm Al sample as described in section 4.2.5. XRR scans indicated an aluminum density identical to bulk. The extracted value for the specific heat capacity was ~ 0.90 J/gK. The transient current response for a 100 nm Al nanobridge is shown in Figure 4.13. The bulk value is also 0.90 J/gK and agrees with results from Volkov et al.[95]

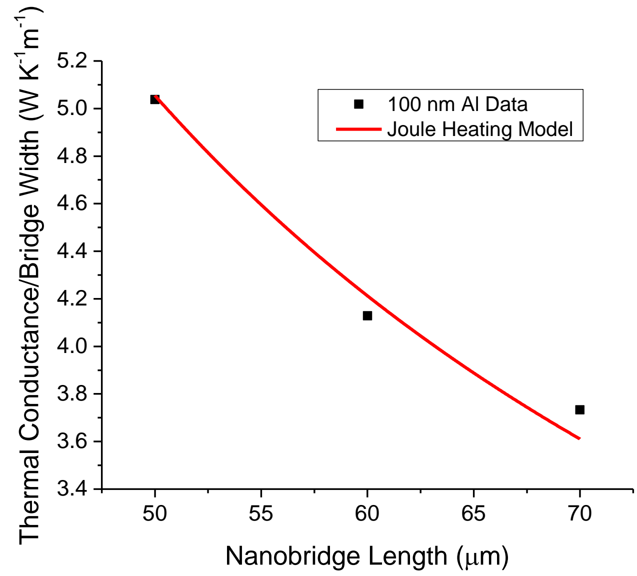

Figure 4.12: Relation of thermal conductance/bridge width to length for 100 nm Al film. Thermal conductivity is extracted by fitting the derived joule-heating model (section 4.2.3) to the data.

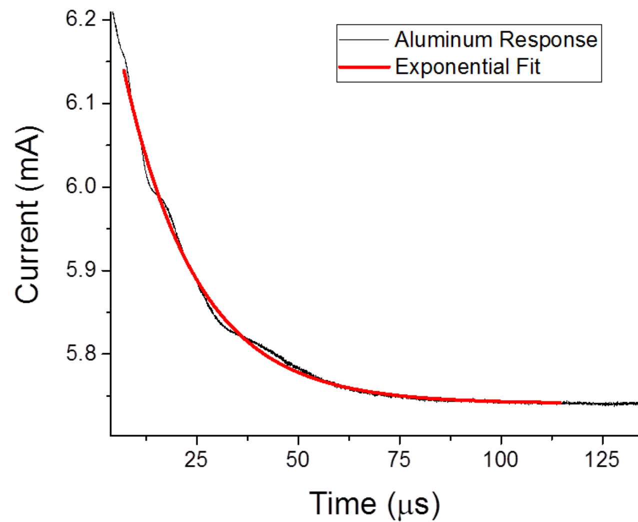

Figure 4.13: Transient current response of 100 nm Al nanobridge. Specific heat capacity is extracted by calculating *c* from equation 4.22 with known density and thermal conductivity.

4.5 Grain Size Measurement

Grain size measurement has been included in this chapter because it plays one of the dominant roles in electro-thermal transport for ultra-thin films. As will be discussed in Chapter 6, electron and phonon scattering at grain boundaries can play a larger role than traditional electron-phonon interactions in ultra-thin films. Grain studies of both the W and Ru were carried out using Grazing Incidence X-ray Diffraction (GIXRD). The Scherrer equation was used to estimate the crystal grain sizes in the ALD metal films from the amount of peak broadening in the X-ray diffraction peaks. The Sherrer equation for crystal grain size, *S*, is given by,

$$S = \frac{0.9\lambda}{Bcos(\theta)}, \tag{4.29}$$

where λ is the X-ray radiation used (1.541 Å), B is the full width at half max of the 2θ peak in radians, and θ is half of the omega angle at which the peak max occurs.

For example, Figure 4.14 shows XRD scans with peak fits for a 20 nm ALD W film. GIXRD spectra indicate the presence of β-W in the ALD films, and it is likely that a mixture of both β-W and α-W exist. It is difficult, however, to accurately separate the four GIXRD peaks necessary for using the Scherrer equation, but a lower limit on grain size can be obtained by fitting the entire broad spectrum, from an Omega of 30 to 50, as one single peak (see Figure 4.14a). If instead four peaks (three β-W peaks and one α-W peak) are used to fit the GIXRD spectrum from 30 to 50 Omega, a larger estimated grain size is obtained (Figure 4.14b). An average of these methods can produce an average grain size for the film. For films with more prominent crystal peaks, an average of single peak fits may be used to extract the approximate grain size in the film.

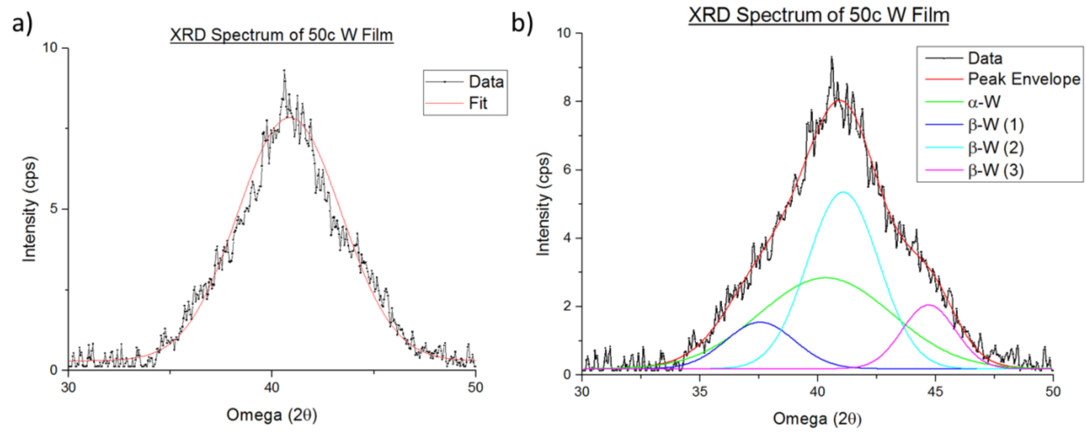

Figure 4.14: XRD data. a) Single peak fit on a 20 nm W ALD film. b) Multiple peak fitting on 20.40 nm W ALD film.

4.6 Experimental Circuit Diagrams for Electro-thermal Characterization

The experimental circuit diagram for resistivity, TCR and thermal conductivity measurement is outlined by Figure 4.15. The experimental circuit diagram for the time constant and specific heat measurement is outlined by Figure 4.16.

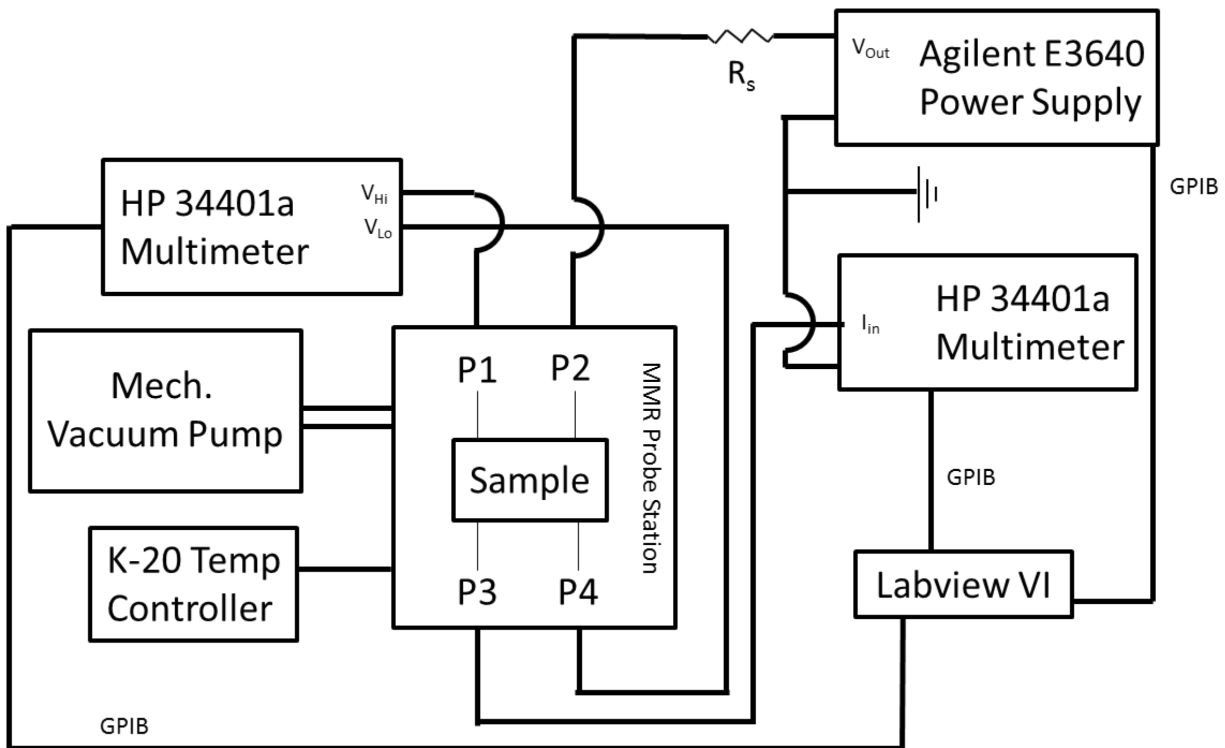

Figure 4.15: Circuit diagram for resistivity, TCR and thermal conductivity measurement.

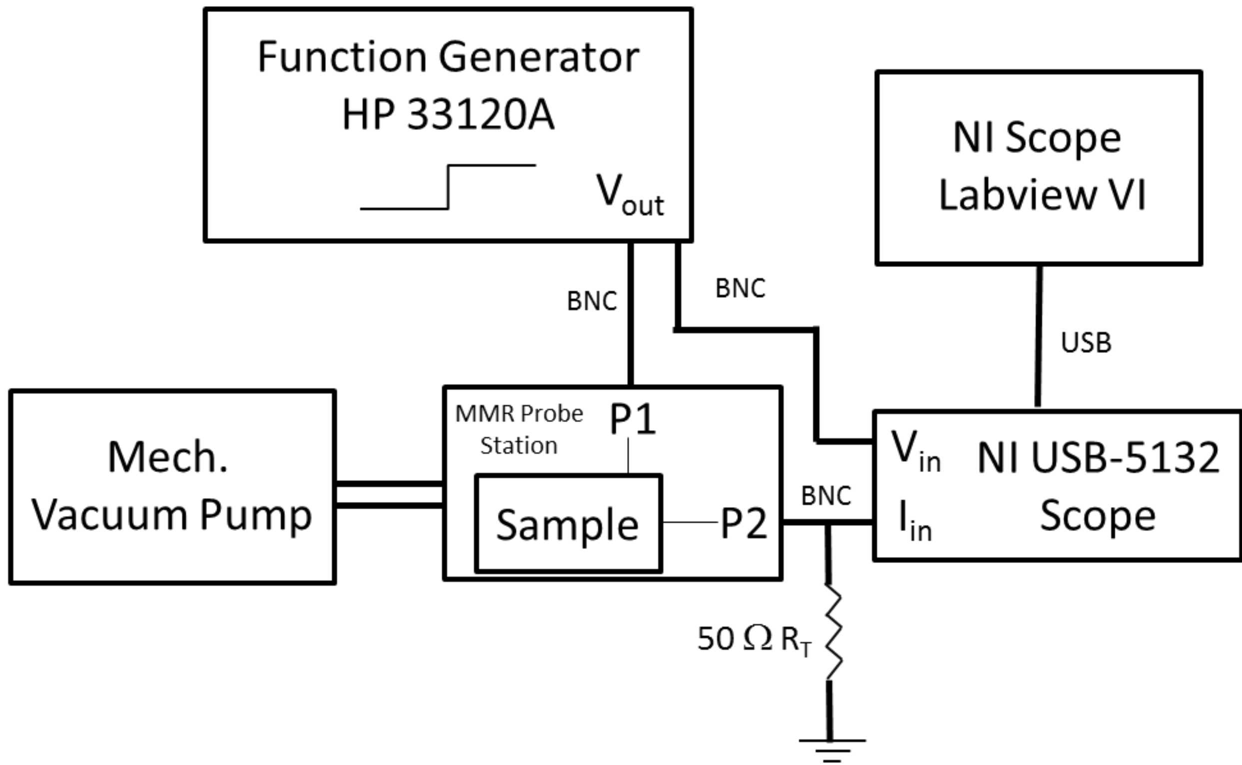

Figure 4.16: Circuit diagram for specific heat capacity measurement.

4.7 Uncertainty Analysis

Uncertainty analysis is important to consider when presenting measured values. This chapter has presented several measurement methods, which involve the instrumental measurement of data that is then used in further calculation or graphing/fitting procedures. A brief description of the universal methods used will be presented in this section.

Uncertainty analysis has been conducted using methods from Holman.[96] The uncertainty of a value Δv, may be defined as,

$$\Delta v^2 = \Delta_{fit}^2 + \Delta_{exp}^2, \tag{4.30}$$

where Δ_{fit} is the uncertainty from the fitting procedure and Δ_{exp} is associated with uncertainty of the measured parameters used in the fitting procedure. For any calculated values based off measurement values, it should be assumed that the "law of propagation of error" was used. Here, Δ_{exp} is related to the measurement sensitivity defined as,

$$\Omega_r = r\frac{\partial f}{\partial r}, \tag{4.31}$$

where *f* is the fitting function and *r* can be any of the independent variables necessary to evaluate the fitting function. The Δ_{exp} may be expressed as,

$$\Delta_{exp} = \frac{1}{\Omega_v}\left(\sum_r(\Omega_r \Delta r)^2\right)^{1/2}, \tag{4.32}$$

where Δr is the uncertainty of the independent variables, and Ω_r is the measurement sensitivity with respect to *v*. The Δ_{fit} was calculated using Origin Pro software outfitted with linear and non-linear fitting packages. To calculate Δ_{fit}, the software outputted standard error of the fit was multiplied by $\sqrt{n}$ where n is the number of data points in the fit. Then, Δv may be calculated from equation 4.30.

Chapter 5

Electro-thermal Property Results of ALD W/Al_2O_3 and Ru/Al_2O_3 and Periodic W/Al_2O_3

This chapter will discuss the various measured electro-thermal properties of ALD films. Chapter 6 will include a detailed interpretation of these results. Chapter 7 will include a more detailed discussion of the application of these nano-structures to a DRS-style microbolometer pixel.

The film thicknesses of both W and Al_2O_3 were varied between ~ 5 – 20 nm and ~ 3 – 13 nm, the thicknesses of Ru between ~ 2 – 8 nm and fabricated using the ALD on polyimide process described in section 3.1.[34] As described in section 2.1.5, recent work with ALD nanolaminates as active materials have involved the fabrication of ALD Pt microbolometers and an array of various N/MEMS devices involving ALD W/Al_2O_3 and ALD Ru/Al_2O_3.[18,19,21,22,24,34,42,55] Thermal barrier research has involved the characterization of through-plane interface thermal resistance in ALD W/Al_2O_3, however, specific studies of the electrical

and thermal properties of free-standing ALD W/Al_2O_3 and Ru/Al_2O_3 nanolaminates remains absent in the literature.[97] While nanolaminates with extended periodicity are common approaches to the optimization of out-of-plane electrical and thermal conduction in thermoelectric materials, they may also benefit nano-devices which conduct electricity and heat in-plane.[97] Periodic structures in application to microbolomeer performance will be discussed in Chapter 7. For the following sections, it should be assumed that reference to Al_2O_3, W, or Ru is to Al_2O_3, W or Ru generated by atomic layer deposition as described in section 2.1.

5.1 Summary of ALD W, Ru, Al_2O_3 Sample Sets

A summary of the studied sample sets is given by Table 5.1. Thicknesses and densities are taken from XRR measurements described in section 3.3. The Al_2O_3 films for all samples are positioned on top and bottom of the metal layers and are equal in thickness. The Al_2O_3 has a density of 3×10^6 g/cm^3.

Table 5.1: Summary of electro-thermal measurements sample set.

Sample	Top Al_2O_3 Thickness (nm)	Metal Thickness (nm)	Bottom Al_2O_3 Thickness (nm)	Metal Density (g/cm^3)
1. Varied W, constant Al_2O_3	3.2	11.6	3.2	16.7
		15.4		
		20.4		
2. Varied W, constant Al_2O_3	6.4	11.6	6.4	16.7
		15.4		
		20.4		
3. Varied Al_2O_3, constant W	9.6	20.4	9.6	16.7
	6.4		6.4	
	3.2		3.2	
4. *Periodic W/Al_2O_3	6.4*	20.4*	6.4*	16.7
5. Varied Ru, constant Al_2O_3	6.7	2.7	6.7	9.5
		3.7		
		5.7		
		8.0		

*Periodic structure maintains constant total thickness with W and Al_2O_3 layers split as denoted by Figure 5.2.

5.2 Electrical Resistivity of ALD W and ALD Ru

Both the resistivity of single ALD W and Ru films and periodic ALD W/Al_2O_3 films have been measured. Figure 5.1a demonstrates the room temperature electrical resistivity of W and Ru at a variety of thicknesses. The electrical resistivity of ALD W is significantly larger than bulk W, which has a resistivity of 5.8 μΩ*cm and of the ALD Ru films. Even at almost a tenth of the thickness at ~ 3 nm, Ru has a lower resistivity than that of a ~ 20 nm W film. Both films show an expected thickness dependent scaling wherein thinner films exhibit larger resistivities. Chapter 6 will discuss these results in more detail. Figure 5.2 demonstrates the cross-section of the periodic W/Al_2O_3 structures constant total thickness and Figure 5.1b demonstrates the electrical resistivity of the 4 periodic W/Al_2O_3 samples. The resistivity remains relatively constant until the 4 layer W sample where it increases slightly relative to the resistivity increase for single layer W films.

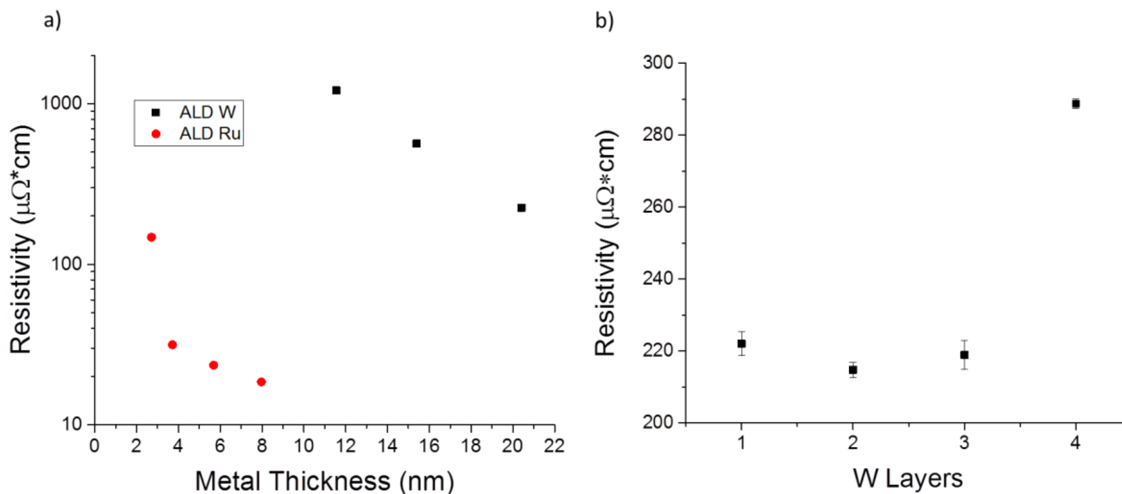

Figure 5.1: Electrical resistivity of single W and Ru ALD films and periodic ALD W films at room temperature. a) Thickness dependence of electrical resistivity of W and Ru films are plotted as black squares and red circles, respectively. b) Periodic layer dependence of electrical resistivity of W/ Al_2O_3 periodic layer stack with constant total thickness.

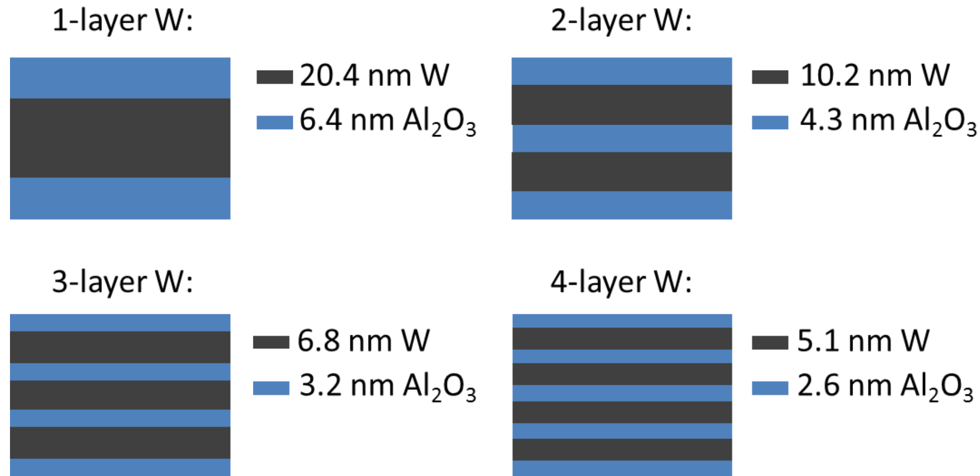

Figure 5.2: Representative graphic of periodic W/Al_2O_3 structures from 1 – 4 layers with constant total thickness.

5.3 Temperature Coefficient of Resistance of ALD W and ALD Ru

The TCR of single W and Ru films as well as periodic W/Al_2O_3 films were measured. Figure 5.3a demonstrates the room temperature TCR of single layer W and Ru. The TCR for ALD W is negative and increases in magnitude with thinner films, contrary to the expected positive TCR associated with metal films. By comparison, bulk W and Ru have positive TCRs of ~ 0.40 – 0.45 %/K at room temperature. Figure 5.3b demonstrates the TCR of the 4 periodic W/Al_2O_3 samples. The TCR for the periodic structures is also negative and increases in magnitude with increasing periodicity or an increased number of thinner W layers which equate to the same total thickness (Figure 5.2). ALD Ru films exhibit an expected positive metallic TCR effect that decreases with decreasing film thickness as demonstrated in Figure 5.3a. The Ru TCR is roughly an order of magnitude larger than the W.

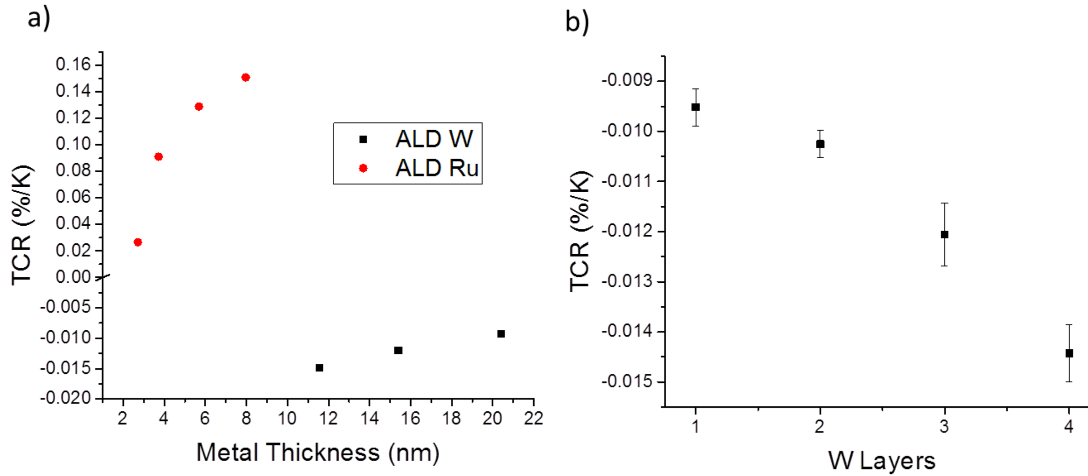

Figure 5.3: TCR of W, Ru and periodic W/Al_2O_3 structures. a) TCR of W plotted as black squares and Ru plotted as red circles with respect to metal thickness. b) TCR of periodic W/Al_2O_3 plotted as black squares with respect to number of W layers denoted in Figure 5.2.

5.4 Thermal Conductivity of ALD W/Al_2O_3, ALD Ru/Al_2O_3 and Periodic ALD W/Al_2O_3

The thermal conductivities of single film Al_2O_3/W/Al_2O_3 and periodic W/Al_2O_3 films were measured utilizing the method described in section 4.2.3. The method is justified by the extremely small magnitude TCR of W (|TCR| < 0.02 %/K). The thermal conductivies of single film Al_2O_3/Ru/Al_2O_3 were measured using the method described in section 4.2.4 due to the larger TCR of ALD Ru. For the single film W trilayers ~ 3.2 nm Al_2O_3 was layered on top and bottom of the W film. For the single film Ru trilayers ~ 6.7 nm Al_2O_3 was layerd on top and bottom of the Ru film. Thus, the effective thermal conductivity of the trilayer stack was measured as the Al_2O_3 will contribute some degree of thermal conduction in the form of phonon conduction. Further discussion of parellel conduction is presented in Chapter 6. Figure 5.4 demonstrates the effective thermal conductivity of the Al_2O_3/W/Al_2O_3 and Al_2O_3/Ru/Al_2O_3 laminates. For both the W and Ru samples, descreasing the metal thickness decreases the effective thermal conductivity of the Al_2O_3/metal/Al_2O_3 trilayer indicating the metal is the main

contributor to thermal condution. By comparison, the bulk thermal conductivities of W and Ru are 170 and 117 W/mK, respectively. However, the large proportion of Al_2O_3 in the total nanolaminate thickness lowers the measured effective thermal conductivity. Futher discussion of the contribution of Al_2O_3 and the metal layers is presented in section 6.6 and 6.7.

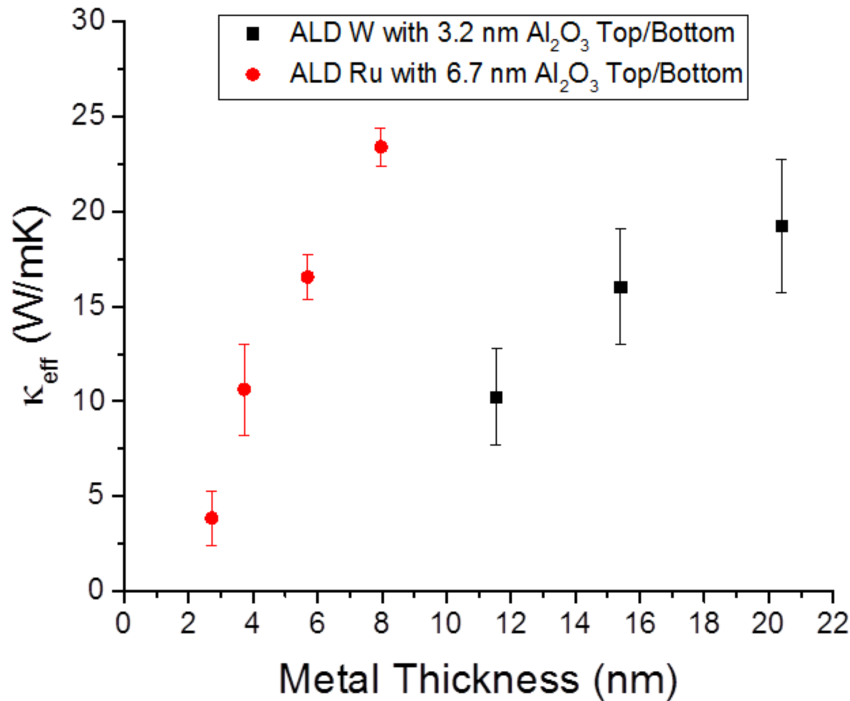

Figure 5.4: Effective thermal condcutivities of $Al_2O_3/W/Al_2O_3$ plotted in black squares and $Al_2O_3/Ru/Al_2O_3$ plotted in red circles with respect to metal thickness. The legend denotes Al_2O_3 layer thicknesses for each sample.

The effective thermal conductivity of the periodic W/Al_2O_3 structures was also measured and shown in Figure 5.5. By adding W periodicity according to Figure 5.2 the total thermal conductivity of the structure was reduced while being kept at a constant total thickness. The multiple effects of thinning the W layers and adding additionl boundaries have reduced the thermal conductivity in the structure. Further detail and modeling will be discussed in Chapter 6.

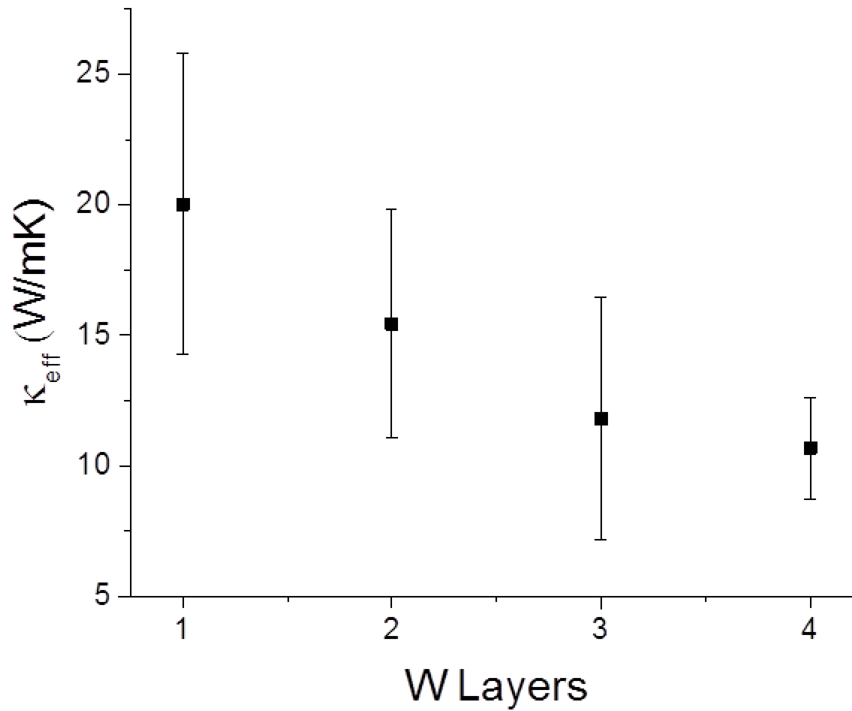

Figure 5.5: Effective thermal conductivity of periodic W/Al_2O_3 structures potted in black squares with respect to number of W layers as denoted in Figure 5.2.

In addition to the single layer and periodic W/Al_2O_3 structures a sample set consisting of a constant W thickness with varying Al_2O_3 top/bottom layers was fabricated and thermal conductivity measured. Figure 5.6 demonstrates the effective thermal conductivity of the Al_2O_3/W/Al_2O_3 trilayer as the top/bottom Al_2O_3 thickness is decreased. The effective thermal conductivity should approach the value of the 20.40 nm W film as the Al_2O_3 is thinned.

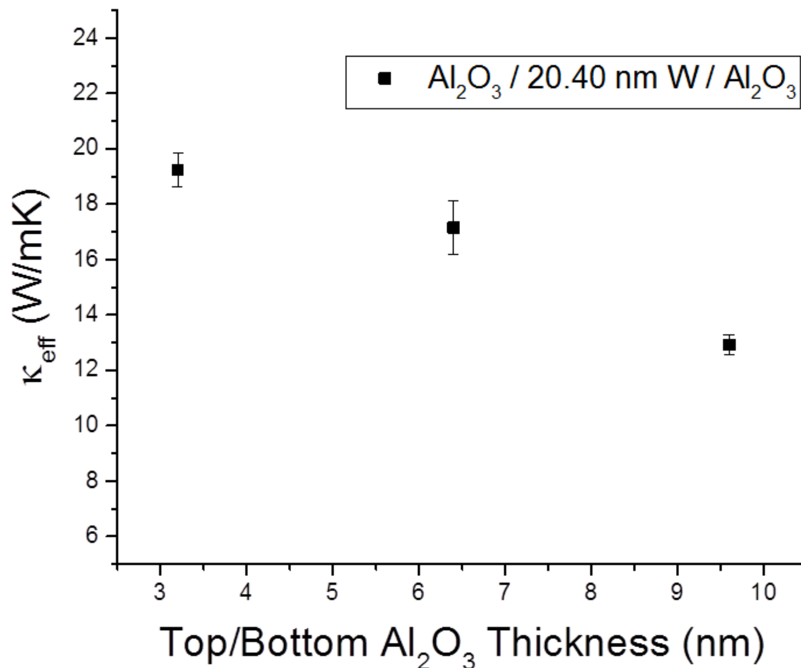

Figure 5.6: Effective thermal conductivity of Al_2O_3/20.40 nm/Al_2O_3 with respect to Al_2O_3 thickness on top and bottom plotted as black squares.

5.5 Specific Heat Capacity of ALD W/Al2O3, ALD Ru/Al2O3 and Periodic ALD W/Al2O3

Using the methods described in section 4.2.5, the effective specific heat capacity (J/gK) was measured for W/Al_2O_3 and Ru/Al_2O_3 structures. Figure 5.7 demonstrates the specific heat capacity of the same sample set from Figure 5.6. Bulk W has a specific heat capacity of ~0.13 J/gK and Al_2O_3 of ~ 0.88 J/gK. As the top/bottom Al_2O_3 thickness is reduced, the effective specific heat capacity decreases towards the value for W. For a sample set of varied W with constant Al_2O_3 thickness (Figure 5.8), the effective specific heat capacity increases with decreasing W thickness.

The effective specific heat capacity of Ru/Al_2O_3 samples was also measured. Figure 5.9 shows the effective specific heat capacity of trilayers of ~ 6.7 nm Al_2O_3/Ru/6.7 nm Al_2O_3 with

varied Ru thicknesses. Reducing the Ru thickness relative to the thicker Al_2O_3 top and bottom layers increases the measured effective specific heat capacity towards the value for Al_2O_3. The data for the thinnest Ru layer resulted in extremely large error. This trend is consistent with the varied W thickness data. More detailed discussion of these trends will be discussed in Chapter 6.

The effective specific heat capacity of the periodic W/Al_2O_3 structure was relatively constant with increasing W-layer periodicity (Figure 5.10). The absolute magnitude of the effective specific heat capacity of the 2-, 3-, and 4-layer periodic strutures are within error of the effective specific heat capacity of the 1-layer W sample.

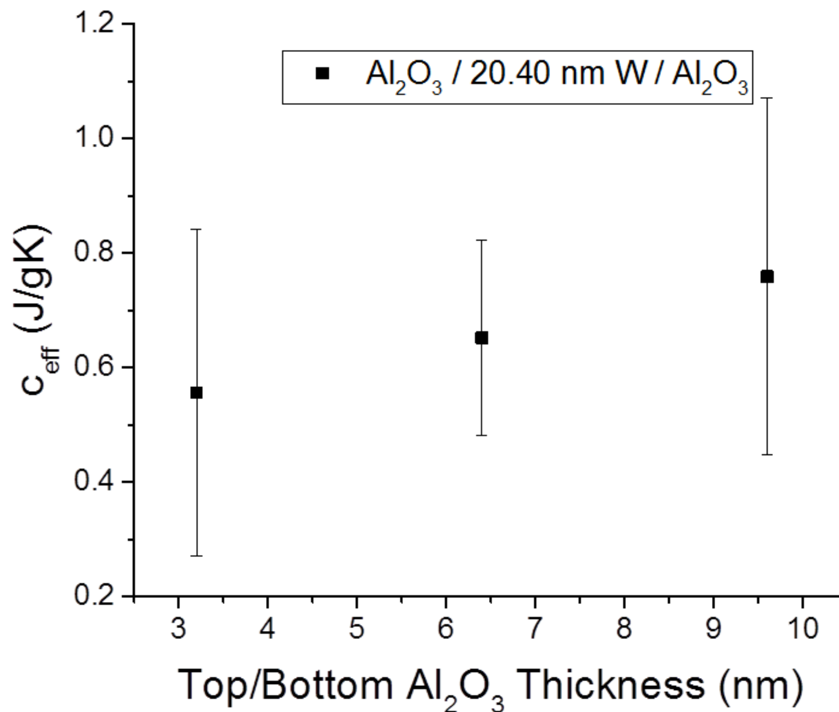

Figure 5.7: Effective specific heat capacity of Al_2O_3/20.40 nm W/Al_2O_3 with respect to top/bottom Al_2O_3 thickness plotted as black squares.

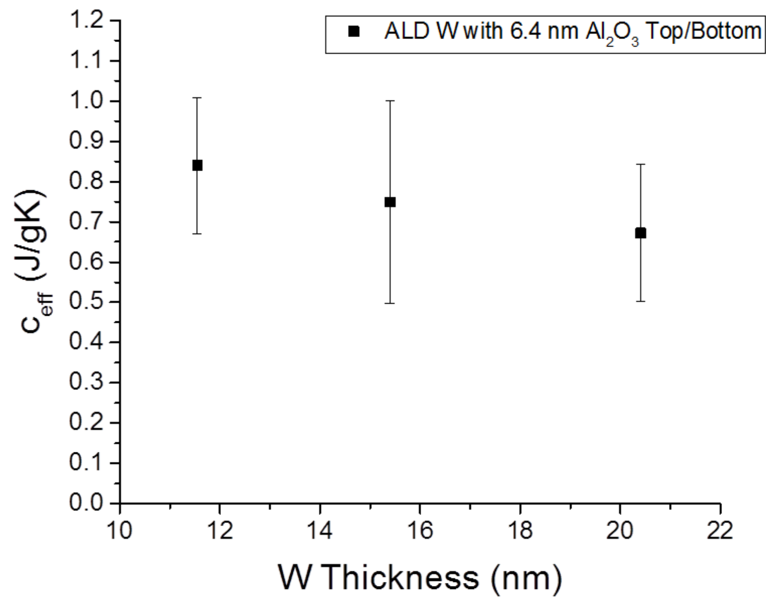

Figure 5.8: Effective specific heat capacity of 6.7 nm Al_2O_3/W/6.7 nm Al_2O_3 with respect to W thickness plotted as black squares.

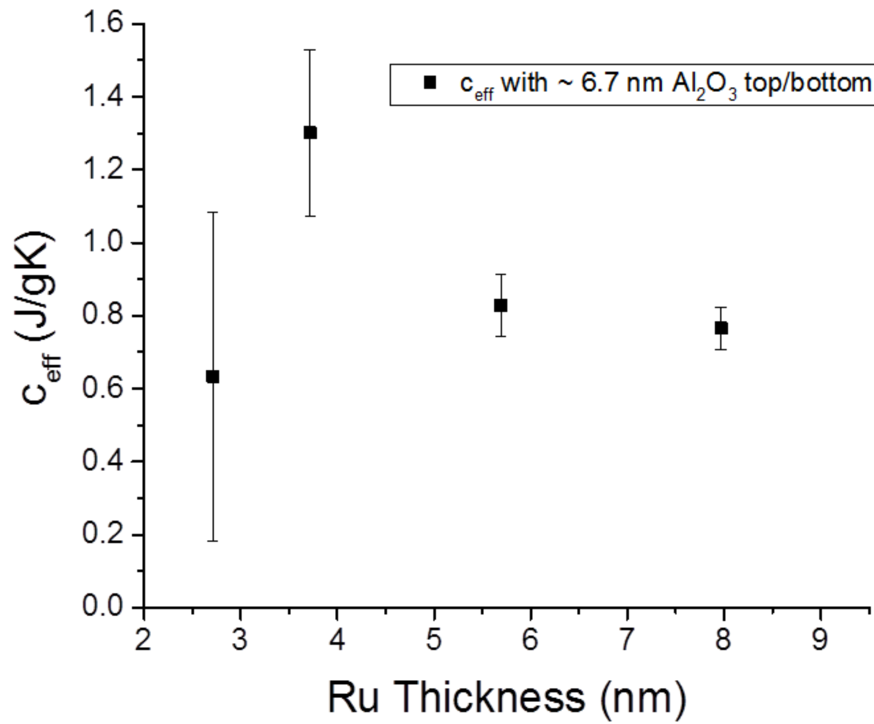

Figure 5.9: Effective specific heat capacity of 6.7 nm Al_2O_3/Ru/6.7 nm Al_2O_3 with respect to Ru thickness plotted as black squares.

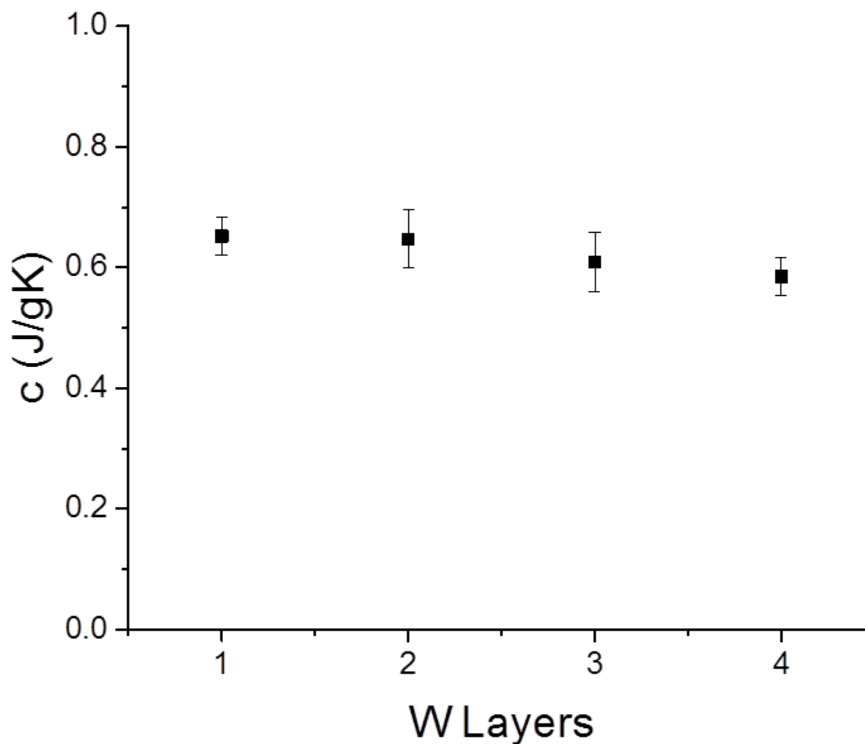

Figure 5.10: Effective specific heat capacity of periodic W/Al_2O_3 with respect to number of W layers denoted by Figure 5.2 plotted as black squares.

5.6 Grain Sizes of ALD W and ALD Ru

To effectively interperet much of the data collected in previous sections of Chapter 5, the grain size of W and Ru ALD films were measured using methods described in section 4.5. In W films GIXRD spectra indicate the presence of β-W in the ALD films, and it is likely that a mixture of both β-W and α-W exist. Thus, single peak and multiple peak fits were used to obtain an upper and lower bound approximations of grain size (Figure 5.11). The average of these methods estimates the grain size for W at ~ 2 nm and suggests an independence of thickness. In Figure 5.11, ALD cycles correspond to a deposition rate of ~ 0.384 nm/cycle.

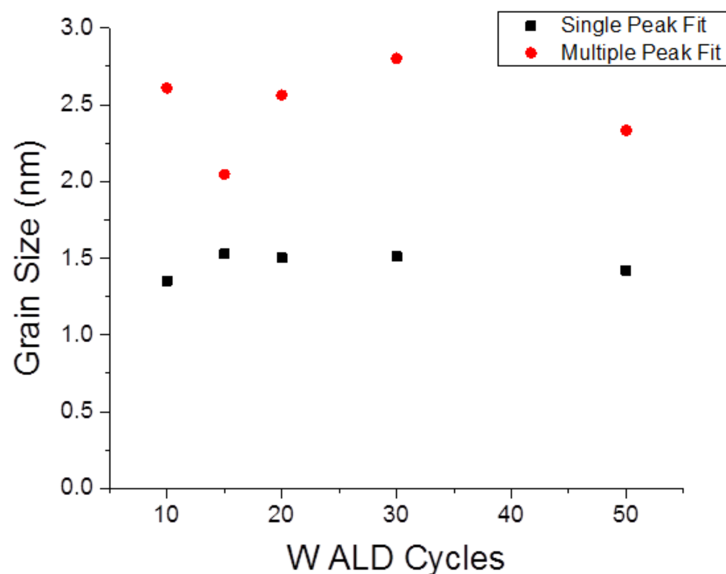

Figure 5.11: Grain size relation to W ALD cycles (thickness).[37] Black square data points are from a single peak fit of GIXRD data. Red circle data points are from an averaged multiple peak fit of GIXRD data for various phases of ALD W.

For the Ru samples, the crystal structure is much more evident and allows the individual fitting of peaks corresponding to the various crystal planes. An average of the strongest peaks for a given thickness can give an estimate of the grain size. Figure 5.12 demonstrates an XRD scan corresponding to a 8.0 nm Ru film with an approximated grain size of ~ 9 nm. Another scan of a 3.7 nm film indicated a grain size of ~ 6 nm, however this was most likely inaccurate due to low intensity and noisy crystal peaks. Measurements of other Ru films did not produce crystal peaks.

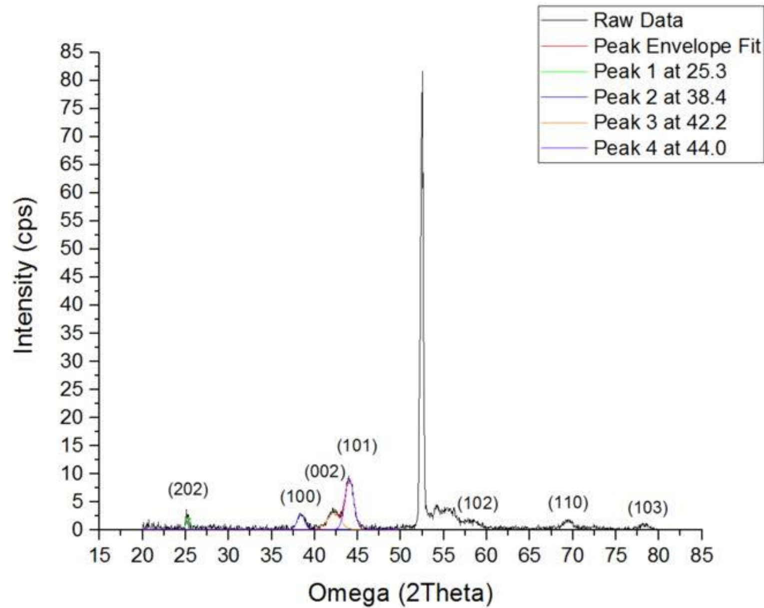

Figure 5.12: XRD data showing a multiple peak fit on a 8.0 nm ALD Ru film.

To better inteperet the electrical and thermal transport for the W and Ru films presented in Chapter 6, an idealized schematic of grain structure and relative thicknesss (approximetely to scale) is demonstrated by Figure 5.13. Data from XRR indicated a continous W film is formed at ~ 2 nm. This nucleation layer is depicted by layer of disordered grains, which forms during a recrystallization process during island coalescnce (Figure 5.13a). Literature studies of ALD Ru using various precursors including the one used in this work, indicate a continous film forming at around 1 – 2 nm as indicated in Figure 5.13b.[98–102] The literature does not comment on the morphology of the nuclation layer in particular, thus, for sake of interperetation, it will be assumed to be disordered in the same nature as the W nuclation layer.

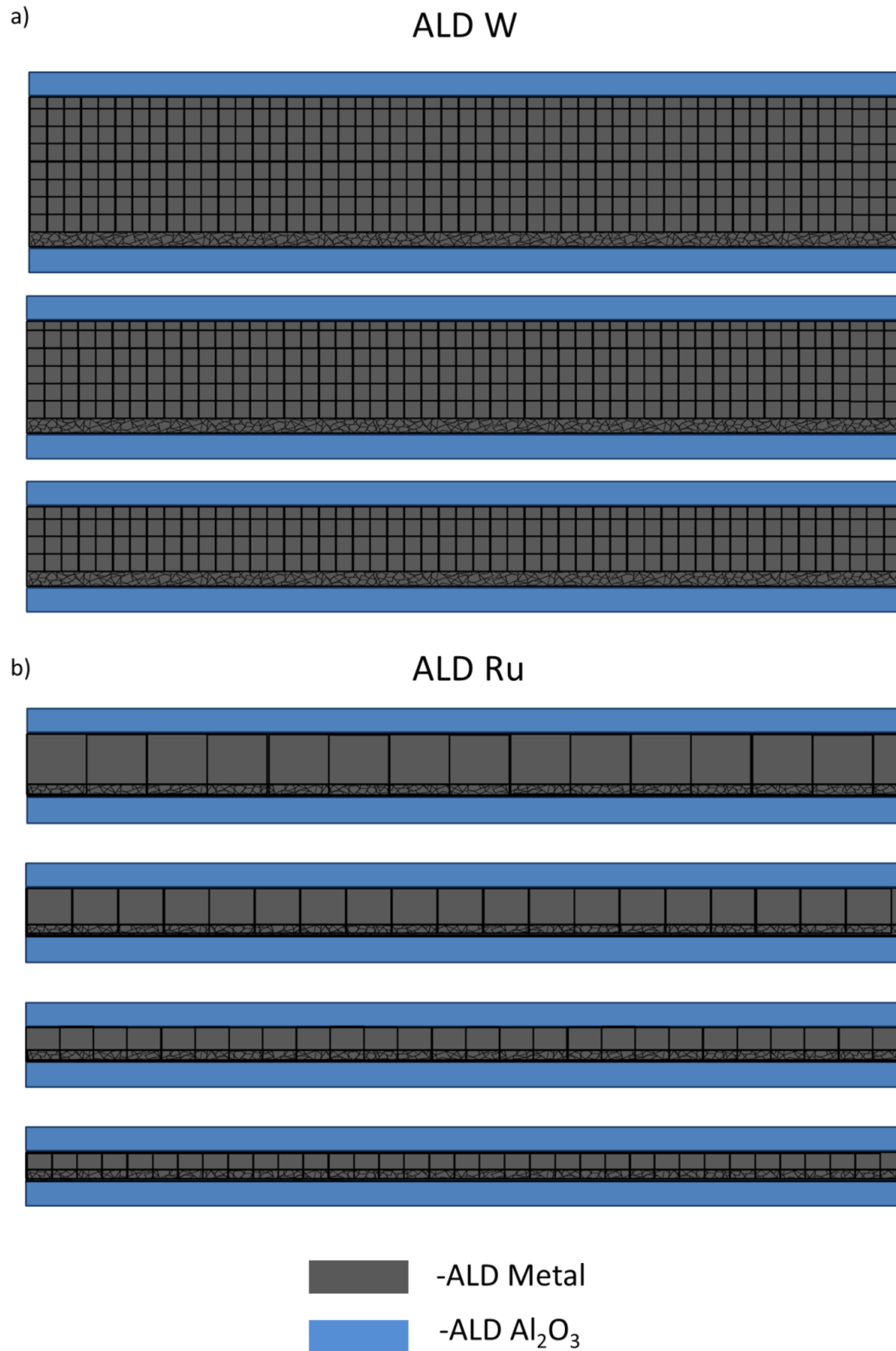

Figure 5.13: Idealized schematic of grain structure and relative thickness in ALD W and ALD Ru with Al_2O_3 capping layers. a) ALD W grain structure and relative thickness with ~ 2 nm nuclation layer made up of disordered grains. b) ALD Ru grain structure and relative thickness with ~ 1 nm nuclation layer.

Chapter 6

Interpretation of Electro-thermal Measurements of W/Al_2O_3 and Ru/Al_2O_3 and Periodic W/Al_2O_3

This chapter will interpret the results presented in Chapter 5 ranging from electrical resistivity, temperature coefficient of resistance, thermal conductivity, specific heat capacity and grain size for W and Ru metal films. Several models will be introduced to better understand the characteristics specific to the ultra-thin metal films produced by ALD including parallel conduction, Fuchs–Sondheimer and Mayadas–Shatzkes models. A discussion of grain size results for W and Ru will aid in the application of these models. Extracted thin film values in comparison to bulk and thickness/grain dependent trends will be discussed. Understanding the physics behind the unique characteristics of these nanoscale structures will aid in the development of future high performance microbolometers and nano-devices.

6.1 Parallel Layer Modeling

The measured $Al_2O_3/W/Al_2O_3$ and $Al_2O_3/Ru/Al_2O_3$ structures are essentially single layer electrical conductors and parallel layer thermal conductors. The metal films contribute the

entirety of electrical conduction via electrons while thermally, the metals offer electron and phonon conduction in conjunction with phonon conduction from the Al_2O_3 layers. The Al_2O_3 layers in question are considered an amorphous oxide and have measured thermal conductivities of ~ 1 – 2.5 W/mK from the literature.[97,103–107] To better understand the conduction properties of the ALD metals, a parallel model may be utilized to extract the thermal conductivities of the individual films. A similar approach may be used for the effective specific heat capacity, as both the metal layers and Al_2O_3 layers contribute to the overall effective specific heat capacity.

A parallel model for effective thermal conductivity and effective specific heat capacity may be given by,

$$\kappa_{eff} = \frac{t_{Al2O3}\kappa_{Al2O3} + t_{metal}\kappa_{metal}}{t_{Al2O3} + t_{metal}}, \quad (6.1)$$

$$c_{eff} = \frac{c_{Al2O3}t_{Al2O3} + c_{metal}t_{metal}}{t_{Al2O3} + t_{metal}}, \quad (6.2)$$

where t is thickness, κ is thermal condcutivity and c is specific heat. For the calcultion of c_{eff} the effective density of the nanolaminates must be utilized. The effective density is defined as,

$$D_{eff} = \frac{D_{Al2O3}t_{Al2O3} + D_{metal}t_{metal}}{t_{Al2O3} + t_{metal}}, \quad (6.3)$$

where D is the density and has been used to prevent confusion with resistivity, ρ. These equations will be utilized in the following sections to extract the individual material properties of ALD Al_2O_3, ALD W, and ALD Ru.

6.2 Traditional Nanoscale Transport Models

It is generally understood that thin films exhibit significant size effects as the surface to volume ratio of the film increases with decreasing film thickness. When the film thickness is on the order of the electron mean free path (MFP) (~10-50 nm for metal films) the boundaries of the film will increase surface scattering. This effect was first modeled by the Fuchs–Sondheimer (FS) theory of surface scattering which partially captures transport scaling in thin films. In FS theory the size effect is modeled by constricting the electron distribution in the Boltzmann equation to a finite z-axis (film thickness).[108] FS theory utilizes a constant term, *p*, that dictates the proportion of specular (*p*=1) or diffuse (*p*=0) scattering at the film surface.[109] The ratio of thin film resistivity relative to bulk is given as,

$$\frac{\rho}{\rho_o} = \left[1 - \frac{3(1-p)}{8\lambda} + \frac{3}{4\lambda}\int_0^{\pi} sin^3\theta|cos\theta| \frac{(1-p)^2 \exp(-\frac{\lambda}{|cos\theta|})}{1-p\cdot\exp(-\frac{\lambda}{|cos\theta|})} d\theta\right]^{-1}, \tag{6.4}$$

where λ is equal to the film thickness divided by the electron mean free path, l_o, and ρ_o is the bulk resistivity.[109] The *p* term is often used as a free parameter in the fitting process, but could also be estimated based on the surface roughness of the films.

While FS theory is often suitable for large grain nanoscale films on the order of 50-100 nm it does not account for the additional scattering effects as films thicknesses fall below 50 nm and their grain structure begins to introduce significant scattering at grain boundaries. The Mayadas–Shatzkes (MS) model best represents grain boundary scattering in thin films. It accounts for electron scattering at grain boundaries and/or impurities through a reflection coefficient *R*. Figure 6.1 demonstrates the qualitative approach by the MS model to model electron reflection at grain boundaries by delta potentials. The full model incorporates both the FS size effect from surface scattering and grain boundary scattering. The simplified model may

be used to describe the dominant effect of grain boundary scattering. The grain boundary resistivity, ρ_g is given as,

$$\frac{\rho_g}{\rho_o} = \left[3(\frac{1}{3} - \frac{1}{2}\alpha + \alpha^2 - \alpha^3 \ln\left(1 + {}^{1}/_{\alpha}\right))\right]^{-1}, \qquad (6.5)$$

where α describes the grain boundary potential strength by,

$$\alpha = \frac{l_o}{G}\frac{R}{1-R}, \qquad (6.6)$$

where l_o is the electron MFP in the bulk material, G is the grain size and R is the electron reflection coefficient for a grain boundary.[110] For films that exhibit both a grain boundary resistance and size effect resistance of comparable magnitude, the full MS model is more suitable, which combines grain boundary resistivity from equation 6.4 and the FS size effect. The full MS model resistivity is given by,

$$\rho_f = \left\{\frac{1}{\rho_g} - \frac{6}{\pi\kappa_o\rho_o}(1-p)\int_0^{\pi/2} d\phi \int_1^{\infty} dt \frac{cos^2\phi}{H^2(t,\phi)} \times \left(\frac{1}{t^3} - \frac{1}{t^5}\right)\frac{1-e^{[-\kappa_o t H(t,\phi)]}}{1-pe^{[-\kappa_o t H(t,\phi)]}}\right\}^{-1}, \qquad (6.7)$$

where,

$$H(t,\phi) = 1 + \alpha/cos\phi(1 - \frac{1}{t^2})^{1/2}, \qquad (6.8)$$

$$\kappa_o = t/l_o. \qquad (6.9)$$

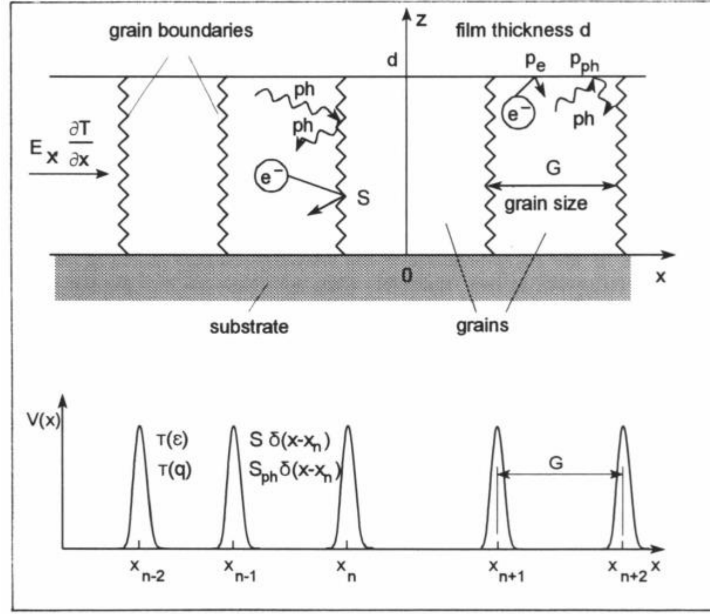

Figure 6.1: Qualitative model of electron and phonon conduction through polycrystalline films. Grain boundaries act as energy potential with strength *S* resulting in added phonon or electron resistance.[111]

Analogous to the surface scattering effects for electrons, phonons will experience size effects as film thickness decreases. Surface and grain boundary scattering will begin to dominate other phonon-phonon and phonon-electron scattering effects and may be described by an adapted MS model for phonon conduction. Voelklein and Kessler derived a grain boundary and surface boundary scattering model for phonon conduction in polycrystalline films by adapting the approach from Mayadas and Shatzkes.[112] Similar to R in the electrical MS model, there is an analogous term S_{ph} that represents the strength of a grain boundary potential that may scatter phonons. Again, Figure 6.1 demonstrates the basic idea of a delta potential associated with grain boundaries. The film thermal conductivity is given as,

$$\kappa_{ph}=\kappa_{ph,bulk}g_{ph}(d,G), \tag{6.10}$$

where $\kappa_{ph,bulk}$ is the bulk material thermal conductivity and $g_{ph}(d,G)$ is given as,

$$g_{ph}(d,G)=\frac{\int_0^{\Theta/T}\frac{x^4e^x}{(e^x-1)^2}\tau_q(x)\left\{1+\frac{3}{2}\gamma+\frac{3(1-p_{ph})}{8K}\right\}^{-1}dx}{\int_0^{\Theta/T}\frac{x^4e^x}{(e^x-1)^2}\tau_q(x)dx}, \quad (6.11)$$

with $\gamma=\frac{2S_{ph}^2\tau_q(x)}{\hbar^2 vG}$, $x=\frac{\hbar\omega}{k_bT}$, $K=\frac{d}{\tau_q(x)v}$.[31]

For the above relations, τ_q is the phonon-phonon umklapp scattering relaxation time for inter-grain scattering, ω is the Debye frequency, v is the sound velocity, Θ is the Debye temperature, and p_{ph} is the parameter of surface scattering. The umklapp scattering relaxation time may be modeled as[112],

$$\tau_q(\omega)={}^{\tau_{u0}}/_{k_BT\omega^2}, \quad (6.12)$$

and applied to equation 6.11 to obtain the following relation,

$$g_{ph}(d,G)\approx\frac{\int_0^{\Theta/T}\frac{x^2e^x}{(e^x-1)^2}\left(1+\frac{\gamma_1}{x^2}+\frac{\gamma_2}{x^2}\right)dx}{\int_0^{\Theta/T}\frac{x^2e^x}{(e^x-1)^2}dx}, \quad (6.13)$$

where $\gamma_1=\frac{3S_{ph}^2\tau_{u0}}{vG(k_bT)^3}$, $\gamma_2=\frac{3(1-p_{ph})v\tau_{u0}\hbar^2}{8d(k_bT)^3}$.

Here, τ_{u0} and S_{ph} become fitting parameters for g_{ph}, where g_{ph} must be solved numerically.

While there exists extremely detailed theory of phonon-phonon and phonon-electron interactions in nanoscale structures, the dominant scattering mechanisms have been described above by the FS and MS models and are suitable for the scope of this dissertation. Discussions of these models applied to data for W and Ru will be provided in the following sections.

6.3 Grain Size Discussion

As shown in the conduction models presented in the previous section, grain size is an important consideration in the overall description of electron and phonon conduction as the size of the grains will dictate the number of boundaries involved in the scattering of electrons and phonons over their respective MFPs. The results for ALD W indicate an average grain size of 2 nm, independent of thickness. The lack of thickness dependence in grain size is unusual for thin films. Often thin films nucleate and continue to grow with grain sizes on the order of the film thickness for films under 20 – 50 nm. The grain size will then continue to grow on the order of the film thickness for films under 30 – 50 nm. This has been witnessed in the studied ALD Ru and Cu, Al and Pt films from the literature.[42,113,114]

Grain size during film growth may be better understood by the temperature zone model presented by Barna and Adamik.[115] Given the ratio of T_s/T_m where T_s is the substrate temperature during film growth and T_m is the melting point of the elemental material, a microstructural evolution model may predict the growth mechanisms and thus give a better estimation of the expected grain size.[115] Figure 6.2 demonstrates the basic temperature zone model. The ALD W in question was deposited at 130 °C and has a T_s/T_m of ~ 0.04 which falls in the extremely low range of Zone I in the microstructural evolution model. In the lower end of Zone I the nucleation density essentially determines the grain size throughout the film thickness. It is composed of extremely small fibers on the order of several nm's which form bundles and are homogeneous throughout the film thickness. This basic model and interpretation is consistent with the measured grain properties of ALD W.

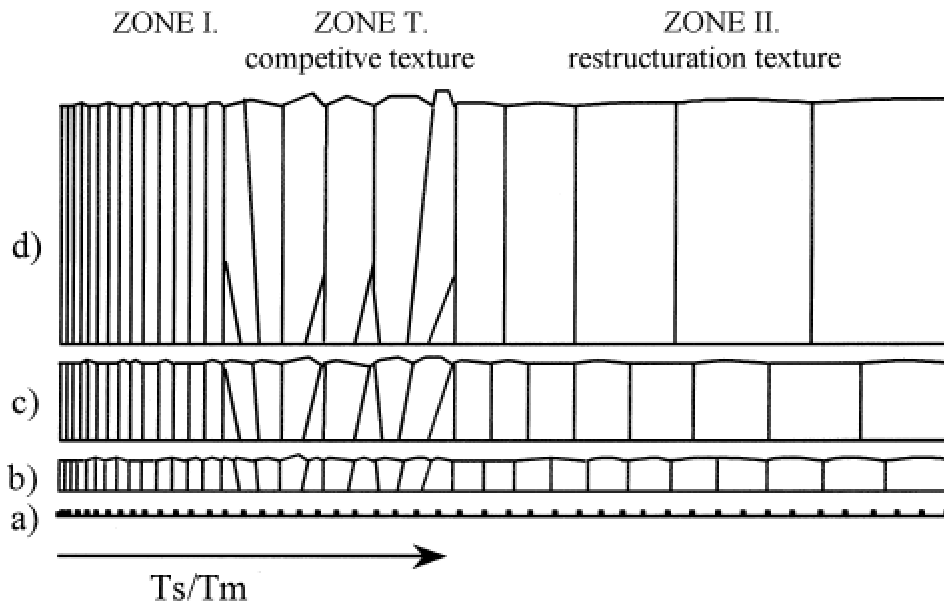

Figure 6.2: Temperature zone model for microstructural evolution during film growth.[115] Zone I, Zone T, and Zone II correspond to a T_s/T_m from 0 – 0.2, 0.2 – 0.4 and > 0.4, respectively. Layers a), b), c) and d) correspond to film thickness growth.

Though the data for Ru grain size was incomplete, the grain sizes for the two measured films indicate a grain size on the order of the film thickness, i.e. 9 nm for a 8.0 nm film and 6 nm for a 3.7 nm film. Previous studies of ALD Ru and TiN films by Milligan and Li demonstrate grain size versus film thickness for several ALD metal films (Figure 6.3).[116] In the region above 10 nm, the grain size is saturated at different sizes corresponding to different materials. Below 10 nm, the curves converge into a linear relationship wherein the grain size is approximately equal to the film thickness. However, the structure zone model for ALD Ru indicates T_s/T_m is ~ 0.12, falling in the middle of Zone I. In this zone as described above, the nucleation density determines the grain size and a smaller grain structure than measured might be expected. Barnes and Adamik have also shown the effect of impurity species as either inhibiting or promoting grain size, i.e. Zone I materials may act more like Zone T materials with grain growth "promoters" or Zone T materials may act like Zone I materials with grain growth "inhibitors". Studies by

Aaltonen et al. show ALD Ru films deposited at 300 °C resulted in larger grain structure also corresponding to a larger O_2 impurity content in the film when compared to films deposited at 400 °C and 500 °C.[101] In this sense, oxygen may act as a grain promoter for ALD Ru growth at 300 °C. For further analysis in the following chapters, it will be assumed that the ALD Ru grain size is equal to the film thickness.

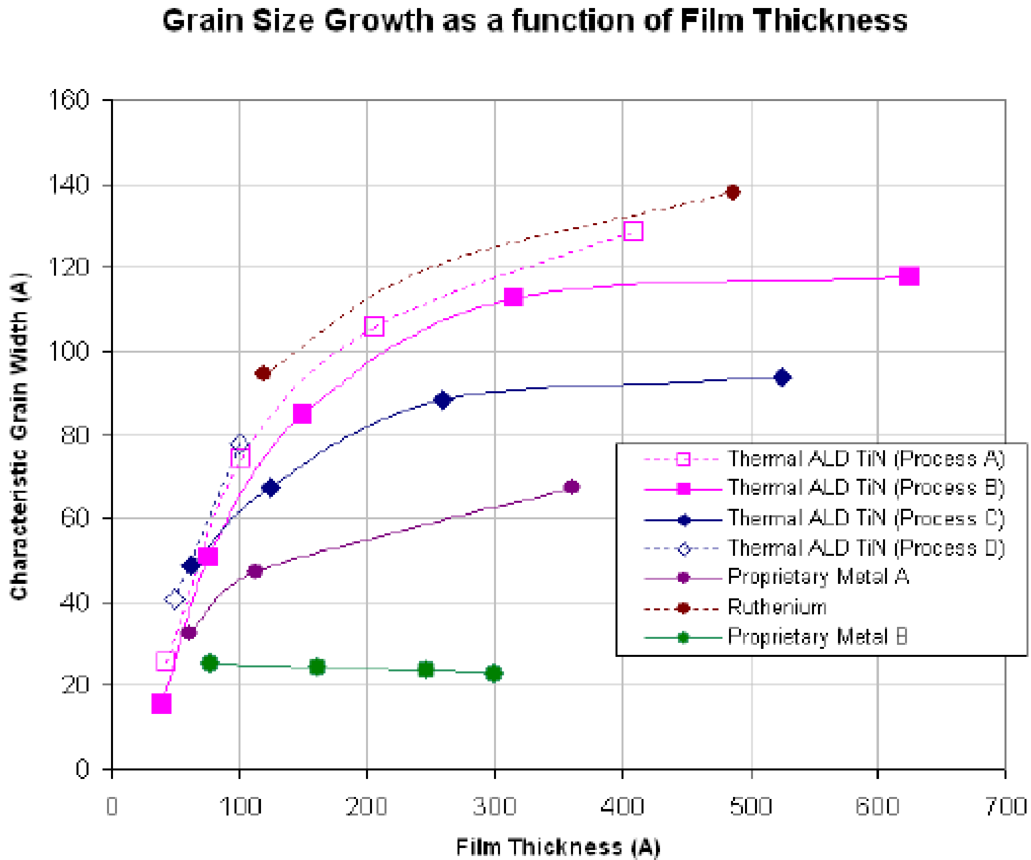

Figure 6.3: Grain width versus film thickness for several ALD generated materials.[116] Each material has a different grain width saturation above 20-30 nm in thickness, but approximately identical linear relationships below 10 nm.

6.4 Electrical Resistivity in ALD W and ALD Ru

The electrical resistivity for W and Ru was modeled by both the FS and MS models presented in section 6.2. Even for completely diffuse scattering (p = 0), the FS model drastically

undershoots the experimental W resistivity. Since the W is nano-crystalline with 2 nm grains independent of thickness, the data are more accurately modeled by using the grain resistivity MS model, equation 6.5 (black solid line in Figure 6.4). A thickness-dependent electron reflection coefficient, *R*, must be utilized to properly fit the data. This might suggest a significant size effect due to layer boundary thinning, however using the full MS model from equation 6.7 resulted in a negligible change in the predicted resistivity suggesting another scattering effect is influencing electron transport with decreasing film thickness. Previous work with ALD Pt films explained a thickness dependent *R* value through the concept of varied density with Pt thickness, however, nucleation studies of ALD W show a constant density at the thicknesses studied.[14,42] The thickness dependent effect for *R* is likely attributed to a disordered layer formed during the recrystallization of grains in the W nucleation phase as demonstrated in Figure 5.13.[14] A base layer of extremely disordered grains increases electron scattering (*R*) for thinner films. The label "disordered" may include the combination of several effects including smaller grains, grain with less crystal structure and/or grains with larger grain separation by impurities. This hypothesis is supported by the measurement of a negative temperature coefficient of resistance (TCR) for ALD W, opposite of the expected positive metallic effect. Specifically, thinner films exhibit a larger negative TCR with measured values of -0.015, -0.012 and -0.009 % K^{-1} for 11.6, 15.4 and 20.4 nm W films, respectively. Thinner films contain a larger scattering contribution from the disordered nucleation layer which contributes to a negative TCR effect through electron grain hopping. These negative TCR contributions overcome the inter-grain metallic positive TCR contribution. Further discussion of TCR will be included in section 6.5

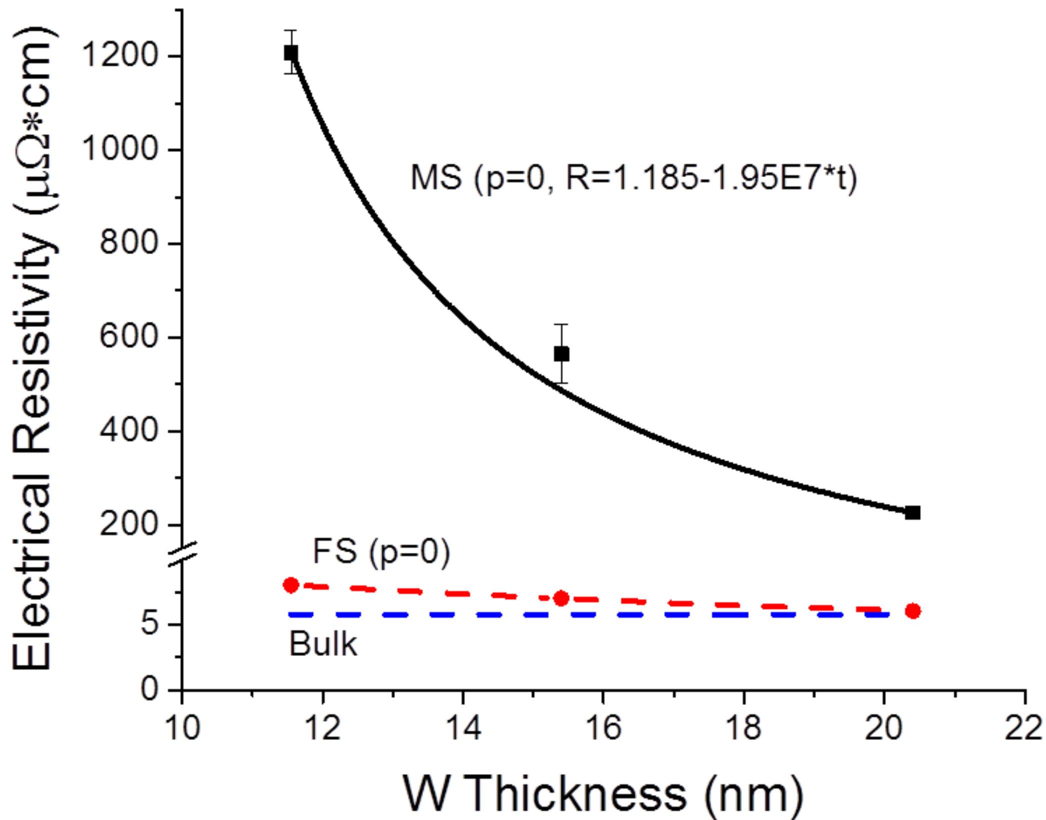

Figure 6.4: Measured electrical resistivity of W films at room temperature at three thicknesses are plotted as black squares. The bulk W resistivity is shown as the blue dashed line. The upper bound FS model (p=0) is shown as the red dashed line. The solid black line is the thickness dependent MS model.

The measured resistivity is much lower for ALD Ru, only about 2x – 3x the bulk resistivity as shown in Figure 6.5. This suggests that the resistivity may not be dominated entirely by grain boundary resistance and a significant size effect may be present for decreasing film thickness. However, the FS undershoots the experimental resistivity data, even for $p = 0$. From this result, it is apparent that the MS model should be utilized. Here, the resistivity is a combination of contibutions from both grain boundary scattering and boundary size effect scattering, suggesting the use of the full MS model which incorporates both of these effects. Equation 6.7 was fit to the electrical resitivity data for ALD Ru where the grain size was

assumed equal to the film thickness as discussed in the previous section. For the three thickest samples a constant R value of 0.49 provided an accurate fit. For the thinnest sample, an R value of 0.80 was needed. Here, the average grain size is assume to be ~ 3 nm where the film thickness is also ~ 3 nm. The nucleation layer as depicted in Figure 5.13 may be introducing additional scattering, increasing R as witnessed in the W films. At this thickness it is possible the film is quasi-continious, and the grain seperation may be larger than in the thicker films, introducing a significant increase in resistivity.

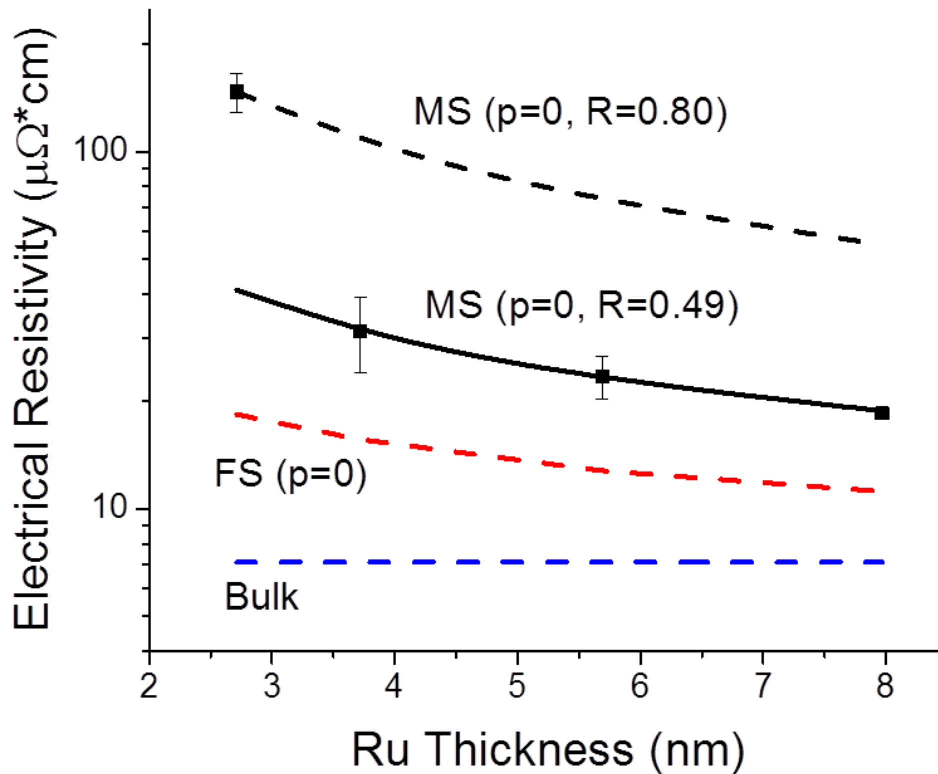

Figure 6.5: Measured electrical resitivity of Ru films at room temperature at four thicknesses are plotted as black squares. The bulk Ru resistivity is shown as the blue dashed line. The upper bound FS model (p = 0) is shown as the red dashed line. The solid black line MS model from equation 6.7 for $p = 0$ and $R = 0.49$. The black dashed line is the MS model from equation 6.7 for $p = 0$ and $R = 0.80$.

6.5 TCR of ALD W and ALD Ru

The W films exhibit a negative TCR effect, similar to many semiconductors. This is contrary to bulk-like metal films which exhibit a positive linear effect governed by the scattering of electrons by phonons wherein increased heat produces a higher rate of electron-phonon scattering and higher electrical resistivity. Traditional MS models presented in section 6.2 adapted to TCR do not capture the negative TCR effect witnessed in ALD W – only the reduction in positive TCR with decreasing film thickness and grain size.[117] This non-metallic behavior has been witnessed in several previous studies of nano-structured metals and is entirely attributed to the grain structure of the metal. Qin et al. and Yushuang et al. have witnessed negative TCR values in nano-crystalline Ag and Bose et al. in nano-crystalline bulk Nb.[118,118,119] Bose et al.'s studies of nano-crystalline bulk Nb indicated a metal-insulator transition and TCR sign change from positive to negative below 8 nm crystallite sizes, wherein the resistivity was 10's of mΩ*cm (~ 2 orders of magnitude larger than the ALD W).[119] They attributed both the metal-insulator and TCR sign change to a significant effect from the distance between grains, roughly on the order of 1 nm and made up of amorphous oxide material. To interpret this effect of film morphology, grain hopping models often applied to semiconductor materials were applied to their transport data. These models were unsuccessful in describing the transport and they attributed the unusual transport data to the height of the electrical potential associated with the grain boundary spacing distance. Yushuang et al. demonstrated that the quantum size effect is predicted for Ag films with crystallite sizes below 20 nm.[118] The quantum size effect causes quasi-continuous electron energy levels to form distinctively separate energy levels in the grain structure, increasing the resistivity. In this case, an increase in temperature increases the electron carrier concentration and decreases the resistivity. This effect dominates of the converse effect of carrier mobility decreasing with increasing temperature.

The proposed mechanism from Bose et al. regarding grain separation may be consistent with the results for ALD W. Wind et al., Wilson et al., Elam et al. and EDX line scans of the samples measured here have shown a Si inclusion in the W films.[14,25,120] It is not unrealistic to assume that a larger majority of impurities are located in the disordered base layer, increasing the separation between grains and thus temperature dependent grain hopping (increasing negative TCR). Work by Vancea et al. empirically witnessed quantum transport effects in nanostructured films and Reiss et al. modeled their results using quantum mechanical transfer matrix calculations.[121,122] Reiss et al. derived a thin film conductivity given by a modified Drude model,

$$\sigma = \left(\frac{ne^2 l}{mv_F}\right) grain(l, G, T^*), \tag{6.14}$$

where n is the free electron number density, e is the charge of an electron, m is the mass of an electron, v_F is the fermi velocity, l the MFP of an electron, G is the grain size T^* is the quantum mechanical transmission coefficient along any direction and *grain(l,D,T*)* is the grain dependent adjustment. Reiss et al. confirmed the empirical model by Vancea et al. showing that in the first order approximation,

$$grain(l, G, T^*) = {T^*}^{l/G}. \tag{6.15}$$

To attempt to explain the negative TCR of W, a grain boundary adjusted TCR relation may be derived from equation 6.14 and given as,

$$TCR = Bl[1 - \left(\frac{l}{G}\right)\ln\left(\frac{1}{T^*}\right)], \tag{6.16}$$

where B is a constant > 0 associated with the material's MFP temperature dependence. It can be seen that for TCR to be negative the following relation must be satisfied,

$$\left(\frac{l}{G}\right) \ln\left(\frac{1}{T^*}\right) > 1 \,. \tag{6.17}$$

For ALD W, this condition is met using the bulk MFP, grain size of 2 nm and T* defined as,[121]

$$T^* = 1 - \frac{R}{2}, \tag{6.18}$$

where R is the reflection coefficient at perpendicular incidence for different thicknesses used in the MS model from section 6.4. Using B as a free parameter, equation 6.16 was fit to the W TCR data in Figure 6.6. Remarkably, the model fit is accurate, matching well with the thinner W layers and implying the electron reflection coefficients from the MS resistivity modelling correlate well with Reiss et al.'s model for conduction. There is some discrepancy in whether the MFP should be defined with a thickness dependence. However, the assumption of a bulk mean free path is valid considering Vancea et al. also showed that defining a MFP for the whole of a nanocrystalline solid is convoluted and that only the background scattering MFP can be defined.[123] To further increase the model accuracy, B could be measured for a bulk nanocrystalline W structure (> 50 nm thickness) with morphology similar to the measured ALD films with 2 nm grain structure. The current model by Vancea et al. with B as a free parameter results in B= 7331 m^{-1} K^{-1} and describes the behavior of the ALD W TCR accurately.

ALD Ru shows a positive TCR trend with decreasing magnitude with decreasing film thickness. This trend is consistent with previous literature of ALD Pt films and the Matthiessen rule.[23] However, the model presented by Vancea et al. is poorly fit to the data in Figure 6.7 using an R value of 0.49 from the MS fit of electrical resistivity and equation 6.16. The size effect here is underrepresented by the assumption of a smaller mean free path of 10 nm. If a larger MFP is used, the size effect is enhanced and an improved fit may be achieved. However, this is exactly

the problem Vancea et al. has identified for defining the mean free path of a nanocrystalline thin film.[123]

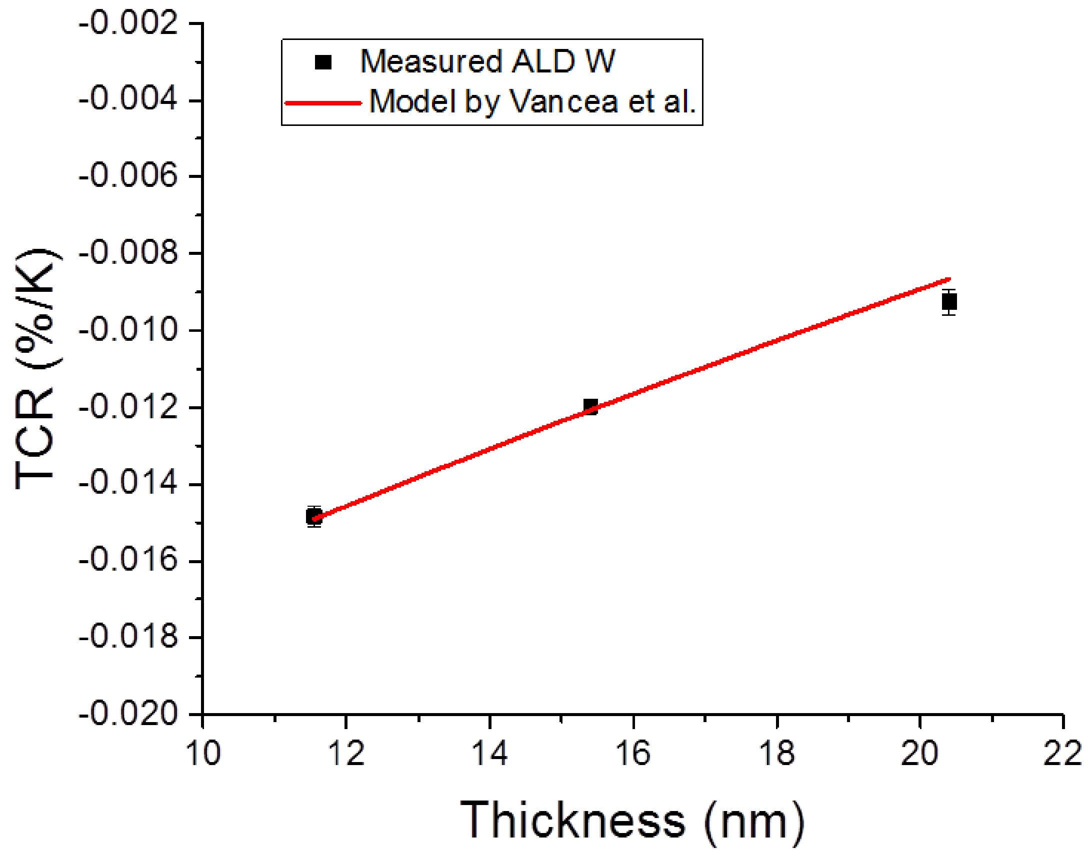

Figure 6.6: TCR of ALD W with respect to thickness plotted as black squares. The red line corresponds to a model fit by equation 6.16.

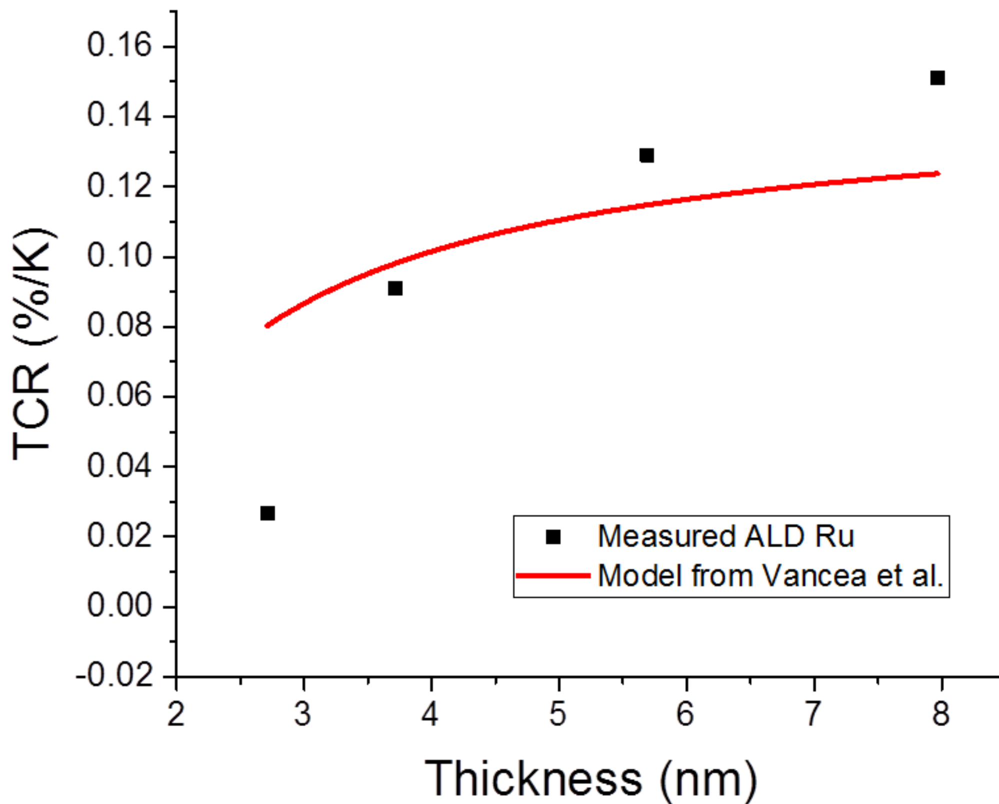

Figure 6.7: TCR of ALD Ru with respect to thickness plotted as black squares. The red line corresponds to a model fit by equation 6.16.

6.6 Thermal Conductivity of ALD Al_2O_3

To better understand the thermal conductivity of the ALD metal layers investigated, the thermal conductivity contribution of ALD Al_2O_3 must be addressed. Using the relative thicknesses of the Al_2O_3 and metal layers of a trilayer, the effective thermal conductivity may be modeled by equation 6.1 from section 6.1. To extract the thermal conductivity of the metal layers, a value for the thermal conductivity of Al_2O_3 must be settled on. As mentioned in section 6.1, the thermal conductivity of amorphous oxides is often in the 1 – 3 W/mK range. To investigate the thermal conductivity of the Al_2O_3 films utilized in the presented measurements a

parallel model can be utilized to extract the thermal conductivity of sub 10 nm Al_2O_3 on W. Figure 5.7 from section 5.4 was fit with a parallel model from equation 6.1 in Figure 6.8 with κ_{Al2O3} and κ_W as free parameters. The extracted thermal conductivity for sub 10 nm Al_2O_3 was 1 ± 3 W/mK. This level of error is consistent with sub 10 nm films measured by Luo et al and does not imply that the thermal conductivity may be negative.[104]

The thermal conductivity of amorphous Al_2O_3 thin films has been studied previously. Work by Luo et al., Gorham et al. and Lee et al. has characterized the thermal conductivity of ALD and sputtered Al_2O_3 with values around ranging from 1 – 3 W/mK. Gorham et al.'s films were on the order of 50 nm and measured using time-domain thermoreflectance, obtaining a value of ~1.6 W/mK for ALD Al_2O_3 deposited films. Luo et al.'s ALD Al_2O_3 films were measured down to 5 nm, using a micro-raman technique, but with large error for the thinnest samples. Lee et al.'s sputtered Al_2O_3 were measured at ~ 140 nm in thickness using the 3ω technique with a suspended metal heater and resulted in a value of ~ 1 W/mK. Figure 6.9 demonstrates the data from Luo et al. and Lee et al. Below 10 nm, the thermal conductivity of Al_2O_3 was shown to decrease below the kinetic minimum thermal conductivity for Al_2O_3 (neglecting size effects) presented by Stark et al. (Figure 6.9a).[105] Both data from Luo et al. and Lee et al. are consistent with the extracted thermal conductivity value presented here for amorphous Al_2O_3.

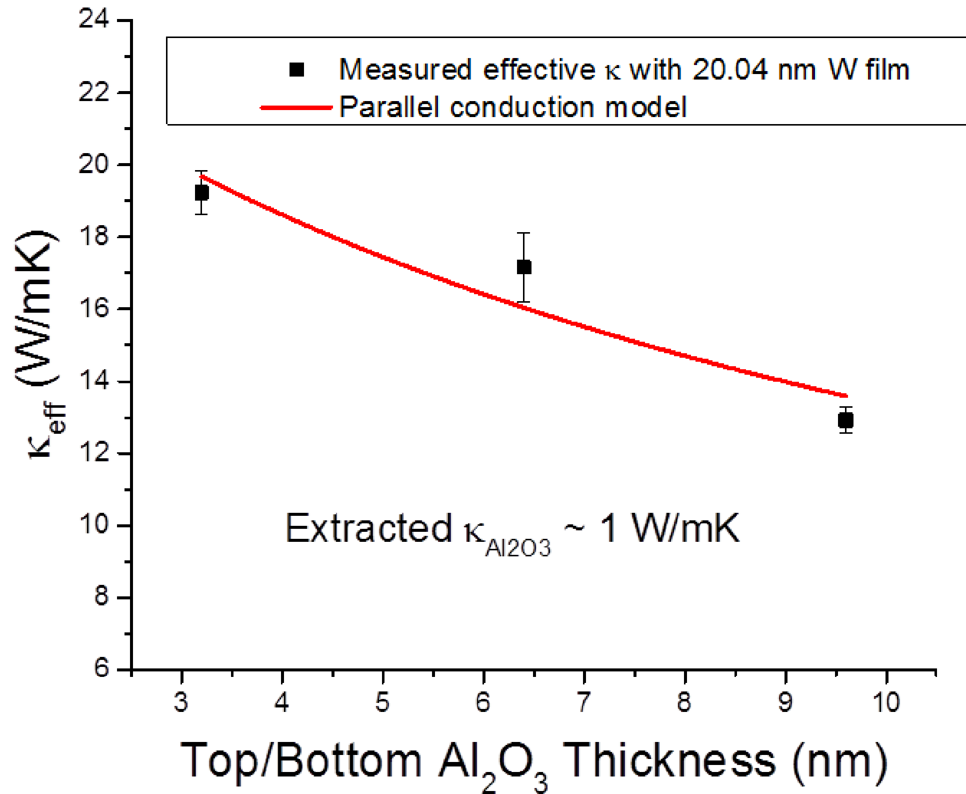

Figure 6.8: Effective thermal conductivity of Al_2O_3/W/Al_2O_3 with respect to top/bottom Al_2O_3 thickness plotted as black squares fit by equation 6.1 (red line).

It is possible there is a thickness dependent conductivity value for Al_2O_3 at these thicknesses since the size effect has been predicted and witnessed in ultra-thin film SiO_2 thermal conductivity measurements by Goodson et al..[124] However, the extracted value presented here will serve as an acceptable estimate for extraction of the metal thermal conductivities of Ru and W from their associated Al_2O_3 trilayer stacks. To date, there is no previous literature on the thermal conductivity of ALD deposited Al_2O_3 at sub 5 nm thicknesses.

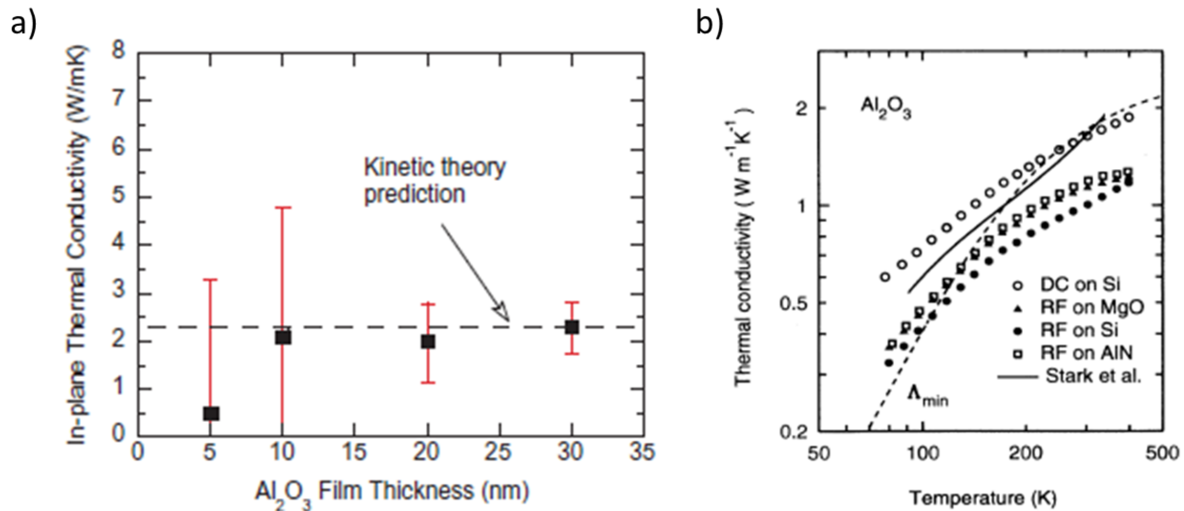

Figure 6.9: Data from Luo et al. and Lee et al. for the thermal conductivity of amorphous Al_2O_3.[104,107] a) Thermal conductivity of ALD Al_2O_3 at various thicknesses. b) Thermal conductivity of amorphous Al_2O_3 deposited on different substrates by various techniques.

6.7 Thermal Conductivity of ALD W and ALD Ru

To better interperet the conduction mechanisms in the metal films from the measured W/Al_2O_3 and Ru/Al_2O_3 nanolaminates, the thermal conductivity of just the W and Ru films were extracted using the parallel model from equation 6.1, assuming an Al_2O_3 thermal conductivity of 1 W/mK.

Figure 6.10 and Figure 6.11 demonstrate the extracted thermal conductivity values for W and Ru respectively. The comparison here between W and Ru is less convoluted since the effect of the Al_2O_3 has been removed. Since the Ru/Al_2O_3 structure had ~ 2x the thickness of Al_2O_3 than the W/Al_2O_3 structures, the effective thermal conductivity was lowered. Here, it is clearly seen that Ru has a significantly larger thermal conductivity compared to W. Even at thicknesses of 3 – 4 nm the Ru thermal conductivity is larger than that of a 20.4 nm W film. The majority of this effect is attributed to the higher degree of electron thermal conduction in the Ru due to its much lower electrical resistivity. For both films the thermal condcutivity is significantly reduced

from bulk. Bulk W and Ru have thermal conductivities of 173 and 117 W/mK respectively and are displayed in Figure 6.10 and Figure 6.11. At the thinnest thicknesses presented here, ALD W and ALD Ru have reduced thermal conductivities of 91% and 83%, respectively.

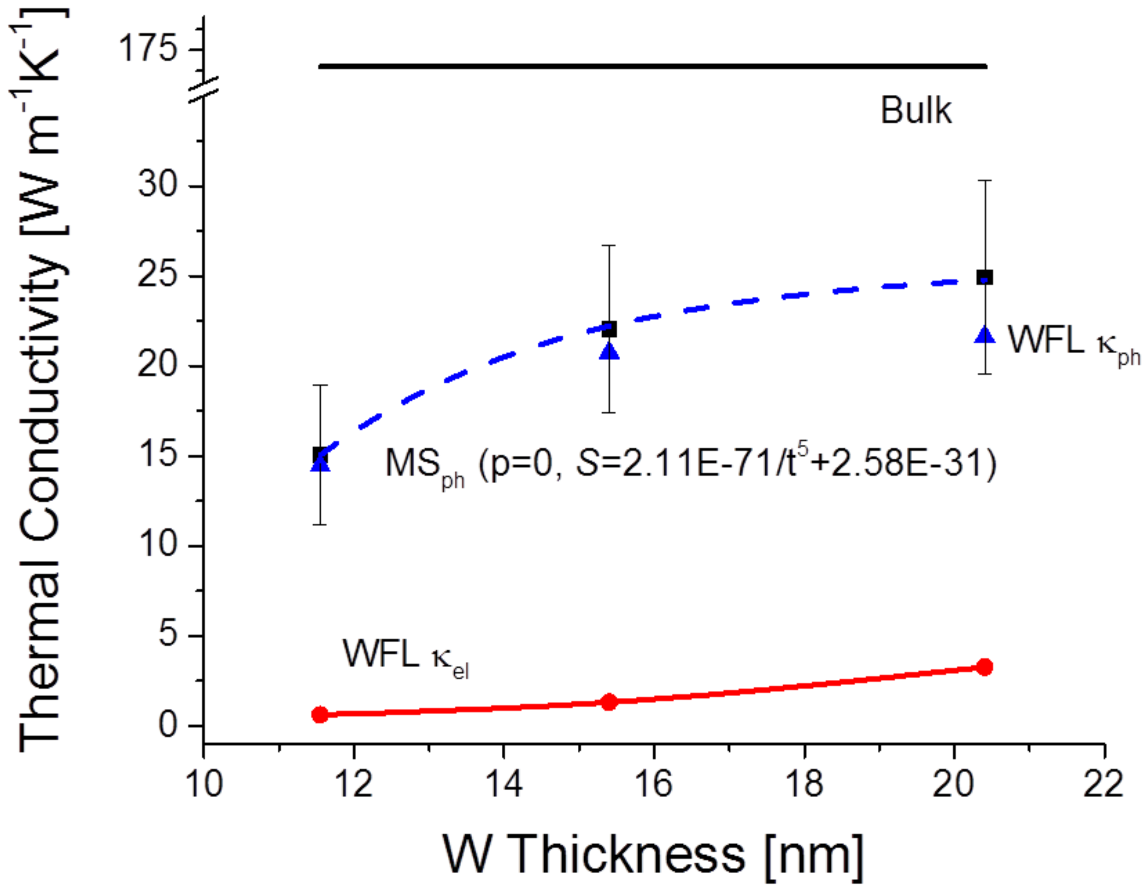

Figure 6.10: Measured thermal conductivity of ALD W with respect to thickness plotted as black squares.[37] The black line is the bulk value. The red circles are WFL calculated κ_{el} values. The blue triangles are WFL calculated κ_{ph} values. The blue dashed line is the thickness dependent MS_{ph} model.

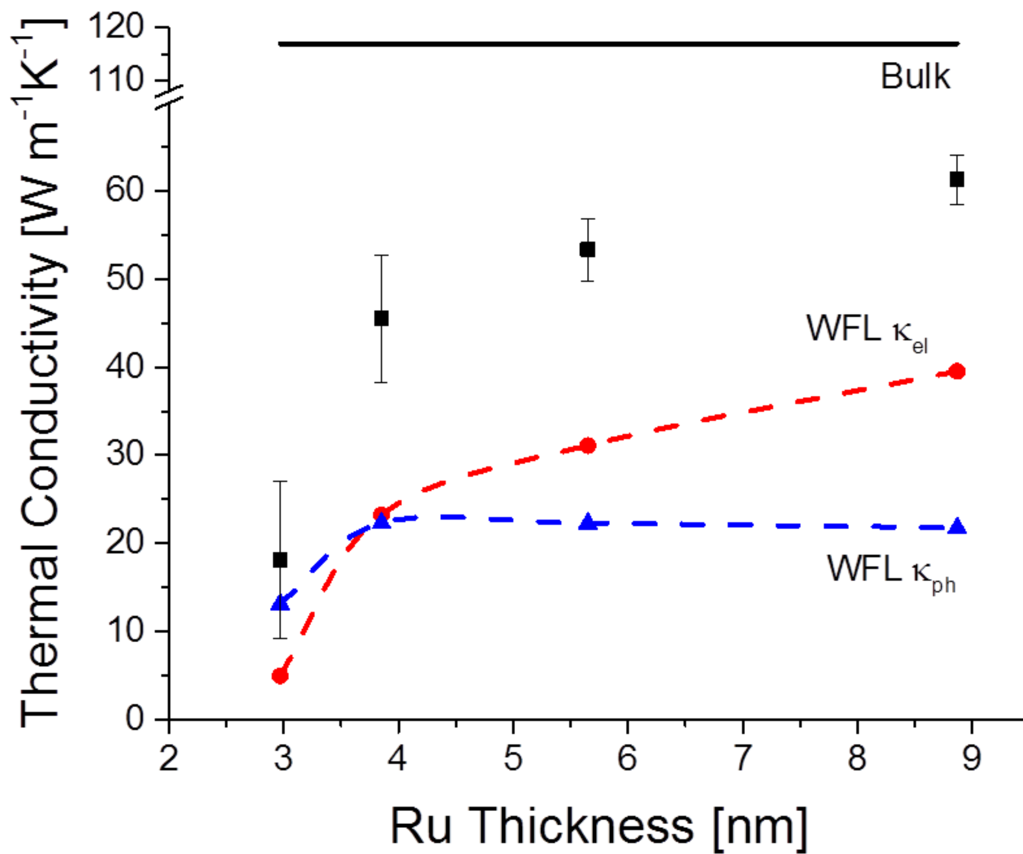

Figure 6.11: Measured thermal conductivity of ALD Ru with respect to thickness plotted as black squares. The black line is the bulk value. The red circles are WFL calculated κ_{el} values. The blue triangles are WFL calculated κ_{ph} values.

To better understand the contribution of phonon and electron conduction in these structures, the Weidemann Franz Law (WFL), which defines the electron thermal conductivity as $\kappa_e = L_o T/\rho$ where T is the absolute temperature and ρ is the measured electrical resistivity was invoked. The total thermal conductivity is given as,

$$\kappa_{tot} = \kappa_{el} + \kappa_{ph} \,, \tag{6.19}$$

where κ_{el} and κ_{ph} are the electron and phonon thermal conductivities respectively. Using the WFL and equation 6.19, κ_{el} and κ_{ph} were calculated and plotted alongside W and Ru thermal conductivities in Figure 6.10 and Figure 6.11. The large electrical resistivity of ALD W produces a very small WFL calculated κ_{el}, where κ_{ph} is ~ 85 – 95% of the total conduction. The modified MS model from section 6.2 for phonon conduction was fit to the WFL calculated phonon conduction for W (dashed line in Figure 6.10b). Input values consisted of a fixed value of τ_{u0} = 10^{-5} from prior literature on Bismuth and Antimony films[31], W bulk conductivity of 173 W m^{-1} K^{-1}, W Debye temperature of 400 K, W Debye frequency of 80,800 GHz, W phonon velocity of 5180 m s^{-1}, grain size of 2 nm, and a completely diffuse film boundary scattering term $p_{ph} = 0$. Not surprisingly, a thickness dependent S_{ph} term must be utilized to accurately fit the data. Analogous to the modelling of electrical resistivity in the W requiring a thickness dependent R term, there is likely a disordered base nucleation layer within the W, which has a larger relative effect on thinner films producing a "size effect" of its own, Here, it is evident that this size effect influences both phonon in addition to electron conduction as shown in section 6.4. The Ru data was not modeled by the MS model from section 6.2 for phonon conduction. However, based on the electrical resistivity data, it is expected that a thickness dependent S_{ph} term would be required to properly fit κ_{ph} for the thinnest structure analogous to the MS electron transport modeling

results for Ru. The smaller resistivity of Ru results in a larger κ_{el}, exceeding κ_{ph} for all but the thinnest sample. However, it is interesting that for both Ru and W, the calculated κ_{ph} values exceed the predicted maximum phonon conduction by Heino et al. for many bulk metals.[125] To investigate this disparity a discussion of Lorenz number follows.

The calculated Lorenz numbers L based on the measured thermal and electrical conductivities of the W and Ru films are plotted in Figure 6.12. These values are significantly larger than the Sommerfeld value, $L_o = 2.45 \times 10^{-8}$ obtained by the free electron theory of metals, especially for W. As discussed in section 6.4, a certain portion of electron charge carriers are reflected at grain boundaries and in effect, do not contribute to the overall electrical charge transport. However, work from Zhang et al., Wang et al. and Ordonex-Miranda et al. have shown that elastically reflected electrons at grain boundaries may interact inelastically with phonons.[126–128] This interaction will allow phonon transfer of heat through the grain boundary, in effect contributing to electron thermal conductivity. Thermally, these grain boundaries are more transparent to electrons that undergo this electron-phonon-grain interaction. For cases where this effect is dominant, the WFL is effectively invalid, as κ_{el} is now proportional to both electron and phonon transport. This phenomenon is the expected culprit for the exceedingly large Lorenz numbers for ALD W, which are approximately an order of magnitude larger than the Sommerfeld value (Figure 6.12). Continuing this interpretation for the case of Ru, the WFL is likely only invalidated for the thinnest Ru thickness, where $\kappa_{ph} > \kappa_{el}$, for the thicker Ru films, $\kappa_{el} > \kappa_{ph}$. This electron-phonon interaction is better desribed as the electron-phonon coupling factor, G_f, defined as the ratio of the lattice deformation energy of localized electrons over the kinetic energy of a localized electron. Hostetler et al. have clearly shown the grain size dependence of G_f for Au and Cr thin films.[129] For grain sizes below 20 nm, G_f is shown to increase exponentially

with decreasing grain size. Conceptually, the larger electron reflection coefficients associated with smaller grains will result in a higher probability of electron-phonon interaction, thus increasing G_f. For the 2 nm grain structure in ALD W, G_f may dominate and thus explain the exceedingly large propotion of phonon transport predicted by the WFL. This effect would also be consistent for Ru films with decreasing grain size equal to the film thickness. However, it is interesting that the WFL calcuated κ_{ph} for both W and Ru seem to reach a saturation level of ~ 20 W/mK for thicker films. The lower electron reflection coefficient for Ru along with larger grain sizes would suggest that the grain size effect on $G_{f,Ru}$ should be smaller than the effect for $G_{f,W}$. However, the absolute magnitude of this coupling coefficient is still dictated by the inter-grain atomic structure specific to the elemental material. Studies of bulk Ru and W by Colombier et al. show $G_{o,Ru}$,= 18.5 W/m^{3}K and $G_{o,W}$ = 4.3 W/m^{3}K using ultrafast laser irradiation.[130] This result suggests that the smaller grain size effect on $G_{f,Ru}$ is compensated for by the stronger background electron-lattice interaction, $G_{o,Ru}$. Conversely, the weaker background electron-lattice interaction for W, $G_{o,W}$, is compensated for by a strong enhancement by nano-grain effects.

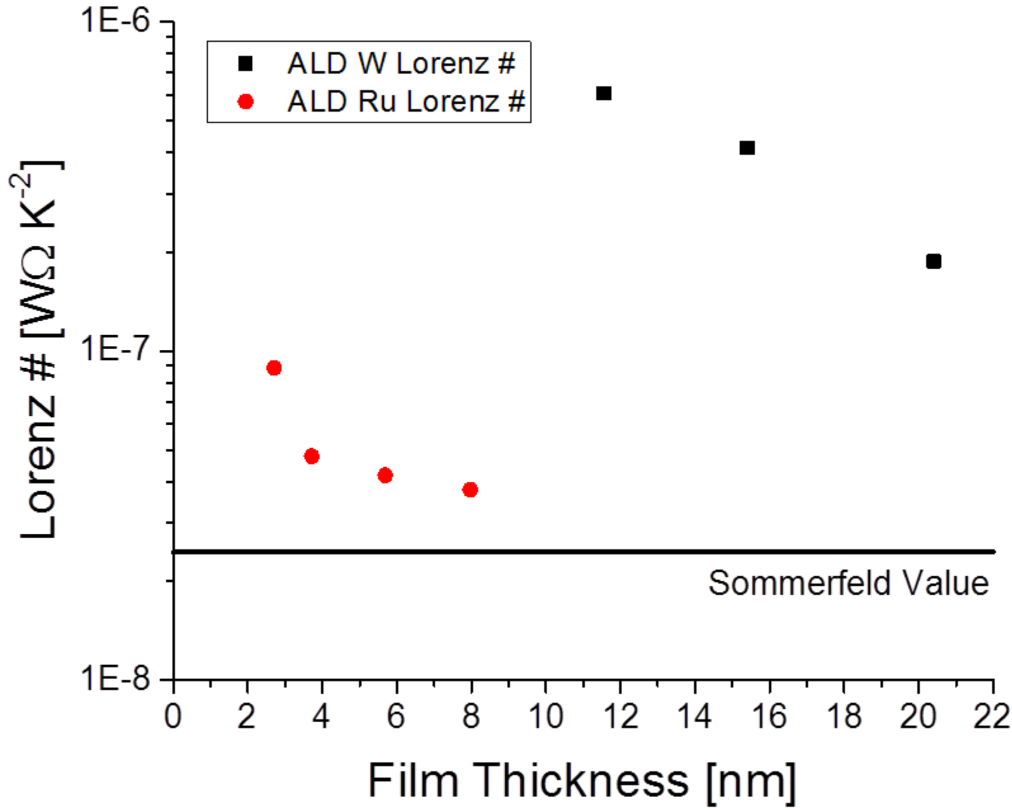

Figure 6.12: Calculated Lorenz numbers based off measured electrical resistivity and thermal conductivity for W (black squares) and Ru (red circles) with respect to film thickness.

6.8 Periodic W/Al_2O_3 Electrical Resistivity and Thermal Conductivity

The electrical resistivity of the periodic W/Al_2O_3 structures was relatively constant until the 4-layer sample. For parallel conductors, the total resistivity of a periodic layer stack is given as,

$$\rho = \left(\sum_{i=1}^{n} \frac{1}{\rho_i}\right)^{-1}, \tag{6.20}$$

where ρ_i is the resistivity of a single W layer in the periodic layer stack. This basic resistor modeling using equation 6.20 for the periodic structures is not consistent with this result and

predicts a significantly larger resistivity than measured. Experimentally, it is likely the ALD Al_2O_3 allows electron tunneling to some degree given that all electrical probing of the suspended structures occurs through the "probe-Al-ALD Al_2O_3-ALD metal" configuration. The results for the periodic resistivity suggest the in-plane conduction also allows tunneling through the thin ALD Al_2O_3 layers, lowering the overall resistivity of the periodic structure. These results indicate grain boundary scattering is still the dominant scattering effect over layer boundary scattering for W films with 2 nm grains.

The total thermal conductivity was reduced by introducing periodicity into the W film with Al_2O_3 spacers while keeping the total thickness constant as depicted by Figure 5.2. The electrical resistivity of the periodic films remained relatively constant when adding periodicity in the W until the 4-layer sample, therefore the majority of the reduction in total thermal conductivity can be attributed to a reduction in phonon conduction. Interfacial thermal resistance, or boundary resistance is invoking further phonon scattering processes due to an acoustic mismatch between the W an Al_2O_3. Enhanced scattering at the film boundaries will reduce phonon conduction in both the individual W and Al_2O_3 layers and across the interfacial boundaries. This effect will increase with decreasing layer thickness. This interpretation is consistent with results from Chen et al. on the thermal conductivity of thin film superlattices with varying layer thickness.[131]

For a constant total thickness of W and Al_2O_3, the total thermal conductivity was reduced ~ 47% by introducing periodicity. By ignoring the small conduction contribution of the Al_2O_3 spacers, the W conduction may be modeled as parallel conductors where the total thermal conductivity is,

$$\kappa_{tot}=\sum_{i=1}^{N}\kappa_{W,i}t_{W,i}/t_{W,tot}=N\kappa_{W,N}t_{W,N}/t_{W,tot}, \quad (6.21)$$

where i denotes an individual W layer with thickness $t_{W,i}$ and thermal conductivity $\kappa_{W,i}$, and $t_{W,tot}$ is the total W thickness. Since the individual W layers have equal thicknesses,

$$t_{W,i}/t_{W,tot}=1/N, \quad (6.22)$$

and thus, κ_{tot} becomes the conductivity of an individual W film, $\kappa_{W,i}$ within the laminate. Utilizing the same thickness dependent S_{ph} used to fit the WFL calculated phonon conduction from Figure 6.10, the phonon thermal conductivity of the W in the periodic structure was modeled using the MS model modified for phonon conduction (solid inverted triangles Figure 6.13).[31] The model demonstrates that phonon conduction in the W is reduced substantially. However, this model is not a completely accurate description of the thermal conductivity of the laminate since the sum of the MS_{ph} model phonon conductivity and WFL electron conductivity from the W is several W/mK less than the total measured thermal conductivity of the laminate for the 3 and 4 layer samples. This error is attributed to the lack of consideration for Al_2O_3 conduction since the phonon conduction from both the W and Al_2O_3 are on the same order of magnitude for the 3 and 4 layer samples. Also, nucleation effects from the W may be incorporating additional error since the nucleation phase is a larger portion of each total deposition cycle for thinner W layers in the more periodic structures.[15]

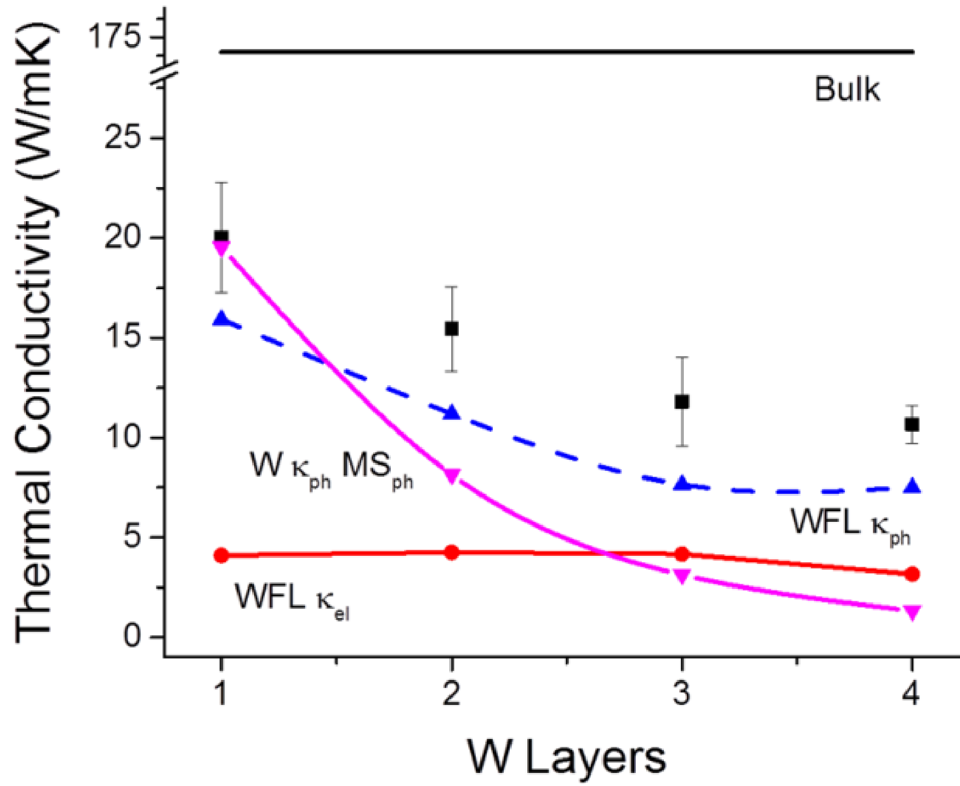

Figure 6.13: Periodicity dependence of thermal conductivity of W films at room temperature.[37] The black line is the bulk value. The red circles are WFL calculated κ_{el}. The blue triangles are WFL calculated κ_{ph}. The upside-down purple triangles are values modeled by the thickness depended MS_{ph} model.

6.9 Specific Heat Capacity of ALD Al_2O_3 and ALD W

Analogous to the parellel model extraction of ALD W and ALD Ru thermal conductivity, the extraction of specific heat capacity requires knowledge of the specific heat capacity of the associated Al_2O_3 layers.

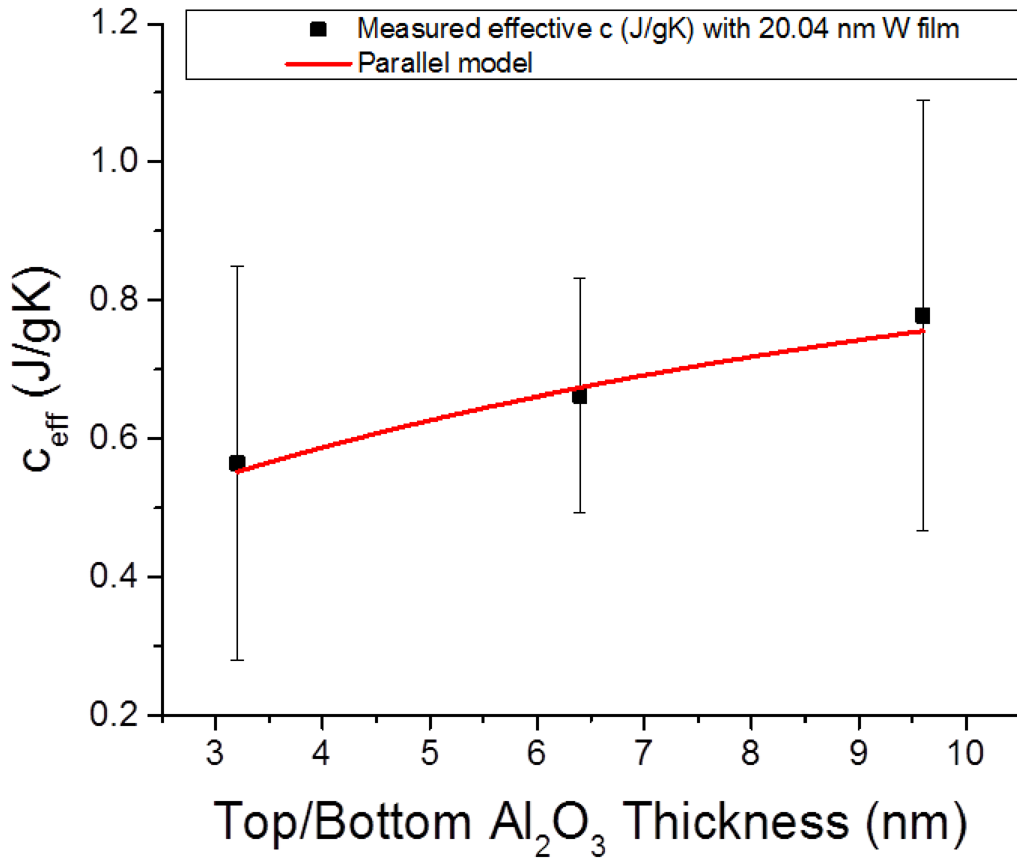

Figure 6.14: Effective specific heat capacity of Al_2O_3/20.40 nm W/Al_2O_3 at room temperature with respect to top/bottom Al_2O_3 thickness plotted as black squares. The red line corresponds to a model fit by equation 6.2.

By using the parallel model, equation 6.2, the specific heat capacity of ALD Al_2O_3 and W (free parameters) may be extracted from a sample set of varied Al_2O_3 thickness surrounding a 20.40 nm W film (Figure 6.14). The extracted values for the specific heat capacity of Al_2O_3 and

W are 1.18 ± 0.19 J/gK and 0.35 ± 0.11 J/gK, respectively. Both values are larger than the corresponding bulk values for Al_2O_3 and W of ~ 0.88 J/gK and 0.13 J/gK, respectively.

Previous work by Yu et al. and Lugo et al. measuring the specific heat of copper thin films also found their thin film copper films ranging from 20 – 200 nm to increase in specific heat with decreasing film thickness.[113,132] They attribute the enhanced specific heat capacity to the effect of grain size. Additionally, work from Rojas et al. also showed enhanced specific heat capacities of several materials with nanocrystalline structures.[133] In general, the literature shows smaller grain sizes increase the specific heat capacity of a polycyrstalline thin film. Studies from Wang et al., Ohshima et al., and Saeedian et al. of the specific heat capacity on nano particulates of varying size may illuminate this effect.[134–136] Their studies have determined that with decreasing particle size for TiO_2, CuO, Ag and Al nanoparticulates the associated specific heat capacity is enhanced. They attribute this effect to particle surface effects of phonon softening. Given the increasing ratio of atoms on the surface to the interior atoms the average phonon frequency is decreased throughout the nanoparticulate because the phonon vibration is restricted by the surface. By referencing the Debye model for phonon specific heat, the effect of phonon softening at grain boundaries may be qualitatively examined.[131] Since the frequency of phonons is proportional to $\sqrt{k/m}$, where k is the force constant which dictates the stiffness or strength of interatomic bonds and m is the effective mass of oscillation throughout the lattice structure, slowing the phonon frequency throughout the grain structure reduces k, softening the lattice structure. Thus, from a spring mass standpoint more work (energy) per mass is now required to raise the temperature of the structure since the spring mass system is softer – increasing the specific heat capacity. The energy is conserved through Grüneisen's law, resulting in an increase in the thermal expansion coefficient, as the crystal must now perform work in the form of

expansion. This effect has been witnessed in work by Narashimhan on Ag(111).[137] For the result of ALD W, the 2 nm grain structure through the film is enough to raise the specific heat capacity by ~ 2.6x. Wang et al. developed a non-dimensional model for the ratio of specific heat of a nanoparticle to that of the bulk based on grain size. The ratio, $R*$, is given as,

$$R^* = \frac{Nk_B}{d^3T^2}, \tag{6.23}$$

where N is the number of atoms in the grain, d is the diameter of the grain and T is the temperature.[134] For a 2 nm ALD W grain with a density of 16.7×10^6 g/m^3, R^* is ~ 4.4 at room temperature. This prediction is solely for the specific heat capacity of a 2 nm nanoparticle, however it is an important comparison for the thin 20 nm ALD W film with a ratio of ~ 2.6. For a thin film structure made up of 2 nm nanoparticles (grains), the effect of phonon softening will be reduced since the surface atoms will be in proximity of other surface atoms of neighboring grains. These neighboring grains will allow an increased amount of phonon transport propotional to the phonon grain boundary transmission coefficient. Relative to the case of a single nanoparticle, this transport effect will lower the overall specific heat capacity for a thin film.

The interperetation above may also be applied to the result for the amorphous ALD Al_2O_3. The atomic disorder found in amorphous structures will lower the average phonon frequency resulting in an increased specific heat capacity. Work by Queen et al. measured the excess specific heat in amorphous Si also showing an increased specific heat over crystalline Si and further increase for thinner films.[138] They attribute this effect to the natural increase of atomic disorder in thinner films (lower silicon number density). Work by Song et al. have also showed an increased specific heat with decreasing film thickness for silicon nitride films.[139] The direct study and theory of phonon transport in amorphous solids is still an undeveloped field. It is

possible that thinner films exhibit higher atomic disorder, thus increasing the specific heat, however, it is also possible that surface boundary effects cause phonon softening at boundaries in higher proportion for thinner films. Either effect will increase the specific heat of ultra-thin amorphous materials. The result for ALD Al_2O_3 is consistent with these interperetations.

The extracted specific heat capacity values for W, using c_{Al2O3} = 1.18 J/gK are plotted in Figure 6.15. Though there is large error associated with the exraction of the W specific heat, the extracted values slightly increase with decreasing thickness, ~ 33% from the 20.4 nm W to the 11.55 nm W. The effective thermal conductivity values for the Al_2O_3/W/Al_2O_3 trilayers were calculated according to the individual W and Al_2O_3 values extracted in section 6.6 and 6.7, introducing additional error in the extraction of the specific heat capacity. The effect of the highly disordered base layer in the W films may be considerable here, however the comparitive change in thermal conductivity is much larger, suggesting the relative change in specific heat capacity versus thickness can be intepereted as approximetely constant. This suggests that boundary size effects have a negligable effect in this thickness range on the specific heat capacity. The effett from nano-grain phonon softening in the ALD W remains dominant. This result is also witnessed in the periodic W/Al_2O_3 structures (Figure 5.10). With increasing W periodicity (with constant total thickness) the specific heat capacity remains approximetely contstant. This suggests that even for the 4-layer periodic sample with 4x the number of layer boundaries compared to the 1-layer sample that the nano-grain structure is the dominant mechanism for increased specific heat.

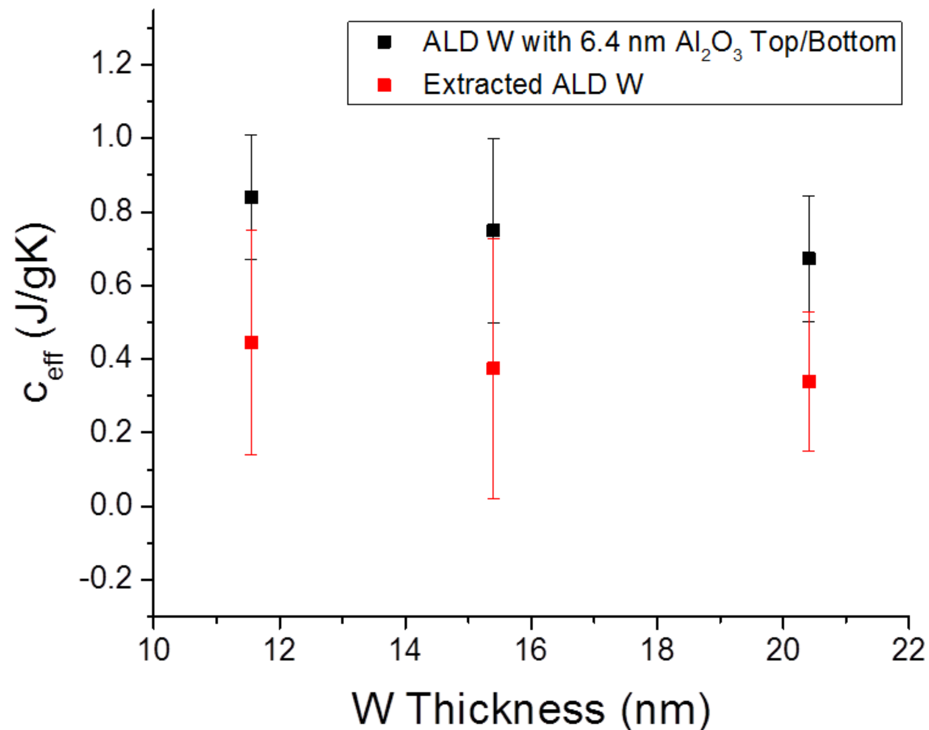

Figure 6.15: Specific heat of W/Al_2O_3 structures. The effective specific heat of 6.7 nm Al_2O_3/W/6.7 nm Al_2O_3 with respect to W thickness is plotted as black squares. The extracted specific heat of the W layer using equation 6.2 is plotted as red squares with respect to W thickness.

6.10 Specific Heat Capacity of ALD Al_2O_3 and ALD Ru

The sample set for specific heat capacity of Al_2O_3/Ru/Al_2O_3 maintained a constant Al_2O_3 thickness with varying Ru thickness (Figure 5.9). Using the parallel model from equation 6.2 and the extracted c_{Al2O3} value from Figure 5.9 results in inconsistent values obtained for the specific heat of the various Ru thickneses. A specific heat value of 1 instead of 1.18 (within error) yields extracted c_{Ru} values of 0.422 J/gK and 0.38 J/gK for the 5.7 and 8.0 nm films, respectively. Bulk Ru has a specific heat capacity of 0.238 J/gK. The Al_2O_3 for the Ru sample set was deposited at 150 °C compared to 130 °C, while the Ru was deposited on top of the first layer of Al_2O_3 at 300

°C. Higher temperature depositions can increase the index of refraction and thus increase the denisty of the Al_2O_3 film.[103] It is unknown if the density of the film could slightly lower the atomic disorder providing a more crystalline film. It is possible that this effect produced a film with lower specific heat capacity, but has not been verified. The extracted values for the thinnest Ru films of 2.7 nm and 3.7 nm had inaccurate results in the context of parallel contribution of specific heat, while also large error. A possible explanation for the poor data could arise from the thermal time constant measurement. From the *off* to *on* state of the voltage-pulse current must tunnel through the thicker Al_2O_3 layers to the Ru film – resulting in a less accurate time constant extraction. Additionally, the proportion of Ru film thickness to the total Al_2O_3 thickness was very low, increasing the error in the extraction of c_{Ru} by equation 6.2.

6.11 Summary of Electro-thermal Results

In summary, there are several distinct material property trends associated with ALD generated W, Ru and Al_2O_3 which are important to summarize before Chapter 7, where ALD material design considerations for bolometer performance will be discussed. Table 6.1 summarizes the extracted results for the discussed W, Ru and Al_2O_3 samples. For ALD W, the 2 nm grain structure dominates electron charge transport, producing a significantly larger resistivity than bulk, and a remarkable negative TCR value. Modelling results suggest the size effect witnessed for decreasing W thickness is attributed to an increasing proportion of a highly disordered nucleation layer in the thickness and not to an increased scattering effect by thinning layer boundaries. The reduction in electron charge transport in Ru is also attributed to nano-grain structure, however, an appreciable size effect is witnessed for films below 10 nm by fitting the data with a full MS model which is attributed to both thinning layer boundaries and shrinking

grain sizes. Only in the thinnest 2.7 nm Ru sample is there a significant increase in resitivity and decrease in TCR deviating from the MS *R* value of 0.49 for the thicker samples. The thermal conduction and specific heat capacity of W is also dominated by the nano-grain structure. The WFL is violated for W, producing unrealistically large Lorenz numbers attributed to a significant increase in electron-phonon coupling contributions to thermal transport. The nano-grain structure also produces a significant phonon softening surface effect, enhancing the specific heat capicity by ~ 2.6x over the bulk for ALD W. The periodic W/Al_2O_3 structures have suprisingly little effect on electron transport with increasing periodicity, yet signifcant effect on phonon trasport indicating the W-Al_2O_3 interfaces are larger acoustic barriers, than electric. However, these interfaces have a negligable effect on the effective specific heat capacity when compared to the phonon softening surface effect induced by the 2 nm grain structure. Within the thickness range studied for single layer W films, the W loses electrical conductivity faster than thermal conductivity with decreasing film thickness, while the specific heat capacity remains constant. Within the range of periodicity studied, the W loses thermal conductivity faster than electrical conductivity with increasing periodicity, while the specific heat remains constant. The Ru thermal conductivity is significantly larger than the W due to a larger contribution of electron thermal conductivity and a larger background electron-phonon coupling factor. The specific heat capacity of the Ru is larger than bulk by ~ 1.5x for the thicker samples. The larger grain structure results in a smaller phonon-softening effect compared to W, however with decreasing thickness (and grain size) this effect increases, producing a thickness dependent specific heat capacity not witnessed in the W. Several of these trends will be exploited in Chapter 7 when considering the performance of a DRS-style microbolometer structure containing absorber and support leg elements.

Table 6.1: Summary of studied material properties for ALD W, Ru and Al_2O_3.

Material	Thickness (nm)	Resistivity (μΩ*cm)	TCR (%/K)	Thermal Conductivity (W/mK)	Specific Heat Capacity (J/gK)	Volumetric Heat Capacity $(J/m^3K)\times10^6$
W	11.55	1209	-0.009	15.1	0.45	7.52
	15.4	564	-0.012	22.1	0.37	6.18
	20.40	225	-0.015	24.9	0.34	5.678
Periodic W*	1-layer	222	-0.009	20.0	0.65	7.38
	2-layer	215	-0.010	15.4	0.65	7.38
	3-layer	218	-0.012	11.8	0.60	6.81
	4-layer	289	-0.014	10.7	0.58	6.583
Ru	2.71	147	0.027	18.1	n/a	n/a
	3.71	31.5	0.091	45.5	n/a	n/a
	5.69	23.5	0.129	53.4	0.42	3.99
	7.97	18.5	0.151	61.3	0.38	3.61
Al_2O_3	n/a	n/a	n/a	1 W/mK	1 – 1.18 J/gK	3 – 3.54

*Periodic W samples include Al_2O_3 spacing layers.

Chapter 7

Application of Work to DRS Microbolometer

This chapter will summarize the work surrounding the use of ALD materials in application to the DRS microbolometer presented in section 2.2.5. Due to the sensitive nature of international traffic in arms regulation (ITAR) controlled devices manufactured by DRS Technologies Inc., actual device photos, discussion of fabrication details and discussion of absolute material thicknesses and device performance metrics will be limited to protect their product. Therefore only relative comparisons between ALD enabled and traditional materials will be quoted.

7.1 General Approach

Utilizing atomic layer deposition (ALD) generated materials will enable high-performance microbolometers by a significant (order of magnitude) reduction in dielectric thickness from traditional bolometer materials. As explained in section 2.2.4, modern microbolometers directly benefit from a reduction in heat capacity, which can be accomplished by using substantially thinner materials. Reducing heat capacity improves their fundamental

performance metric, NETD*τ_{th}, shifting the frontier of performance as shown in Figure 2.12. By utilizing ALD, film growth at sub nm scales with atomic precision and extremely high conformality is possible. By replacing traditional bolometer dielectric and metal materials for the of a DRS style bolometer pixel with ALD Al_2O_3 and ALD W, the total thickness may be reduced significantly. Therefore, an objective of this research was to successfully implement the new ultra-thin ALD materials with DRS's manufacturing processes to produce operable bolometer pixels at the 6'' wafer scale. The final objective was to fabricate functioning infrared (IR) cameras in the form of the Tamarisk 320 consumer model (Figure 7.1).

Figure 7.1: DRS Tamarisk consumer model LWIR camera.

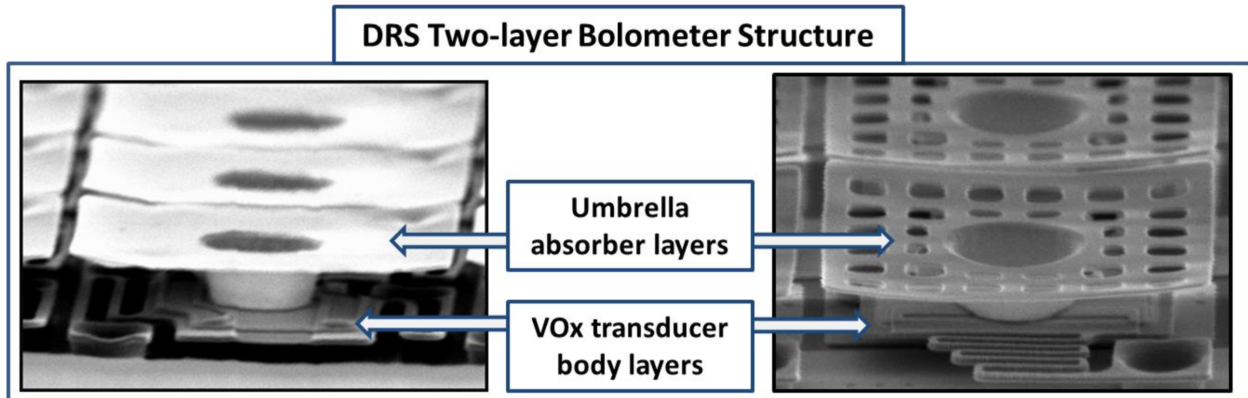

Figure 7.2: DRS-style two level microbolometer. Flat umbrella structure (left) and flat "holed" umbrella structure with reduced heat capacity (right). Images were provided by DRS.

7.2 ALD Umbrella

Several considerations for proper device performance must be made when addressing an improved umbrella structure. Optimal absorption of LWIR and proper structural separation of the umbrella layer from the body layers to prevent thermal shorting require that umbrella be flat (Figure 7.2). The umbrella structure must form a thermal contact with an underlying transducing element and also remain mechanically robust upon release. A nominal W layer with an appropriate electrical resistivity must be chosen to maximize the absorption of LWIR within the arrangement of the DRS pixel. LWIR electro-magnetic interference between the umbrella, body layers and reflective coating will determine the optimal resistivity for maximum absorption. Using the resistivity versus thickness results presented in section 6.4 a nominal layer thickness was chosen according to LWIR absorption modeling by DRS. This W layer was implemented with an Al_2O_3 sandwich to protect it during fabrication.

7.2.1 Fabrication

The ALD enabled DRS microbolometer with an ALD umbrella was fabricated according to methods described by US Patent Application 14/604,906 and work by Eigenfeld et al. presented in section 3.1.[34,35] By using the ALD on polyimide process, the multilevel DRS bolometer structure comprised of a DRS body level support leg structure and transducer, and ALD umbrella absorber structure was fabricated. To achieve this, a custom 8'' ALD reactor was built by the Steven George group at the University of Colorado Boulder to allow both W and Al_2O_3 deposition on DRS wafers. Detailed pilot studies of etch rates, material compatibility and thickness variation were conducted to integrate the new ALD fabrication step into the DRS process flow.

Figure 7.3 demonstrates the extraordinary conformality achieved by ALD during deposition on a DRS umbrella absorber via. The surface limited reactions from ALD even allow coatings to be achieved on inverted portions of over-etched via corners (right of Figure 7.3).

7.2.2 Stress Tuned Flat Umbrella

As shown in section 3.2.2, atomically controlled thickness variation in the associated ALD layers can provide optimal curl of a suspended structure. This technique was applied to Al_2O_3 sandwich layers surrounding the nominal W absorbing layer in the ALD enabled DRS umbrella structure. Figure 7.4 demonstrates the results of an umbrella structure with upward (Figure 7.4c) and downward curl (Figure 7.4d) as well as a flat suspended structure (Figure 7.4e). The flat suspended structure had a vertical deflection deviation from anchor to perimeter of +/- 250 nm, measured using a Zygo white light interferometer. The difference between a completely unusable structure and a flat suspended structure is on the order of single nm's

suggesting the use of ALD's atomic precision was crucial for a successful ultra-thin device. An unequal top and bottom thickness is required to correctly balance the stress in the umbrella structure. This may be attributed to varied surface stresses by the nucleation of films on varied substrates, i.e. Al_2O_3 on polyimide, W on Al_2O_3 and Al_2O_3 on W.

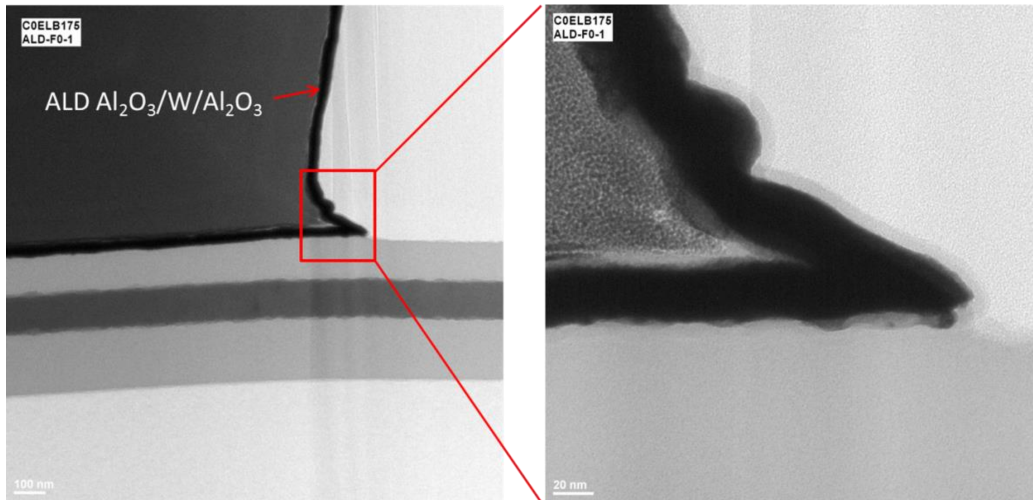

Figure 7.3: TEM images of nominal ALD coating on polyimide for an umbrella absorption structure.

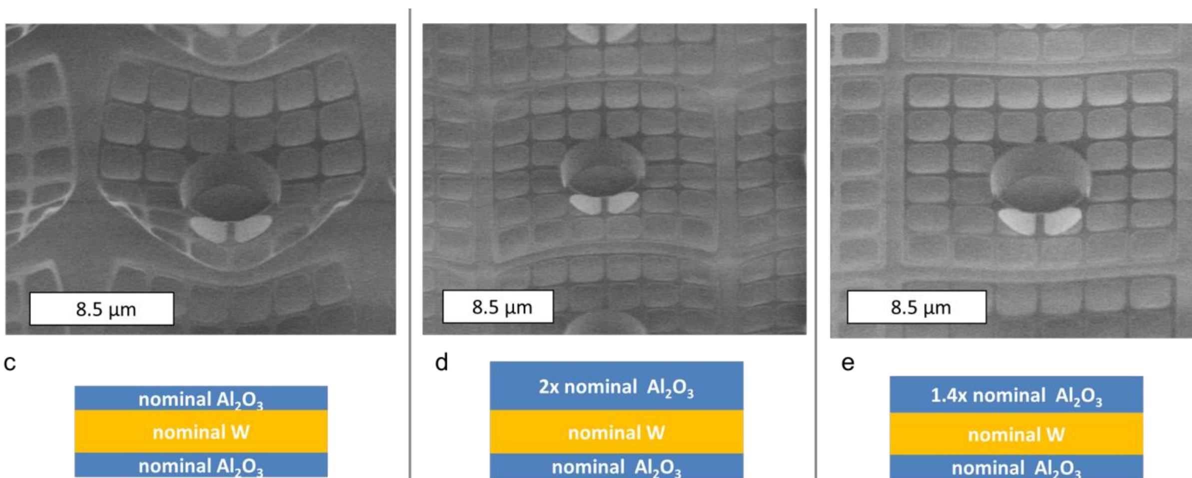

Figure 7.4 : SEM images of suspended membranes for microbolometer applications, with cross section of Al_2O_3 (blue) and W (yellow) (not to scale).[37] Only the top Al_2O_3 layer was varied in thickness. Identical W and lower Al_2O_3 layers are used in all three images. Each square structure is 16 µm × 16 µm. c) Nominal top and bottom Al_2O_3 thicknesses resulted in upward curl, while d) a top Al_2O_3 layer two times thicker resulted in downward curl. e) A flat structure was achieved with a 1.4 times nominal top Al_2O_3 layer and nominal bottom Al_2O_3 layer. Images in (c-e) were taken at 45° stage tilt angle.

7.2.3 ALD Umbrella Results and Modeling

By integrating the flat ultra-thin absorption structure with real DRS bolometer devices a 1.4X improvement in bolometer performance relative to the DRS baseline production model was achieved through a substantial reduction in overall heat capacity of the pixel. A detailed description of the bolometer performance measurement will remain proprietary to DRS. Originally, calculations of the expected performance enhancement using bulk specific heat capacity properties for W and Al_2O_3 resulted in a prediction of a 1.5X improvement for the ALD umbrella bolometer relative to the baseline production model. This prediction was inconsistent with the measured performance enhancement because of the incorrect material property inputs. If the extracted material property values of specific heat capacity for Al_2O_3 and the nominal W layer from section 6.9 are used in the calculations, a 1.4X improvement is predicted. Identified material properties and trends in nanoscale structures such as specific heat and thermal conductivity presented in this thesis will undoubtedly aid in the future modeling of the DRS microbolometer structure and nanodevices alike.

7.2.4 Electro-thermal Considerations of Umbrella

As explained in section 2.2.4, the removal of heat capacity shifts the frontier of bolometer performance, by shifting the curve of NETD vs. τ. In the case of the umbrella absorber structure there are several electro-thermal considerations to achieve optimal performance. The first is to achieve optimal electrical resistivity for LWIR absorption at thin film dimensions. Second, the film should achieve a small volumetric specific heat and thirdly, the film should have a large thermal conductivity. The absorbed radiation should be conducted to the transducing element as quickly as possible to minimize thermal leakage via radiation and conduction to air. The longer

the heat is trapped in the absorber, the larger percentage of thermal leakage will occur. Also, the faster the heat is transferred to the transducer, the larger and longer the transient temperature change during electrical readout since the heat flow out of the transducer is constricted by the support leg structure. By maximizing thermal conductivity of the umbrella, a larger signal from the transducers may be achieved.

In light of these requirements for an optimal absorber several nanoscale material property trends may be exploited. In Chapter 6 it was shown thermal conductivity decreases substantially with decreasing film thickness. However, it was witnessed in both W and Ru, that phonon conduction is a significant contribution to the total thermal conductivity due to enhanced electron-phonon coupling by electron reflections at grain boundaries resulting in a larger than expected thermal conductivity for a nanoscale film. This nanoscale effect will alter the thermal conductivity versus electrical resistivity scaling depending on grain size and various materials may be compared. In the case of the microbolometer absorption structure a term such as,

$$Z_{B-abs} = {}^{\kappa}\!/_{(\rho \cdot c_V \cdot t)}, \tag{7.1}$$

should be maximized. Here, *abs* is short for absorber, c_v is the volumetric specific heat and t the film thickness.

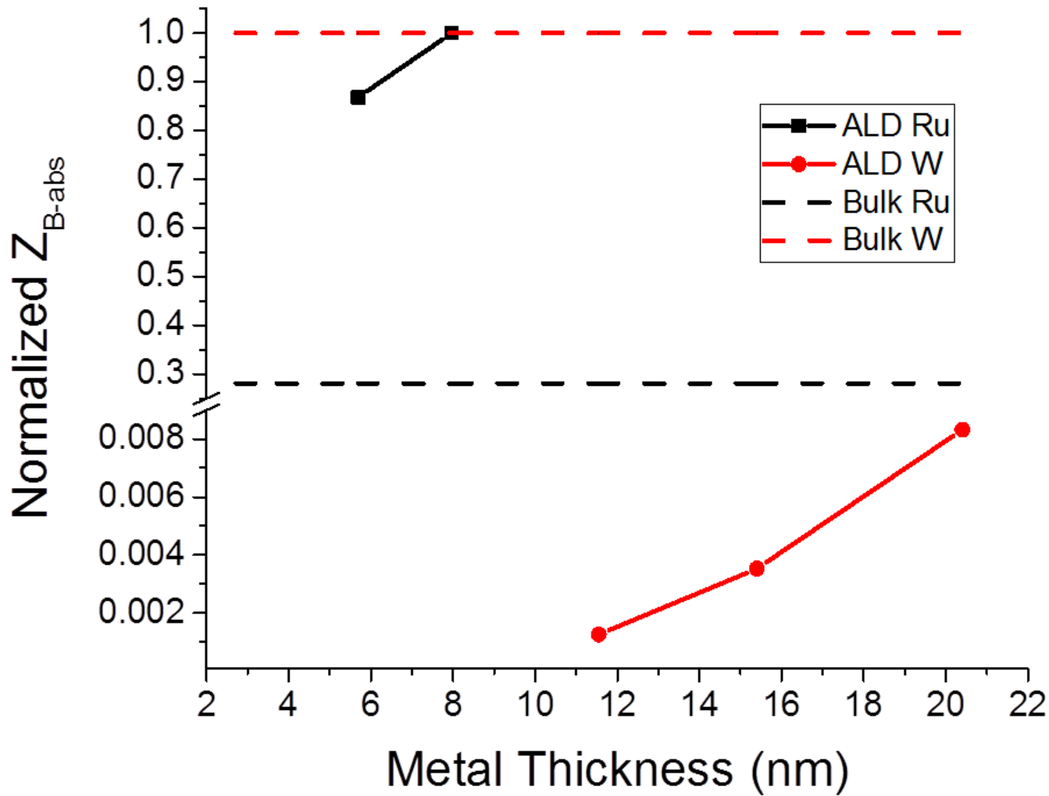

Figure 7.5: Comparison of proposed figure of merit, $Z_{B\text{-abs}}$, for single layer ALD Ru (black squares) and single layer ALD W (red circles) normalized to the 8.0 nm Ru film. Bulk Ru and bulk W normalized to bulk W are plotted as black dashes and red dashes, respectively.

A case study comparison of Ru versus W $Z_{B\text{-abs}}$ performance is shown in Figure 7.5. The Ru outperforms W in this metric significantly due to the larger thermal conductivity and order of magnitude smaller electrical resistivity at thinner thicknesses. $Z_{B\text{-abs}}$ obtains a maximum for the 7.9 nm Ru thickness. A comparison of $Z_{B\text{-abs}}$ for bulk W and Ru indicate bulk W is a higher performing absorber material than Ru. This result demonstrates the importance of evaluating nano-materials for device performance.

7.3 All-ALD Bolometer Approach

By addressing the bolometer support leg structure with ALD materials, further performance enhancement may be achieved by continued reduction in bolometer material layer thicknesses. Fundamentally, continued removal of heat capacity in the dielectric and metal layers in the support structure will improve the NETD*τ figure of merit. However, the support leg structure has several required functions including, mechanical support for the entire pixel structure, electrical connection to transducing material and thermal pathway to the underlying substrate. Because of these functional requirements, the design and optimization of this microblometer "part" is inherently more complicated than the umbrella structure. This section will address several ideal designs to meet these functional requirements with ALD laminates according to results presented in previous chapters of this thesis.

7.3.1 Structural Considerations of Support Leg

When considering the drastic material thickness reduction by replacing thick ~100 – 200 nm SiO_2 dielectric protection layers with ~ 5 – 10 nm Al_2O_3 layers, it is obvious that the support leg stiffness will be substantially reduced considering the flexural rigidity is proportional to t^3 (equation 3.1). To check if such a substantial material thickness reduction is mechanically feasible, basic flexure calculations assuming the flexures are springs were conducted. Considering the lateral geometric design and thicknesses of the transducing and umbrella components the total mass *m* was calculated. Using the geometric design of the serpentine-like support legs, a spring-mass calculation may follow. The stiffness of the serpentine leg structure is given as,

$$k_{Leg} = \frac{k_o}{4N}, \tag{7.2}$$

where N is the number of turns and k_o is the stiffness of half the length of the first segment of a turn in the serpentine structure and given as,

$$k_o = \frac{3EI}{l_o^3}, \tag{7.3}$$

where l_o is half the length of one segment of a two segment turn in the serpentine structure and EI the flexural rigidity defined by equation 3.1. For two legs in parallel,

$$k_{tot} = 2 * k_{leg}. \tag{7.4}$$

The effective modulus of ALD Al_2O_3 and a DRS leg metal was calculated based on the value measured by Tripp et al. for the Young's modulus of ALD Al_2O_3 and the bulk value for the DRS leg metal.[20] Using the lateral design of the umbrella and transducer structure, ALD Al_2O_3 and DRS transducers thicknesses and material densities, the mass, m, of the umbrella and the DRS transducers structure was calculated as ~ 0.11 ng. The deflection of the spring mass system is given as,

$$\Delta y = ma/k_{tot}, \tag{7.5}$$

where a is the gravitational acceleration constant, 9.8 m/s^2. These calculations result in a deflection of ~ 0.5 μm. Without disclosing the exact height of the DRS body level structure, but taking into consideration that the optimal absorption of the optical cavity is proportional to λ/4, where λ is the wavelength of light being absorbed, results in an optimal cavity height (height of umbrella) of ~ 2.5 μm for the LWIR.[62] Assuming the body level is roughly half this height, a 0.5 μm downward deflection is a significant proportion of the total substrate separation height and likely to cause device snap down. Device snap down is roughly universal for parallel plate actuators, cantilevers and microbridges and is governed by the $1/3z_o$ rule, where z_o is the initial

gap height. If the device does not collapse mechanically, it is likely to snap down during the pulsed-bias electrical readout measurement. Also, considering Ahmed et al. have shown that the Young's modulus of nanocrystalline metals is smaller than their corresponding bulk values, the 0.5 μm deflection prediction may be increased if the bulk value for DRS leg metal is not assumed.[140]

These results strongly suggest the use of the trench-like cross-section presented in section 3.2.1 for successful mechanical support and device function. It was previously shown theoretically by Eigenfeld et al. that the trench-like cross-section will increase the flexural rigidity by ~10^4.[34] Repeating the calculations presented above with EI_{trench} defined by equation 3.4 with a trench width and depth equal to the flat leg thickness results in a ~ 2 nm deflection, a negligible effect for a μm sized spacing. While the trench does add a measurable amount of heat capacity from the incorporation of side-walls, these calculations have shown that it is certainly a requirement for the successful function of a device with ultra-thin ALD dielectric layers.

7.3.2 Electro-thermal Considerations of Support Leg

As explained in section 2.2.4, the removal of heat capacity shifts the frontier of bolometer performance by shifting the curve of NETD vs. τ. Removal of heat capacity mainly reduces the thermal time constant, however when considering a standard 30 Hz imaging device, a small time constant is not required as previously explained in section 2.2.4. In the case of the support leg structure as opposed to the umbrella, this upperbound for τ creates design space for the support leg thermal conductance, G_{th} which acts as the thermal barrier to the substrate and is independent of the negligible series thermal resistance from the umbrella and transducer. Optimization may occur by reducing G_{th} to increase τ to its upper-bound of ~ 10 – 15 ms while simultaneously

reducing the NETD given its linear dependence on G_{th}. This optimization is most easily achieved by increasing the length, *l,* of the support leg given $C_{th} \alpha l$ and $G_{th} \alpha l^{-1}$ (staying on the curve of Figure 2.12 in section 2.2.4). However, this method would not be categorized as a fundamental improvement, or "frontier shift" in bolometer performance, only a standard optimization process.

Besides continued thickness reductions, there remain several other fundamental improvements apart from reducing the dielectric or metal thickness in the support leg structure. These include, reducing the thermal conductivity or volumetric specific heat capacity. In Chapter 6 it was shown that thermal conductivity decreases substantially with decreasing film thickness. Ideally, this reduction may be achieved while maintaining the electrical resistivity and effective specific heat capacity of the cross-section. However, it was shown that electrical resistivity and specific heat capacity increases with decreasing film thickness in Ru due to its thickness-dependent grain structure, while the W resistivity increased and specific heat capacity remained approximately constant due to its thickness-independent grain structure. However, in the periodic W/Al_2O_3 structure, the resistivity and specific heat remained constant while thermal conductivity was reduced by introducing periodicity.

In light of these specific trends in the studied nanostructured films, a new metric to describe the relative performance of bolometer support leg materials is proposed which involves the electrical resistivity, thermal conductivity, specific heat capacity and thickness similar to Z_{B-abs} described in section 7.2.4. Considering the majority of resistance change is expected to occur in the transducing element, minimal electrical resistance in the support leg structure is desired for optimal device performance. A possible figure of merit to describe the optimization of the support leg structures may closely resemble that of thermoelectric materials with the addition of

specific heat capacity and thickness. Thermoelectric materials require low electrical resistivity and low thermal conductivity and are characterized by the relation,

$$Z_T = {S^2 T}/{\rho \kappa}, \tag{7.6}$$

where S is the Seebeck coefficient, and T is the absolute temperature. In the case of microbolometer support leg optimization the Seebeck coefficient and absolute temperature are not applicable. Thus, a term such as,

$$Z_{B-leg} = {1}/{(\rho \cdot \kappa \cdot c_V \cdot t)}, \tag{7.7}$$

is more appropriate, where c_v is the volumetric specific heat and t the film thickness. Achieving minimal electrical resistivity, thermal conductivity and specific heat capacity at thin film dimensions will maximize $Z_{B\text{-}leg}$, producing a high performance support leg material. By framing the performance of the support leg in this way, lateral geometric dependence of thermal *conductance*, *heat capacity* and electrical *resistance* is removed. The performance is described by the thickness at which the metal may achieve optimal intrinsic material properties.

As a case study, the W and periodic W/Al_2O_3 structures were compared. For each structure, $Z_{B\text{-leg}}$ is normalized to the single layer W sample and plotted in Figure 7.6. As the single W layer thickness decreases, $Z_{B\text{-leg}}$ decreases due to a substantial increase in electrical resistivity. However, for the periodic structure, $Z_{B\text{-leg}}$ obtains a maximum at 3 layers. This maximum is attributed to the periodic structure losing thermal conductivity faster than gaining electrical resistivity while specific heat capacity remains constant with increasing periodicity – a trait attributed to the electrically transparent, yet acoustically opaque W-Al_2O_3 interfaces discussed in Chapter 6.

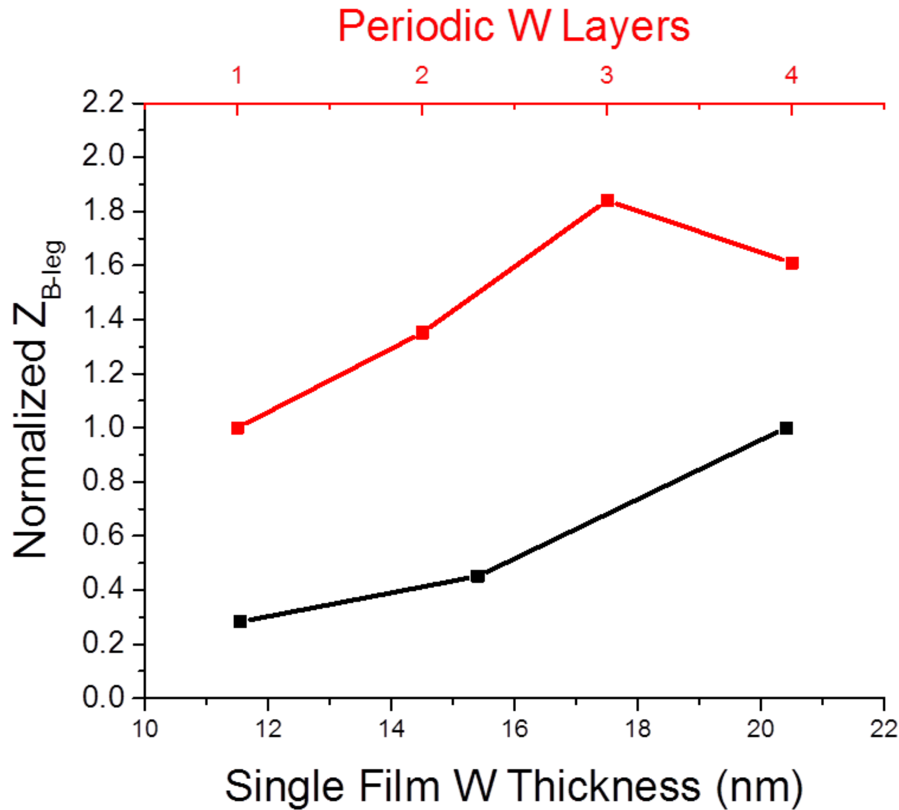

Figure 7.6: Comparison of proposed figure of merit, Z_B for single layer W (black squares) and periodic W layer structure (red squares) normalized to the 20.40 nm W or "single-layer" W structure.

Another case study comparison of Ru versus W $Z_{B\text{-}leg}$ performance is shown in Figure 7.7. The Ru outperforms W in this metric significantly. Interestingly, $Z_{B\text{-}leg}$ continues to increase with decreasing Ru thickness compared to W where $Z_{B\text{-}leg}$ decreases with decreasing W thickness, implying Ru has more favorable thickness scaling for both thermal conductivity and electrical resistivity at these thicknesses. This is further demonstrated by investigating the relation between the normalized thermal sheet resistance versus the normalized electrical sheet resistance of Ru and W as shown in Figure 7.8. The initially steep slope for thicker Ru samples (>1) provides favorable thickness scaling in the context of the $Z_{B\text{-}leg}$ performance metric. For the thicker samples studied, Ru gains thermal sheet resistance faster than electrical sheet resistance (loses thermal conductivity faster than gaining electrical resistivity with decreasing thickness).

This explains the rise in $Z_{B\text{-leg}}$ for Ru with decreasing thickness in Figure 7.7. It is expected that a local maximum would occur around 5 nm Ru in Figure 7.7 and then $Z_{B\text{-leg}}$ would begin to decrease as the thickness scaling for thermal and electrical sheet resistance becomes unfavorable and the slope in Figure 7.8 becomes < 1 and the specific heat capacity continues to increase with decreasing thickness/grain size. Unfortunately, the measured specific heat data for thinner thickness of Ru thin films was poor and thus not plotted. For W, the slope in Figure 7.8 is < 1 for all thicknesses, providing unfavorable thickness scaling.

Figure 7.7 also demonstrates a comparison of $Z_{B\text{-leg}}$ for bulk W and Ru indicate bulk W. Similar to the comparison of bulk W and Ru for $Z_{B\text{-abs}}$, bulk W is a higher performing leg material than Ru. This result again demonstrates the importance of evaluating nano-materials for device performance. Using bulk properties does not serve as a meaningful interpretation for device design.

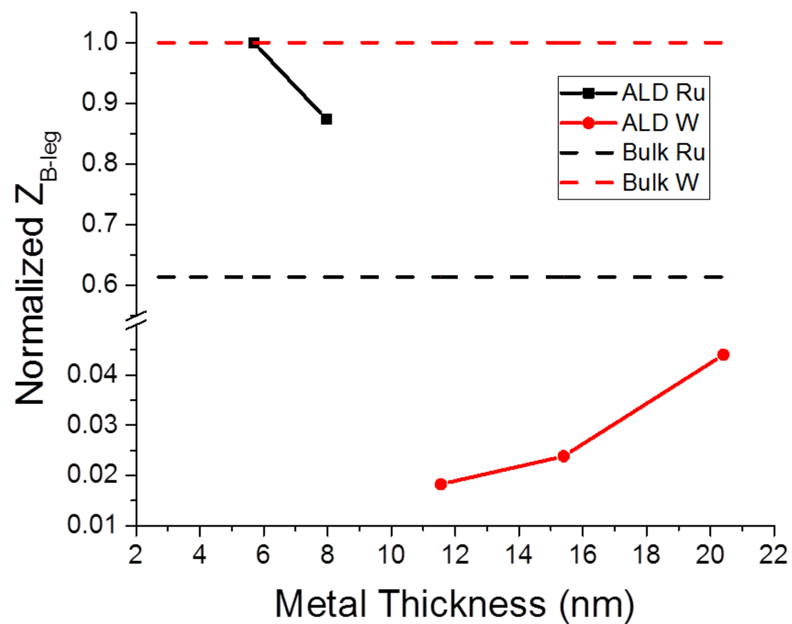

Figure 7.7: Comparison of proposed figure of merit, $Z_{B\text{-leg}}$ for single layer Ru (black squares) and single layer W (red circles) normalized to the 5.7 nm Ru film. Bulk Ru and bulk W normalized to bulk W are plotted as black dashes and red dashes, respectively.

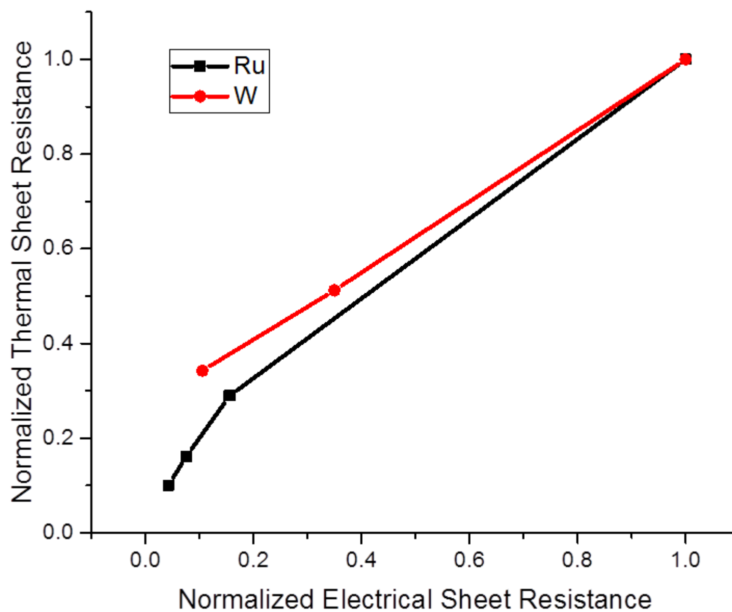

Figure 7.8: Comparison normalized thermal sheet resistance versus electrical sheet resistance for W and Ru. The data for Ru is plotted as black squares and W plotted as red circles.

Figure 7.9 demonstrates several optimization approaches. Decreasing the dielectric thickness has already been implemented. By decreasing the dielectric layer thickness both the time constant and NETD may be reduced by a simultaneous reduction in C_{th} and G_{th}, where the reduction in C_{th} is the dominant effect since the majority of thermal conduction is attributed to the metal layer and the volumetric specific heat to the dielectric layers. The second approach is shown by dashed lines. At any "frontier shift" (black squares), the length of the support legs may be varied to tailor the desired thermal time constant or NETD (black dashed line). The third is a reduction in thermal conductivity κ, assuming constant thicknesses (red circles) and constant volumetric heat capacity, analogous to the case study discussed previously for periodic W/Al_2O_3 structures. In this case, the NETD is reduced linearly by κ whereas τ is increased by κ^{-1}.

To further clarify this optimization process Figure 7.9 will help to demonstrate an optimization example using a $Al_2O_3/W/Al_2O_3$ leg structure. Several assumptions are made in this example: (1) the normalized τ=1 value corresponds to the upper limit associated with acceptable 30 Hz imaging (2) the NETD has no lower limit and should be reduced (3) the initial t_{Al2O3} is ~ 55 nm (4) there no non-linear effects associated with the *Noise* term in equation 2.8 and (5) structural support is achieved by a trench structure. The upper right corner of the black square line in Figure 7.9 corresponds to the baseline starting point. Using measured values for Al_2O_3 and W volumetric specific heat and thermal conductivity, the NETD and τ of the structure may be reduced by ~ 50% corresponding to a 75% reduction in Al_2O_3 thickness (black square and red circle intersection). This is a "frontier shift" in performance. At this juncture there are two paths for further optimization. The first is the traditional route: increase the leg length, *l*, to increase τ back to the upper-limit and produce a 30 Hz imager with a 60% reduction in NETD. This is not a "frontier shift" in performance, but only a standard optimization process. The second option at

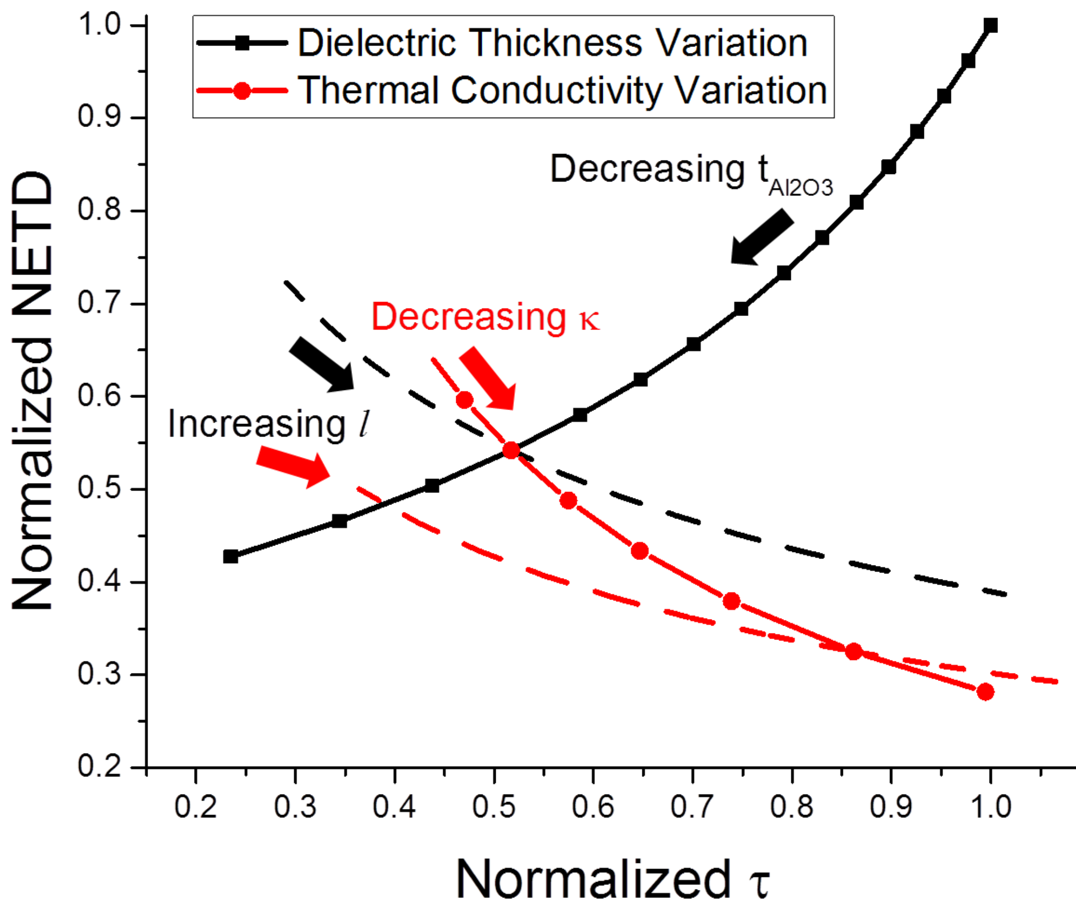

Figure 7.9: Comparison of normalized NETD with respect to normalized τ for several support leg optimization routes. The optimization begins with decreasing dielectric thickness, t_{Al2O3} and may then proceed by increasing l or decreasing κ and then increasing l.

this juncture involves increasing τ towards its upper limit by introducing the 3-layer periodicity in the W/Al_2O_3 structure, which corresponds to the optimal $Z_{B\text{-}leg}$ structure in the case study discussed above. The 3-layer periodicity decreases the effective thermal conductivity by ~ 40% (red dashed and red circle line intersection, Figure 7.9). This is considered a "frontier shift" in performance. From this juncture, increasing the length of the support structure to increase τ back to the upper-limit will produce a 30 Hz imager with a 70% reduction in NETD. Thus, by

decreasing the effective thermal conductivity by introducing periodicity into the support leg structure, a 25% improvement in the NETD*τ may be achieved during an optimization process.

It should be noted that for the discussions above, ALD W was utilized due to the convenient results discussed in Chapter 6 regarding the periodic influence on thermal conductivity. However, the absolute magnitude of its resistivity is relatively large and would not provide a low resistance structure for electrical biasing of the transducing element. The optimization process presented should be assumed universal and will be discussed further in the following sections.

7.4 The Ideal DRS-style Bolometer

In an attempt to utilize the nanoscale trends presented in this thesis, an idealized approach to a high performance DRS-style bolometer will be discussed. It should be noted that the discussion will only outline ideal materials for the absorber and support leg structure and that no non-linear or second order effects from the transducer element will be considered. While it should be obvious to the reader that removing heat capacity will improve the fundamental performance metrics, NETD*τ, more detailed approaches will be required to continue performance enhancements as the associated film thickness in the absorbing and support leg elements continue to shrink.

7.4.1 The Ideal Absorber

While a significant performance enhancement was achieved by reducing the overall thickness of the umbrella structure using ultra-thin ALD dielectric layers, there are still opportunities for further performance enhancement by optimizing the metal absorber. As shown

in Chapter 5, the ALD W resistivity was comparatively an order of magnitude larger than Ru. ALD Ru achieved lower overall resistivity at thinner thickness. Without disclosing the exact sheet-resistance required for optimal absorption, Ru can achieve optimal absorption at a ~ 70% reduced thickness than W. When considering the volumetric heat capacity (D*c) of Ru and W presented in Chapter 6, the total heat capacity of the metal layer in the umbrella structure could be reduced by ~ 88% by utilizing Ru instead of W.

Ideally, the heat capacity of the absorbing umbrella structure should be minimized. Thus, the dielectric layers should be kept to minimal thicknesses. For the case of ALD Al_2O_3 and the associated fabrication process presented in section 3.1, the minimum thickness of the dielectric layers would be limited by the required ALD cycles to form a continuous film. Assuming a dielectric/metal/dielectric configuration, the bottom protective layer is limited by the nucleation phase for the underlying substrate, often 5 – 10 AB cycles for polymer substrates and the top layer by the nucleation phase on the active metal absorber, often 1 – 5 AB cycles.

Assuming the dielectric layer thickness is minimized, the metal absorber has three key requirements for optimization which were highlighted in section 7.2.4 by the introduction of $Z_{B\text{-}abs}$ term:

1. Minimal thickness at optimal sheet resistance for LWIR absorption.
2. Minimal volumetric heat capacity.
3. Large thermal conductivity

To accomplish requirement 1, a highly conductive metal film should be used to achieve target sheet resistance values at thinner thicknesses. This can be accomplished by choosing a metal material with high electron mobility. However, it has been shown in Chapter 6 that nano-grain

effects largely dominate the electron mobility, and thus, even for a high electron mobility material such as W, the resistivity is more than two orders of magnitude larger than its bulk value because its 2 nm grain structure. Similarly, a nano-grain structure will increase the specific heat capacity due to surface phonon softening effects. Thus, to accomplish both requirements 1 and 2, the grain size should be maximized, which will also improve the thermal conductivity and contribute to accomplishing requirement 3. It is recommended that the chosen metal thin film be deposited in such a manner that a large grain structure is formed. One possibility is to deposit the metal material at greater than 40% its melting temperature following the structure model by Barna and Adamik presented in section 6.3. For ALD Ru and ALD W, this is near impossible given their melting points are > 2000 °C and CMOS circuitry can only withstand ~ 300 °C. Materials such as Aluminum, Copper or Gold have long been utilized as high conductivity thin films. Given their melting points are 658 °C, 1083 °C and 1337 °C respectively, standard evaporation and sputtering techniques can create large grain structures easily. For example, Rendón et al. were able to produce 25 nm gold films with 150 nm grain widths by heating the substrate to 300 °C during evaporation.[141] However since the thicknesses required for optimal absorption are likely < 2 nm for these low resistivity films, evaporation and other non-ALD deposition techniques will struggle to produce continuous, pinhole free films at such small thicknesses. Thus, there is a motivation for ALD enabled high conductivity films capable of producing large grain structure at < 2 nm thicknesses with minimal surface roughness. Using ALD is especially important considering that at these thicknesses, it is likely that a trench-like structure will require a highly conformal coating for structural stability. Several studies have produced ALD Cu and ALD Al. Li et al. produced ALD Cu films using a Liquid Copper (I) Amidinate Precursor and molecular hydrogen gas as the reducing agent with electrical resistivity

slightly less than the ALD Ru presented here.[142] Using electron cyclotron resonance plasma-assisted ALD, Xiong et al. grew Al films with TMA and hydrogen plasma, and then annealed them, achieving slightly larger electrical resistivity than the ALD Ru presented here.[143] Lee and Kang were also able to grow ALD Al using TMA and hydrogen plasma at 250 °C, with electrical resistivities almost identical to the ALD Ru presented here. Though the studies do not explicitly discuss grain structure, it is clear that the resistivity is limited by nano-grain effects and that ALD generated high material conductivity ultra-thin films do not provide a fundamental reduction in resistivity versus thickness scaling. It is difficult to compare volumetric heat capacities given the nano-grain structure will increase the specific heat capacity of the films over that of the bulk. However, there may be slight improvement in volumetric heat capacity for Al or Cu because their densities are considerably less than W or Ru.

7.4.2 The Ideal Support Leg

Following the optimization process presented in section 7.3.2, it should be clear to the reader that an ideal support leg meets the following requirements by $Z_{B\text{-}leg}$:

1. Minimal thickness with low electrical resistivity
2. Minimal volumetric heat capacity
3. Minimal thermal conductivity

While it was shown in section 7.3.2 that a periodic W/Al_2O_3 could provide a comparatively better $Z_{B\text{-}leg}$ term over single layer W (meeting the above requirements for comparison), the absolute resistivity of the structure was exceedingly large, failing to meet requirement 1. As described in the previous section, a thin film formation technique which can produce ultra-thin

films with large grain structures and bulk-like electrical resistivity and specific heat capacity is desired to meet requirements 1 and 2. For requirement 3, a periodic dielectric-metal structure should again be utilized. The materials should be chosen carefully as to produce an electrically transparent, yet acoustically opaque interface barrier. The ALD W/Al_2O_3 layer thicknesses are thick enough to prevent phonon tunneling, yet thin enough to provide electron tunneling. Also, the relative density mismatch between Al_2O_3 and W is very large, providing high reflectivity for phonons encountering the boundary.

For ideal materials with bulk-like electrical resistivity, it may be imagined for extremely short layer periods at fractions of the phonon wavelengths thick, the influence of phonon tunneling will offset the reduction in thermal conductivity due to interface scattering. However, Garg and Chen have shown that for real materials with interfacial disorder, the interface scattering is dominant, negating any theoretical increase in phonon tunneling across dielectric borders and increase in thermal conductivity.[144] Thus, for materials with ideal electrical resistivity, an aggressive short periodicity with dielectric-metal materials with a large density mismatch should be pursued. Periodic ALD Ru and ALD SiO_2 may provide a high performance support leg structure given the electrical resistivity of ALD Ru is quite low and the density of SiO_2 less than that of Al_2O_3 while the thermal conductivity is comparable.[124]

In summary, for both the development of an ideal absorber and support leg structure there is a need for an ALD-like thin film formation method that can produce ultra-thin films with large grain structures which produce bulk-like electrical resistivity and specific heat capacity. This is inherently difficult due to ALD temperature windows and thin film/substrate surface energy considerations. However, in future years, it may be expected that techniques to meet

these requirements are developed, as semiconductor industries likely require similar thin film characteristics.

Chapter 8

Conclusions/Future Work

8.1 Dissertation Summary

The primary focus of the research reported in this dissertation was the development of a cohesive understanding of several ALD generated materials for microbolometer development. Chapter 3 demonstrated the development of a robust nano-fabrication process applicable to a variety of suspended nano-devices. The first ever two-story suspended ALD structures were demonstrated as well as precise mechanical control of suspended structures utilizing both the conformality and atomic-level thickness control provided by ALD. Chapters 4 – 6 described the measurement methods, results and interpretation of the electro-thermal characteristics of ultra-thin W, Ru and Al_2O_3 films generated by ALD. Several interesting material property trends associated with nanoscale films were identified in material properties including electrical resistivity, temperature coefficient of resistance, thermal conductivity and specific heat capacity. These results will provide a useful nano-design utility for future nano-devices including the microbolometer. Chapter 7 demonstrated the application of Chapters 3 and 6 to a DRS-style

microbolometer. A performance increase of 1.4X over the baseline model was achieved by incorporating the fabrication process developed in Chapter 3 to the absorption umbrella of a functioning microbolometer sensor. The relative performance increase was correctly modeled using measured material property values presented in Chapter 6. Several performance enhancement approaches were discussed for the microbolometer support leg structure as well as ideal materials for absolute optimization based off identified trends in Chapter 6.

Utilizing the known properties of ALD material formation on polymers in combination with standard MEMS fabrication methods, a new method for top-down N/MEMS manufacturing with three-dimensional features, property control, and atomically controlled curl tuning has been demonstrated. The process is extendable to multiple levels, enabling the possibility of complex hierarchical systems. New opportunities for such devices are enabled by this process wherein the lateral pattern is curled to generate non-planar structures**.** Further understanding of curl properties is a serious design utility and will no doubt expedite the development of future nanosystems. The multi-level process combined with targeted stress relief could enable complex and even isotropic 3-D meta-material structures.[73] Prior to release, the sample may be coated with biological or chemical particulates to be trapped by flower petal structures upon release and even an electro-mechanical actuation scheme realized. Helical structures from this process target applications such as nano-scale flagella motors for magnetically controlled bio-implantation devices or 3-D helical chiral meta-materials.[73,145,146] This process has also aided in enhancing microbolometer performance by incorporating ultra-thin materials. Further improvements in lithography in combination with the processing defined here will enable suspended nanoscale devices with volumetric footprints on the order of tens of cubic nanometers and may be expected to impact the development of visible frequency meta-materials, optical tuning devices and

standard electronics.

By measuring the electro-thermal properties of freestanding ALD deposited W/Al_2O_3, periodic W/Al_2O_3 and Ru/Al_2O_3 nanolaminates accurate predictions of nano-devices performance may be achieved. The measured material properties have been shown to significantly deviate from bulk due to nanoscale effects such as nano-grain structure and decreased layer boundary separation. In particular, suspended periodic nanolaminates of W/Al_2O_3 have been shown to maintain electrical resistivity while decreasing phonon thermal conductivity. Utilizing this method may allow the fabrication of freestanding ultra-thin films that have approximately zero phonon conduction and have reached the WFL limit for conduction in a metal film – an interesting utility for future nano-engineering. Additionally, the specific heat capacity of ALD W has been shown to increase ~ 2.6X due to nano-grain structure. Though this effect is disadvantageous for microbolometer improvement it may offer significant utility in other thin film applications such as space coatings.

The direct application of the developed nano-fabrication process and studied material property trends produced a measured and predicted 1.4X performance improvement in a DRS microbolometer with ALD absorbing structure over a baseline pixel. The absorption was optimized by using the resistivity versus thickness curve for ALD W to identify the optimal thickness for LWIR absorption. When taking into account the increased specific heat capacity of ALD W and Al_2O_3, an accurate prediction of device performance was made. This utility extends to other material properties such as thermal conductivity and electrical resistivity of the support leg structure. In particular, the periodic structure was also predicted to produce a “frontier shift” in microbolometer performance by incorporating it into a support leg structure. Ideal thin films for continued performance enhancement were discussed in the context of identified nanoscale

trends. The ideal materials consist of ALD-like ultra-thin films with large grain structures which produce bulk-like electrical resistivity and specific heat capacity.

8.1.1 List of Major Achievements

Major achievements are listed as follows:

1. Simple and extendable ALD on polyimide fabrication process was developed that easily produces ultra-thin suspended structures. The stress relieved curl may be tuned by changing thin film layer thicknesses with atomic precision. Mechanical rigidity or mechanical control may be achieved by producing a 3-dimensional mold in the underlying polyimide substrate. The process may be extended to multiple levels by simply repeating process steps.
2. Using the developed fabrication process, ultra-thin suspended test structures were fabricated for measurement of electro-thermal properties. These properties include: electrical resistivity, temperature coefficient of resistance, thermal conductivity and specific heat capacity.
3. The measured results were correlated with nanoscale transport models and various literature studies of nanoscale films to explain trends associated with grain structure and thickness.
4. Using the developed fabrication process, an improved microbolometer structure was fabricated. Expected performance enhancement was correctly modeled utilizing measured ALD material properties.
5. An idealized approach to fundamental bolometer performance enhancement was discussed in the context of identified nanoscale trends associated with the studied

ALD materials.

8.2 Envisioned Future Work

Several items remain to be investigated for continued optimization of ALD enabled microbolometers.

8.2.1 ALD Material Parameterization

As established in section 7.4.2, there are alternative material combinations with existing ALD chemistries, which may produce lower overall heat capacity when arranged in an umbrella or support leg structure. Material combinations such as periodic Ru/Al_2O_3 or single layer/periodic Ru/SiO_2 may offer improved performance over the studied single layer W/Al_2O_3, Ru/Al_2O_3 or periodic W/Al_2O_3 films, due to reduced volumetric specific heat at thinner thicknesses. Also, dielectric materials such as TiO_2, HfO_2 and even semi-conducting ZnO should be investigated. Metals such as Pt, Al or Cu may also offer performance advantages. The nanofabrication method presented here is universal for most ALD materials given their low-temperature depositions and ability to nucleate on model ALD dielectrics such as Al_2O_3. Thus, it should be straight-forward to fabricate test structures with a variety of material combinations. For all prospective metals a comparison of $Z_{B\text{-}abs}$ and $Z_{B\text{-}leg}$ should be considered for optimal material choice.

8.2.2 New ALD-like Material Formation

As explained previously in Chapter 7.4, the investigation of high conductivity ALD materials such as Al and Cu may offer improved electrical resistivity at thinner thicknesses offering optimal electro-thermal characteristics at reduced heat capacities. However, it is

important to investigate thin film formation techniques which are capable of producing large grained structures that maintain bulk-like electro-thermal characteristics such as low resistivity and low specific heat capacity. It is envisioned that some combination of ALD, annealing and etching may allow the production of thin films with the above-mentioned desirable traits. It is foreseen that significant work in this area to develop new thin film formation technologies will push the fundamental performance of the microbolometer and nano-devices alike, while also providing an interesting utility for semi-conductor industries.

8.2.3 Improved Lithography

As lithography techniques continue to improve, the definable lateral dimensions of microbolometer parts may reach sub 100 nm's. In this regime, quantum confinement effects for electro-thermal transport must be considered. It is possible that electrical and thermal conductivity could become quantized at integer multiples of a minimum state. This may allow for interesting optimization techniques such as geometrically induced manipulation of electron and phonon coherence. It is also possible that in these nanoscale lithography regimes, there may be a simpler device design that could provide higher performance such as single level metal absorber/transducers serpentine structure from Purkl et al. demonstrated in section 2.1.5. [24]

Bibliography

1 R. P. Feynman, *J. Microelectromechanical Syst.*, 1992, **1**, 60–66.

2 M. Bohr, *Commun. ACM*, 1998, **41**, 80–87.

3 K. E. Petersen, *Proc. IEEE*, 1982, **70**, 420–456.

4 P. J. French, *Sens. Actuators Phys.*, 2002, **99**, 3–12.

5 C. Liu, *Adv. Mater.*, 2007, **19**, 3783–3790.

6 M. Melzer, D. Makarov, A. Calvimontes, D. Karnaushenko, S. Baunack, R. Kaltofen, Y. Mei and O. G. Schmidt, *Nano Lett.*, 2011, **11**, 2522–2526.

7 J. Meyer, D. Schneidenbach, T. Winkler, S. Hamwi, T. Weimann, P. Hinze, S. Ammermann, H.-H. Johannes, T. Riedl and W. Kowalsky, *Appl. Phys. Lett.*, 2009, **94**, 233305.

8 K. T. Kamtekar, A. P. Monkman and M. R. Bryce, *Adv. Mater.*, 2010, **22**, 572–582.

9 S. A. Dayeh, D. P. Butler and Z. Çelik-Butler, *Sens. Actuators Phys.*, 2005, **118**, 49–56.

10 F. H. Fabreguette, R. A. Wind and S. M. George, *Appl. Phys. Lett.*, 2006, **88**, 013116.

11 C. Oshman, B. Shi, C. Li, R. Yang, Y. C. Lee, G. P. Peterson and V. M. Bright, *J. Microelectromechanical Syst.*, 2011, **20**, 410–417.

12 A. Bagolini, L. Pakula, T. L. M. Scholtes, H. T. M. Pham, P. J. French and P. M. Sarro, *J. Micromechanics Microengineering*, 2002, **12**, 385.

13 S. M. George, *Chem. Rev.*, 2010, **110**, 111–131.

14 R. W. Wind, F. H. Fabreguette, Z. A. Sechrist and S. M. George, *J. Appl. Phys.*, 2009, **105**, 074309.

15 L. Baker, A. S. Cavanagh, D. Seghete, S. M. George, A. J. M. Mackus, W. M. M. Kessels, Z. Y. Liu and F. T. Wagner, *J. Appl. Phys.*, 2011, **109**, 084333.

16 G. K. Dalapati, Yi Tong, Wei-Yip Loh, Hoe Keat Mun and Byung Jin Cho, *IEEE Trans. Electron Devices*, 2007, **54**, 1831–1837.

17 M. Knaut, M. Junige, V. Neumann, H. Wojcik, T. Henke, C. Hossbach, A. Hiess, M. Albert and J. W. Bartha, *Microelectron. Eng.*, 2013, **107**, 80–83.

18 N. D. Hoivik, J. W. Elam, R. J. Linderman, V. M. Bright, S. M. George and Y. C. Lee, *Sens. Actuators Phys.*, 2003, **103**, 100–108.

19 C. F. Herrmann, F. W. DelRio, D. C. Miller, S. M. George, V. M. Bright, J. L. Ebel, R. E. Strawser, R. Cortez and K. D. Leedy, *Sens. Actuators Phys.*, 2007, **135**, 262–272.

20 M. K. Tripp, C. Stampfer, D. C. Miller, T. Helbling, C. F. Herrmann, C. Hierold, K. Gall, S. M. George and V. M. Bright, *Sens. Actuators Phys.*, 2006, **130-131**, 419–429.

21 Y.-J. Chang, J. M. Gray, A. Imtiaz, D. Seghete, T. Mitch Wallis, S. M. George, P. Kabos, C. T. Rogers and V. M. Bright, *Sens. Actuators Phys.*, 2009, **154**, 229–237.

22 B. D. Davidson, D. Seghete, S. M. George and V. M. Bright, *Sens. Actuators Phys.*, 2011, **166**, 269–276.

23 S. Yoneoka, J. Provine, F. B. Prinz, M. Liger, G. Yama, R. Shuster, F. Purkl, R. T. Howe and T. W. Kenny, in *IEEE*, Cancun, Mexico, 2011.

24 F. Purkl, T. S. English, G. Yama, J. Provine, A. K. Samarao, A. Feyh, B. Kim, G. O'Brien, O. Ambacher and R. T. Howe, in *The 17th International Conference on Solid-State Sensors,*

Actuators and Microsystems (TRANSDUCERS & EUROSENSORS XXVII), 2013 Transducers & Eurosensors XXVII:, 2013, pp. 1507–1510.

25 C. A. Wilson, J. A. McCormick, A. S. Cavanagh, D. N. Goldstein, A. W. Weimer and S. M. George, *Thin Solid Films*, 2008, **516**, 6175–6185.

26 C. A. Wilson, R. K. Grubbs and S. M. George, *Chem. Mater.*, 2005, **17**, 5625–5634.

27 W.-H. Kim, S.-J. Park, D. Y. Kim and H. Kim, *Jounral Korean Phys. Soc.*, 2009, **55**, 32–37.

28 J. W. Elam, Z. A. Sechrist and S. M. George, *Thin Solid Films*, 2002, **414**, 43–55.

29 J. D. Ferguson, A. R. Yoder, A. W. Weimer and S. M. George, *Appl. Surf. Sci.*, 2004, **226**, 393–404.

30 J. W. Klaus and S. M. George, *Surf. Sci.*, 2000, **447**, 81–90.

31 P. F. Carcia, R. S. McLean, M. H. Reilly, M. D. Groner and S. M. George, *Appl. Phys. Lett.*, 2006, **89**, 031915.

32 A. A. Dameron, S. D. Davidson, B. B. Burton, P. F. Carcia, R. S. McLean and S. M. George, *J. Phys. Chem. C*, 2008, **112**, 4573–4580.

33 M. D. Groner, S. M. George, R. S. McLean and P. F. Carcia, *Appl. Phys. Lett.*, 2006, **88**, 051907.

34 N. T. Eigenfeld, J. M. Gray, J. J. Brown, G. D. Skidmore, S. M. George and V. M. Bright, *Adv. Mater.*, 2014, **26**, 3962–3967.

35 N. T. Eigenfeld, J. J. Brown, J. M. Gray, G. D. Skidmore, V. M. Bright and S. M. George, US Application 14 604 906, 2014.

36 N. T. Eigenfeld, J. M. Gray, J. C. Gertsch, G. D. Skidmore, S. M. George and V. M. Bright, in *Transducers 2015 IEEE*, Anchorage, Alaska, 2015.

37 N. T. Eigenfeld, J. C. Gertsch, G. D. Skidmore, S. M. George and V. M. Bright, Nanoscale, 2015, **7**, 17923–17928.

38 G. N. Parsons, J. W. Elam, S. M. George, S. Haukka, H. Jeon, W. M. M. (Erwin) Kessels, M. Leskelä, P. Poodt, M. Ritala and S. M. Rossnagel, *J. Vac. Sci. Technol. Vac. Surf. Films*, 2013, **31**, 050818.

39 O. Thomas, A. Charai, F. M. d'Heurle, T. G. Finstad and R. V. Joshi, *Thin Solid Films*, 1989, **171**, 343–357.

40 D. Seghete, Y. J. Chang, B. Davidson, V. M. Bright and S. M. George, in *Proceedings of the Solid-State Sensors, Actuators, & Microsystems Workshop, June*, pp. 1–5.

41 J. Vila-Comamala, S. Gorelick, E. Färm, C. M. Kewish, A. Diaz, R. Barrett, V. A. Guzenko, M. Ritala and C. David, *Opt. Express*, 2011, **19**, 175–184.

42 S. Yoneoka, J. Lee, M. Liger, G. Yama, T. Kodama, M. Gunji, J. Provine, R. T. Howe, K. E. Goodson and T. W. Kenny, *Nano Lett.*, 2012, **12**, 683–686.

43 A. S. Yersak, Y. C. Lee, J. A. Spencer and M. D. Groner, *J. Vac. Sci. Technol. Vac. Surf. Films*, 2014, **32**, 01A130.

44 M. Ritala and J. Niinistö, in *ECS Transactions*, ELECTROCHEMICAL SOC INC, Vienna, Austria, 2009, vol. 25, pp. 641–652.

45 M. Horowitz, E. Alon, D. Patil, S. Naffziger, R. Kumar and K. Bernstein, in *Electron Devices Meeting, 2005. IEDM Technical Digest. IEEE International*, IEEE, 2005, p. 7–pp.

46 M. T. Bohr, R. S. Chau, T. Ghani and K. Mistry, *IEEE Spectr.*, 2007.

47 V. Mikhelashvili, G. Eisenstein, P. Thangadurai, W. D. Kaplan, R. Brener and C. Saguy, *J. Appl. Phys.*, 2008, **103**, 114106.

48 J. Niinistö, K. Kukli, M. Heikkilä, M. Ritala and M. Leskelä, *Adv. Eng. Mater.*, 2009, **11**, 223–234.

49 M. K. Tripp, C. F. Herrmann, S. M. George and V. M. Bright, in *Micro Electro Mechanical Systems, 2004. 17th IEEE International Conference on.(MEMS)*, IEEE, 2004, pp. 77–80.

50 D. Seghete, B. D. Davidson, R. A. Hall, Y. J. Chang, V. M. Bright and S. M. George, *Sens. Actuators Phys.*, 2009, **155**, 8–15.

51 I. M. Szilágyi, G. Teucher, E. Härkönen, E. Färm, T. Hatanpää, T. Nikitin, L. Khriachtchev, M. Räsänen, M. Ritala and M. Leskelä, *Nanotechnology*, 2013, **24**, 245701.

52 M. K. Tripp, F. Fabreguette, C. F. Herrmann, S. M. George and V. M. Bright, eds. E. G. Johnson, G. P. Nordin and T. J. Suleski, 2005, pp. 241–251.

53 T. M. Mayer, J. W. Elam, S. M. George, P. G. Kotula and R. S. Goeke, *Appl. Phys. Lett.*, 2003, **82**, 2883.

54 M. Leskelä and M. Ritala, *Thin Solid Films*, 2002, **409**, 138–146.

55 M. K. Tripp, C. Stampfer, C. F. Herrmann, C. Hierold, S. George and V. M. Bright, in *Solid-State Sensors, Actuators and Microsystems, 2005. Digest of Technical Papers. TRANSDUCERS'05. The 13th International Conference on*, 2005, vol. 1, pp. 851–854.

56 K. Davami, L. Zhao and I. Bargatin, in *Micro Electro Mechanical Systems (MEMS), 2014 IEEE 27th International Conference on*, IEEE, 2014, pp. 449–452.

57 L. L. Liu, O. M. Mukdadi, J. R. Hertzberg, H. B. Kim, V. M. Bright and R. Shandas, in *Biomedical Imaging: Nano to Macro, 2004. IEEE International Symposium on*, 2004, pp. 512–515.

58 C. R. Stoldt and V. M. Bright, *J. Phys. Appl. Phys.*, 2006, **39**, R163–R170.

59 V. Guériaux, A. Nedelcu, A. Coulibaly, L. Dua, N. B. de l'Isle, V. Trinité and X. Marcadet, *Infrared Phys. Technol.*, 2011, **54**, 177–181.

60 P. W. Kruse, *Uncooled thermal imaging: arrays, systems, and applications*, SPIE Press, Bellingham, Wash., USA, 2001.

61 S. Bauer, S. Bauer-Gogonea and B. Ploss, *Appl. Phys. B*, 1992, **54**, 544–551.

62 K. C. Liddiard, *Infrared Phys.*, 1993, **34**, 379–387.

63 K. C. Liddiard, *Infrared Phys.*, 1986, **26**, 43–49.

64 B. Li, *Sens. Actuators Phys.*, 2004, **112**, 351–359.

65 F. Niklaus, C. Vieider and H. Jakobsen, in *Proceedings SPIE*, eds. J.-C. Chiao, X. Chen, Z. Zhou and X. Li, 2007, p. 68360D–68360D–15.

66 US7,622,717 B2, 2009.

67 Z. Woltersdorff, *Z Phys*, 1934, **91**.

68 J. J. Monzón and L. L. Sánchez-Soto, *Appl. Opt.*, 1994, **33**, 5137–5141.

69 G. D. Skidmore, C. J. Han and C. Li, in *SPIE*, eds. N. K. Dhar and A. K. Dutta, 2014, vol. 9100, p. 910003.

70 C. Li, G. Skidmore, C. Howard, E. Clarke and C. J. Han, eds. B. F. Andresen, G. F. Fulop and P. R. Norton, 2009, p. 72980S–72980S–11.

71 W.-G. Bae, H. N. Kim, D. Kim, S.-H. Park, H. E. Jeong and K.-Y. Suh, *Adv. Mater.*, 2013.

72 N. I. Zheludev, *Opt. Photonics News*, 2011, **22**, 30–35.

73 C. M. Soukoulis and M. Wegener, *Nat. Photonics*, 2011.

74 K. Chalapat, N. Chekurov, H. Jiang, J. Li, B. Parviz and G. S. Paraoanu, *Adv. Mater.*, 2013, **25**, 91–95.

75 H. Andersson and A. van den Berg, *Curr. Opin. Biotechnol.*, 2004, **15**, 44–49.

76 W. Young and R. Budynas, *Roark's Formulas for Stress and Strain*, McGraw-Hill Professional, 7th edn., 2001.

77 J. S. Tello and A. F. Bower, *J. Mech. Phys. Solids*, 2008, **56**, 2727–2747.

78 M. S. Weinberg, *Microelectromechanical Syst. J. Of*, 1999, **8**, 529–533.

79 W.-H. Chu, M. Mehregany and R. L. Mullen, *J. Micromechanics Microengineering*, 1993, **3**, 4.

80 K. C. Yung, W. M. Wu, M. P. Pierpoint and F. V. Kusmartsev, *Contemp. Phys.*, 2013, **54**, 233–251.

81 M. F. El-Kady and R. B. Kaner, *ACS Nano*, 2014, **8**, 8725–8729.

82 S. P. Koenig, L. Wang, J. Pellegrino and J. S. Bunch, *Nat. Nanotechnol.*, 2012, **7**, 728–732.

83 A. Vijayaraghavan, *Phys. Status Solidi B*, 2013, **250**, 2505–2517.

84 M. De Volder, S. H. Tawfick, S. J. Park, D. Copic, Z. Zhao, W. Lu and A. J. Hart, *Adv. Mater.*, 2010, **22**, 4384–4389.

85 K. Dohnalová, T. Gregorkiewicz and K. Kůsová, *J. Phys. Condens. Matter*, 2014, **26**, 173201.

86 S. G. Li, Q. Gong, C. F. Cao, X. Z. Wang, J. Y. Yan, Y. Wang and H. L. Wang, *Opt. Quantum Electron.*, 2014, **46**, 623–640.

87 P. J. French, *J. Micromechanics Microengineering*, 1996, **6**, 197.

88 A. J. Learn and D. W. Foster, *J. Appl. Phys.*, 1985, **58**, 2001.

89 J. Liu, B. Yoon, E. Kuhlmann, M. Tian, J. Zhu, S. M. George, Y.-C. Lee and R. Yang, *Nano Lett.*, 2013, **13**, 5594–5599.

90 B. Feng, W. Ma, Z. Li and X. Zhang, *Rev. Sci. Instrum.*, 2009, **80**, 064901.

91 A. S. I World Congress on Engineering and International Association of Engineers, Eds., *World Congress on Engineering: WCE 2010 : 30 June - 2 July, 2010, Imperial College London, London, U.K.*, Newswood Ltd. ; International Association of Engineers, Hong Kong, 2010.

92 M. M. Sisto, S. García-Blanco, L. Le Noc, B. Tremblay, Y. Desroches, J.-S. Caron, F. Provencal and F. Picard, in *SPIE*, eds. R. C. Kullberg and R. Ramesham, 2010, vol. 7592, pp. 759204–759204–10.

93 *Fluid Flow Databook*, Genium Publishing, 1982.

94 D. C. Giancoli, *Physics*, Prentice Hall, 4th edn., 1995.

95 Y. A. Volkov, L. S. Palatnik and A. T. Pugachev, *Zh Eksp Teor Fiz*, 1976, **70**, 2244–2250.

96 J. P. Holman, *Experimental Methods for Engineers*, McGraw-Hill, 6th edn., 1994.

97 R. M. Costescu, *Science*, 2004, **303**, 989–990.

98 K. J. Park, D. B. Terry, S. M. Stewart and G. N. Parsons, *Langmuir*, 2007, **23**, 6106–6112.

99 S.-J. Park, W.-H. Kim, H.-B.-R. Lee, W. J. Maeng and H. Kim, *Microelectron. Eng.*, 2008, **85**, 39–44.

100 K. Gregorczyk, L. Henn-Lecordier, J. Gatineau, C. Dussarrat and G. Rubloff, *Chem. Mater.*, 2011, **23**, 2650–2656.

101 T. Aaltonen, P. Alen, M. Ritala and M. Leskelä, *Chem. Vap. Depos.*, 2003, **9**.

102 H. Wang, R. G. Gordon, R. Alvis and R. M. Ulfig, *Chem. Vap. Depos.*, 2009, n/a–n/a.

103 C. S. Gorham, J. T. Gaskins, G. N. Parsons, M. D. Losego and P. E. Hopkins, *Appl. Phys. Lett.*, 2014, **104**, 253107.

104 Z. Luo, H. Liu, B. T. Spann, Y. Feng, P. Ye, Y. P. Chen and X. Xu, *Nanoscale Microscale Thermophys. Eng.*, 2014, **18**, 183–193.

105 I. Stark, M. Stordeur and F. Syrowatka, *Thin Solid Films*, 1993, **226**, 185–190.

106 A. Cappella, J.-L. Battaglia, V. Schick, A. Kusiak, A. Lamperti, C. Wiemer and B. Hay, *Adv. Eng. Mater.*, 2013, **15**, 1046–1050.

107 S.-M. Lee, D. G. Cahill and T. H. Allen, *Phys. Rev. B*, 1995, **52**, 253.

108 E. H. Sondheimer, *Adv. Phys.*, 2001, **50**, 499–537.

109 K. Fuchs and N. F. Mott, *Math. Proc. Camb. Philos. Soc.*, 1938, **34**, 100.

110 A. F. Mayadas and M. Shatzkes, *Phys. Rev. B*, 1970, **1**, 1382.

111 F. Voelklein and T. Franke, in *Thermal Conductivity 23*, CRC Press, 1996, vol. 23, pp. 129–144.

112 P. G. Klemens, in *Thermal Conductivity*, Academic Press, London, 2nd edn., 1969, vol. 1.

113 J. Yu, Z. Tang, F. Zhang, H. Ding and Z. Huang, *J. Heat Transf.*, 2010, **132**, 012403.

114 S. Noge, H. Ueno, K. Hohkawa and S. Yoshikawa, in *Ultrasonics Symposium, 1995. Proceedings., 1995 IEEE*, IEEE, 1995, vol. 1, pp. 379–382.

115 P. B. Barna and M. Adamik, *Thin Solid Films*, 1998, **317**, 27–33.

116 R. B. Milligan and D. Li, in *ECS Transactions*, The Electrochemical Society, 2010, vol. 33, pp. 159–168.

117 C. R. Tellier and A. J. Tosser, *Thin Solid Films*, 1977, **44**, 141–147.

118 L. I. U. Yushuang, M. O. Chimei and C. A. I. Weili, *J. Mater. Sci. Technol.*, 2000, **16**, 521.

119 S. Bose, R. Banerjee, A. Genc, P. Raychaudhuri, H. L. Fraser and P. Ayyub, *J. Phys. Condens. Matter*, 2006, **18**, 4553–4566.

120 J. W. Elam, C. E. Nelson, R. K. Grubbs and S. M. George, *Thin Solid Films*, 2001, **386**, 41–52.

121 J. Vancea, H. Hoffmann and K. Kastner, *Thin Solid Films*, 1984, **121**, 201–216.

122 G. Reiss, J. Vancea and H. Hoffmann, *Phys. Rev. Lett.*, 1986, **56**, 2100.

123 J. Vancea, G. Reiss and H. Hoffmann, *Phys. Rev. B*, 1987, **35**, 6435.

124 K. E. Goodson, M. I. Flik, L. T. Su and D. A. Antoniadis, *J. Heat Transf.*, 1994, **116**, 317–324.

125 P. Heino and E. Ristolainen, *Microelectron. J.*, 2003, **34**, 773–777.

126 Q. G. Zhang, B. Y. Cao, X. Zhang, M. Fujii and K. Takahashi, *Phys. Rev. B*, 2006, **74**.

127 H.-D. Wang, W.-G. Ma, Z.-Y. Guo, X. Zhang and W. Wang, *Chin. Phys. B*, 2011, **20**, 040701.

128 J. Ordonez-Miranda, J. J. Alvarado-Gil and R. Yang, *J. Appl. Phys.*, 2011, **109**, 094310.

129 J. L. Hostetler, A. N. Smith, D. M. Czajkowsky and P. M. Norris, *Appl. Opt.*, 1999, **38**, 3614–3620.

130 J. P. Colombier, F. Garrelie, N. Faure, S. Reynaud, M. Bounhalli, E. Audouard, R. Stoian and F. Pigeon, *J. Appl. Phys.*, 2012, **111**, 024902.

131 G. Chen, *Nanoscale Energy Transport and Conversion*, Oxford, New York, 2005.

132 J. M. Lugo, C. Ayora, V. Rejón and A. I. Oliva, *Thin Solid Films*, 2015, **585**, 24–30.

133 D. P. Rojas, L. Fernández Barquín, J. Rodríguez Fernández, L. Rodríguez Fernández and J. Gonzalez, *Nanotechnology*, 2010, **21**, 445702.

134 B.-X. Wang, L.-P. Zhou and X.-F. Peng, *Int. J. Thermophys.*, 2006, **27**, 139–151.

135 K. Ohshima, T. Fujita and T. Kuroishi, *J. Phys. Colloq.*, 1977, **38**.

136 M. Saeedian, M. Mahjour-Shafiei, E. Shojaee and Mohammadizadeh, *J. Comput. Theor. Nanosci.*, 2012, **9**, 616.

137 S. Narasimhan, *Surf. Sci.*, 1998, **417**, 1166–1172.

138 D. Queen, X. Liu, J. Karel, T. Metcalf and F. Hellman, *Phys. Rev. Lett.*, 2013, **110**.

139 Q. Song, Z. Cui, S. Xia, Z. Chen and J. Zhang, *Sens. Actuators Phys.*, 2004, **112**, 122–126.

140 H. S. T. Ahmed, E. Brannigan and A. F. Jankowski, *J. Nanotechnol.*, 2013, **2013**, 1–10.

141 G. Rendón, P. Poot, A. I. Oliva and F. J. Espinosa-Faller, *J. Appl. Res. Technol.*, 2012, **10**, 549–556.

142 Z. Li, A. Rahtu and R. G. Gordon, *J. Electrochem. Soc.*, 2006, **153**, C787.

143 Y.-Q. Xiong, X.-C. Li, Q. Chen, W.-W. Lei, Q. Zhao, L.-J. Sang, Z.-W. Liu, Z.-D. Wang and L.-Z. Yang, *Chin. Phys. B*, 2012, **21**, 078105.

144 J. Garg and G. Chen, *Phys. Rev. B*, 2013, **87**.

145 L. Zhang, J. J. Abbott, L. Dong, B. E. Kratochvil, D. Bell and B. J. Nelson, *Appl. Phys. Lett.*, 2009, **94**, 064107.

146 V. Y. Prinz, V. A. Seleznev, A. K. Gutakovsky, A. V. Chehovskiy, V. V. Preobrazhenskii, M. A. Putyato and T. A. Gavrilova, *Phys. E Low-Dimens. Syst. Nanostructures*, 2000, **6**, 828–831.